University of California
Los Angeles

Orbital Structure of Multi-Asteroid and Multi-Planet Systems

A dissertation submitted in partial satisfaction
of the requirements for the degree
Doctor of Philosophy in Astronomy

by

Julia Anna Fang

2013

Abstract of the Dissertation

Orbital Structure of Multi-Asteroid and Multi-Planet Systems

by

Julia Anna Fang

Doctor of Philosophy in Astronomy

University of California, Los Angeles, 2013

Professor Jean-Luc Margot, Chair

The study of multi-body asteroid systems has a significant impact on key questions in planetary astronomy. From analysis of the orbits of satellites around a primary asteroid, fundamental physical characteristics can be directly measured, and the abundance and orbital properties of binaries and triples can reveal much about their formation, evolution, and dynamical environment. Our investigations of both near-Earth triple asteroids 2001 SN263 and 1994 CC and main belt triple Sylvia have elucidated their orbital and physical properties as well as dynamical evolution. These multi-body asteroid systems are also local laboratories for studying dynamics on a much different scale: multi-planet systems. The in-depth dynamical and statistical characterization of multi-planet systems have allowed for a more substantial understanding of the architecture of planetary systems, and have also led to fundamental clues about planet formation and evolutionary processes. By fitting models to data from the *Kepler* mission, we found that multi-planet systems are typically flat with low relative inclinations and many of them are dynamically packed. The scientific diversity of knowledge gleaned from studying the dynamics of systems with different scales (from asteroids to exoplanets) has the common theme of using N-body dynamics to inform us about the orbital architecture of individual systems and to illuminate the properties of an ensemble of systems as a whole.

The dissertation of Julia Anna Fang is approved.

Kevin McKeegan

Michael Fitzgerald

Michael Jura

Jean-Luc Margot, Committee Chair

University of California, Los Angeles

2013

Dedicated to my parents.

Table of Contents

1 Orbits of Near-Earth Asteroid Triples 2001 SN263 and 1994 CC: Properties, Origin, and Evolution [Fang et al. 2011, AJ, 141, 154] 1

2 Orbits, Masses, and Evolution of Main Belt Triple (87) Sylvia [Fang et al. 2012, AJ, 144, 70] 48

3 Architecture of Planetary Systems Based on *Kepler* Data: Number of Planets and Coplanarity [Fang & Margot 2012, ApJ, 761, 92] 93

4 Are Planetary Systems Filled to Capacity? A Study Based on *Kepler* Results [Fang & Margot 2013, ApJ, 767, 115] 134

List of Figures

Figure 1.01 Best-fit orbit diagrams of 2001 SN263 and 1994 CC 3

Figure 1.02 Range and doppler residuals for 2001 SN263 17

Figure 1.03 Reduced chi-square as a function of orbital parameters for 2001 SN263 19

Figure 1.04 Reduced chi-square as a function of physical parameters for 2001 SN263 21

Figure 1.05 Range and doppler residuals for 1994 CC 22

Figure 1.06 Reduced chi-square as a function of orbital parameters for 1994 CC 27

Figure 1.07 Reduced chi-square as a function of physical parameters for 1994 CC 28

Figure 1.08 Sample resonant argument for 1994 CC 32

Figure 1.09 Close encounter statistics for 2001 SN263 37

Figure 1.10 Distribution of final eccentricities and inclinations for 2001 SN263 38

Figure 1.11 Close encounter statistics for 1994 CC 39

Figure 1.12 Distribution of final eccentricities and inclinations for 1994 CC 40

Figure 2.01 Keck H-band adaptive optics image of Sylvia 53

Figure 2.02 Diagram of best-fit orbits for satellites Remus and Romulus 65

Figure 2.03 Residuals for Remus 66

Figure 2.04 Residuals for Romulus 67

Figure 2.05 Variation of semi-major axis and eccentricity over 50 years 72

Figure 2.06 Tidal love number as a function of radius 76

Figure 2.07 Simulation with resonant capture and no escape 81

Figure 2.08 Simulations with resonant capture followed by escape 83

Figure 3.01 Observed and debiased distributions of orbital periods and radii 100

Figure 3.02 Known transiting planets and different mass-radius relations 104

Figure 3.03 Chi-square probabilities for multiplicity fit 114

Figure 3.04 K-S probabilities for inclination fit 115

Figure 3.05 Combined probabilities for overall fit 116

Figure 3.06 A best-fit model for multiplicity and inclination 119

Figure 3.07 Fit for normalized transit duration ratios 120
Figure 4.01 Observed transiting exoplanets and mass-radius relationships 139
Figure 4.02 Best-fit model's underlying mutual Hill radii distribution 145
Figure 4.03 Comparison between Kepler detections and simulated detections 146
Figure 4.04 Comparison to the Solar System 149

List of Tables

Table 1.01 Orbit model constraints	6
Table 1.02 Range of initial conditions for 2001 SN263	8
Table 1.03 Range of initial conditions for 1994 CC	10
Table 1.04 Best-fit parameters and errors for 2001 SN263	16
Table 1.05 2001 SN263 precession rates	20
Table 1.06 Best-fit parameters and errors for 1994 CC	24
Table 1.07 1994 CC precession rates	25
Table 1.08 Minimum orbital intersection distance	41
Table 2.01 Summary of 2011 observations	52
Table 2.02 Astrometry from 2001 data	53
Table 2.03 Existing astrometry from 2001-2004 data	55
Table 2.04 Best-fit parameters and uncertainties for Sylvia	63
Table 3.01 Multiplicity vector	120
Table 4.01 Lower limits on dynamically packed systems	152

Acknowledgments

I am thankful for the support of my thesis advisor, Jean-Luc Margot. His patience, insight, and encouragement have been invaluable to me over the years. Without him, I am not sure if I would have continued in this PhD program to this day. The decision to work with him was without a doubt the best decision I made in graduate school. Under his tutelage, I learned how to think like a scientist and I gained valuable technical skills, all of which will forever be a part of how I frame my thoughts and how I view the world. Over the course of our collaboration, he has imparted many valuable words of wisdom and one of the most memorable was, "You've done Tycho's work. Now go be a Kepler!"

I would also like to thank other members of the Department of Physics and Astronomy and the Earth and Space Sciences Department. I am grateful to members of my thesis committee for contributing their time, effort, and mentorship: Michael Jura, Michael Fitzgerald, and Kevin McKeegan. Last but not least, graduate school would have been a completely different animal without the help and support of my fellow graduate students. For these reasons I am lucky to have known Ian Crossfield, Fred Davies, Shane Frewen, Tom Esposito, Betsy Mills, Nate Ross, Siyi Xu, Robin Mostardi, David Rodriguez, Lauren Holzbauer, Sylvana Yelda, Kathy Kornei, and Tuan Do.

Many research colleagues have provided assistance with my projects. I would like to thank John Chambers for his assistance with the N-body integrator, MERCURY. I would also like to acknowledge Mats Rynge for his assistance with the Open Science Grid. I am also indebted to the entire *Kepler* team for procuring such an excellent dataset of planetary systems. I am also grateful to Bill Bottke, Dan Fabrycky, Frederick Davies, Stan Peale, Man Hoi Lee, Seth Jacobson, Ben Collins, Simon Porter, Matija Cuk, Peter Goldreich, and Jay McMahon for useful discussions. I would also like to thank all of the anonymous reviewers who took the time to provide useful comments on my papers over the years.

My projects have utilized a number of telescope and computing facilities. Some of the data presented herein were obtained at the W. M. Keck Observatory, which is operated as a scientific partnership among the California Institute of Technology, the University of California, and the National Aeronautics and Space Administration. The Observatory was made possible by the generous financial support of the W. M. Keck Foundation. My work was based in part on observations made with ESO telescopes at the La Silla Paranal Observatory under program ID 088.C-0528. In addition, I used data from Arecibo Observatory, which is part of the National Radio Astronomy and Ionosphere Center, which is operated by SRI International under a cooperate agreement with the National Science Foundation. Some of this work was performed at the Jet Propulsion Laboratory, California Institute of Technology, under contract with the National Aeronautics and Space Administration (NASA). My research was also performed using resources provided by the Open Science Grid (OSG), which is supported by the National Science Foundation and the U.S. Department of Energy's Office of Science.

During my PhD career, I was financially supported by a number of sources, including teaching assistantships from UCLA's Department of Physics and Astronomy, NASA Planetary Astronomy Grant NNX09AQ68G, and NASA Earth and Space Sciences Graduate Fellowship.

The dissertation is organized as a collection of chapters. Each chapter is a reprint of a peer-reviewed publication of which I am the first author. The publications have been reproduced with permission by the AAS.

Vita

2009	B.A. (Physics), Northwestern University.
2011	M.S. (Astronomy), University of California, Los Angeles.

Publications

Fang, J., and Margot, J.L., "Are Planetary Systems Filled to Capacity? A Study Based on Kepler Results", 2013, *The Astrophysical Journal*, 767, 115

Fang, J., and Margot, J.L., "Architecture of Planetary Systems Based on Kepler Data: Number of Planets and Coplanarity", 2012, *The Astrophysical Journal*, 761, 92

Fang, J., Margot, J.L., Rojo, P., "Orbits, Masses, and Evolution of Main Belt Triple (87) Sylvia", 2012, *The Astronomical Journal*, 144, 70

Sromovsky, L.A., Hammel, H.B., de Pater, I., Fry, P.M., Rages, K.A., Showalter, M.R., Merline, W.J., Tamblyn, P., Neyman, C., Margot, J.L., Fang, J., Colas, F., Dauvergne, J.L., Gmez-Forrellad, J.M., Hueso, R., Snchez-Lavega, A., Stallard, T., "Episodic bright and dark spots on Uranus", 2012, *Icarus*, 220, 6

Fang, J., and Margot, J.L., "Predicting Planets in Kepler Multi-Planet Systems", 2012, *The Astrophysical Journal*, 751, 23

Fang, J., and Margot, J.L., "The Role of Kozai Cycles in Near-Earth Binary Asteroids", 2012, *The Astronomical Journal*, 143, 59

Fang, J., and Margot, J.L., "Near-Earth Binaries and Triples: Origin and Evolution of Spin-Orbital Properties", 2012, *The Astronomical Journal*, 143, 24

Fang, J., and Margot, J.L., "Binary Asteroid Encounters with Terrestrial Planets: Timescales and Effects", 2012, *The Astronomical Journal*, 143, 25

Brozovic, M., Benner, L.A.M., Taylor, P.A., Nolan, M.C., Howell, E.S., Magri, C., Scheeres, D.J., Giorgini, J.D., Pollock, J.T., Pravec, P., Galad, A., Fang, J., Margot, J.L., Busch, M.W., Shepard, M.K., Reichart, D.E., Ivarsen, K.M., Haislip, J.B., Lacluyze, A.P., Jao, J., Slade, M.A., Lawrence, K.J., Hicks, M.D., "Radar and optical observations and physical modeling of triple near-Earth Asteroid (136617) 1994 CC", 2011, *Icarus*, 216, 241

Fang, J., Margot, J.L., Brozovic, M., Nolan, M., Benner, L., Taylor, P., "Orbits of Near-Earth Asteroid Triples 2001 SN263 and 1994 CC: Properties, Origin, and Evolution", 2011, *The Astronomical Journal*, 141, 154

Introduction

This thesis is a compilation of four chapters, each composed of a published paper. The first two chapters describe my work on orbit and mass modeling of multi-asteroid systems 2001 SN263, 1994 CC, and Sylvia. The remaining two chapters describe my work fitting multiplicity, inclination, and dynamical spacing distributions to *Kepler* data. The following paragraphs provide a brief synopsis of each chapter.

Chapter 1 describes three-body model fits to Arecibo and Goldstone radar data of 2 near-Earth triples: 2001 SN263 and 1994 CC. The larger system, 2001 SN263, has an inner satellite orbiting at $\sim$3 primary radii with a period of $\sim$0.7 days and an outer satellite orbiting at $\sim$13 primary radii with a period of $\sim$6.2 days. 1994 CC is a smaller system with satellites orbiting at $\sim$5.5 and $\sim$19.5 primary radii with orbital periods of $\sim$1.2 and $\sim$8.4 days, respectively. Precession of orbital apses and nodes are detected in both systems (on the order of 1 deg/day) and agree with analytical predictions from secular evolution. In both systems, significant mutual inclinations of $\sim 14-16$ degrees between the orbital planes of the satellites suggest that past processes may have generated the observed misalignment. In particular, I show how close planetary encounters can excite such inclinations to observed values.

Chapter 2 focuses on Sylvia, a triple system located in the main belt. I present new adaptive optics observations and astrometry for this system, and I fit fully dynamical three-body models to all available astrometric data. Sylvia is composed of a dominant-mass primary body orbited by two satellites located at about 5 and nearly 10 primary radii. Their orbits are relatively circular with eccentricities less than 0.04. The system is remarkably coplanar: the spin axis of the primary body and the orbital poles of both satellites are all aligned to within about 2 degrees of each other. This near-alignment is suggestive of satellite formation in or near the equatorial plane of the primary. I also investigate Sylvia's past orbital evolution by simulating the effects of passage through the 3:1 mean-motion resonance, which can help place constraints on interior structure and past eccentricity values.

Chapter 3 describes the underlying architecture of planetary systems using the sample of planetary candidates identified by the *Kepler* mission. I derive typical planet multiplicity (i.e., number of planets per system) and the distribution of orbital inclinations. The scope of this study included solar-like stars, planets with orbital periods less than 200 days, and planet radii between 1.5 and 30 Earth radii. Based on best-fitting models, I find that 75−80% of planetary systems have 1 or 2 planets with orbital periods less than 200 days. Over 85% of planets have orbital inclinations less than 3 degrees. Such low inclinations are consistent with planets forming in a protoplanetary disk, followed by evolution without significant and lasting perturbations from other bodies capable of increasing inclinations.

Chapter 4 includes my work on fitting to the mutual Hill radii distribution among *Kepler* planetary candidates. I generate populations of planetary systems following various dynamical spacing distributions of adjacent planets, subject them to synthetic observations by the *Kepler* spacecraft, and compare the properties of observed planets in my simulations with actual *Kepler* detections. I determine the intrinsic (i.e., free of observational bias) dynamical spacing distribution of neighboring planets, and on average they are spaced 21.7 mutual Hill radii apart with a standard deviation of 9.5. I also test the *packed planetary systems* hypothesis, which states that all planetary systems are dynamically packed (i.e., filled to capacity). I find that $\geq$31%, $\geq$35%, and $\geq$45% of two-planet, three-planet, and four-planet systems are dynamically packed. Such sizeable fractions suggest that many planetary systems are filled to capacity and therefore cannot include an additional intermediate planet without leading to instability.

Chapter 1

Orbits of Near-Earth Asteroid Triples 2001 SN263 and 1994 CC: Properties, Origin, and Evolution

Reproduced by permission of the AAS (Fang, J., Margot, J.L., Brozovic, M., Nolan, M., Benner, L., Taylor, P., 2011, The Astronomical Journal, 141, 154).

1. Introduction

The existence and prevalence (∼16%) of binary asteroids in the near-Earth population (Margot et al. 2002; Pravec et al. 2006) naturally lead to the search and study of multiple-asteroid systems (Merline et al. 2002; Noll et al. 2008). Triple systems are known to exist in the outer Solar System, the main belt, and the near-Earth population. Among the trans-neptunian objects (TNOs), there are currently two well-established triples, 1999 TC36 (Margot et al. 2005; Benecchi et al. 2010) and Haumea (Brown et al. 2006), and one known quadruple, Pluto/Charon (Weaver et al. 2006). In the main belt population, four triples are known to exist: 87 Sylvia, 45 Eugenia, 216 Kleopatra, and 3749 Balam (Marchis et al. 2005; Marchis et al. 2007; Marchis et al. 2008a; Marchis et al. 2008b). There are currently only two well-established asteroid triples in the near-Earth population, 2001 SN263 (Nolan et al. 2008a) and 1994 CC (Brozovic et al. 2009), both of which are the focus of this study. There is also another possible triple, near-Earth asteroid 2002 CE26, that may have a tertiary component but the limited observational span of this object prevented an undisputable detection (Shepard et al. 2006).

(153591) 2001 SN263 has been unambiguously identified as a triple-asteroid system, and its orbit around the Sun is eccentric at 0.48 with a semi-major axis of 1.99 AU and inclined 6.7 degrees with respect to the ecliptic. It is an Amor asteroid with a pericenter distance of 1.04 AU. The system is composed of three components: a central body (equivalent radius

$\sim$ 1.3 km) and two orbiting satellites. In this paper, we use the following terminology for triple systems: the central body (most massive component) is called Alpha, the second most massive body is termed Beta, and the least massive body is named Gamma (Figure 1). In the case of 2001 SN263, Beta is the outer satellite and Gamma is the inner satellite. The other near-Earth triple is (136617) 1994 CC with a primary of equivalent radius R $\sim$ 315 m, where the opposite is true; Beta is the inner body and Gamma is the outer body. Its heliocentric orbit has a semi-major axis of 1.64 AU and is also eccentric (0.42) and inclined (4.7 degrees) with respect to the ecliptic. 1994 CC is an Apollo asteroid with a pericenter distance of 0.95 AU.

In this work, we present dynamical solutions for both triple systems, 2001 SN263 and 1994 CC, where we derived the orbits, masses, and Alpha's J_2 gravitational harmonic using N-body integrations. We utilize range and Doppler data from Arecibo and Goldstone, and these observations as well as our methods are described in Section 2. In Section 3, we present our best orbital solutions and their uncertainties. We also include discussion regarding the satellite masses and the primary's oblateness (described by J_2), and the observed precession of the apses and nodes are compared to analytical predictions. Section 4 describes the origin and evolution of the orbital configurations, including Kozai and evection resonant interactions, as well as the effects of planetary encounters.

Previous studies of multiple TNO systems include the analytic theory of Lee & Peale (2006) for Pluto, where they treated Nix and Hydra as test particles. Tholen et al. (2008) used four-body orbit solutions to constrain the masses of Nix and Hydra; they did not find evidence of mean-motion resonances in the system. Ragozzine & Brown (2009) determined the orbits and masses of Haumea's satellites using astrometry from Hubble Space Telescope and the W. M. Keck Telescope. They used a three-body model and found that their data was not sufficient to constrain the oblateness, described by J_2, of the non-spherical central body. Their orbital solutions yielded a large eccentricity ($\sim$0.249) of the inner, fainter satellite, Namaka, and a mutual inclination with the outer satellite, Hi'iaka, of $\sim$13.41 degrees. They postulated that the excited state of the system could be conceptually explained by the satellites' tidal evolution through mean-motion resonances. In the main belt, Winter et al. (2009) studied the orbital stability of the satellites in the Sylvia triple system and Marchis et al. (2010) presented a dynamical solution of Eugenia and its two satellites.

2. Observations and Methods

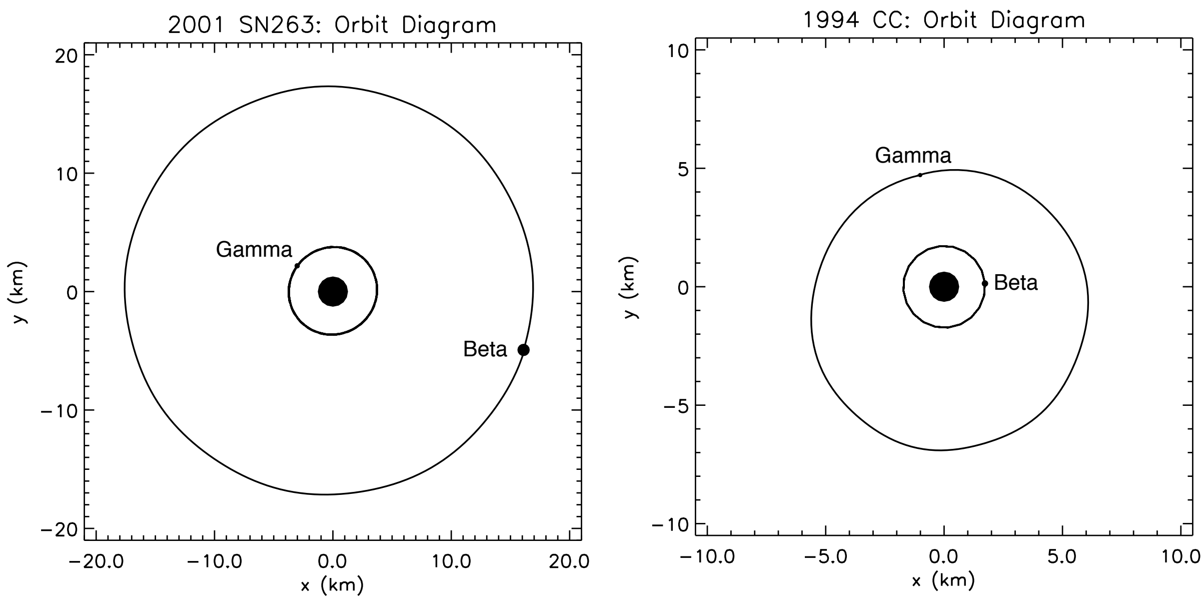

Fig. 1.— 2001 SN263 and 1994 CC: Best-fit orbit diagrams of the inner and outer satellites, projected onto Alpha's equatorial plane. In both diagrams, we show the actual trajectories from numerical integrations, and the relative sizes of the bodies (estimated from radar images) are shown to scale. All bodies are located at their positions at MJD 54509 (for 2001 SN263) and MJD 54994 (for 1994 CC) with Alpha centered on the origin. The slightly irregular shape of the orbit of 1994 CC's outer body is real and due to mutual perturbations in the system.

To arrive at three-body orbit solutions for 2001 SN263 and 1994 CC, we used radar observations from Arecibo and Goldstone. Specifically, these observables include the range and Doppler separations between Alpha and Beta (or Gamma) at multiple epochs. Range-Doppler separations were measured as the center of mass (COM) differences between Beta (or Gamma) and Alpha. For 2001 SN263, we modeled the shapes of the components (Hudson 1993; Magri et al. 2007) and differenced the COM estimates. For 1994 CC, the COMs were estimated visually, using the center of the trailing edge of the echo as an estimate of the COM location, and taking range smear into account when necessary. Measurement uncertainties were based on the image resolution. Our fits with reduced chi-square less than unity (see Section 3) indicate that uncertainties were assigned conservatively. For 2001 SN263, we used Arecibo observations taken over a span of approximately 14 days from the Modified Julian Date (MJD = JD - 2400000.5) 54508.06138 to MJD 54522.12406 when the triple made a close approach with Earth at 0.066 AU ($\sim$1550 $R_\oplus$). Range uncertainties are 75-150 meters and Doppler uncertainties are about 0.6 Hz at the nominal 2380 MHz frequency of the Arecibo radar (in this work, all Doppler observations and uncertainties are reported relative to this reference frequency). For 1994 CC, our observations were taken from both Arecibo and Goldstone planetary radars and spanned a total interval of almost 7 days from MJD 54994.69293 to MJD 55001.53906 during a close approach with Earth at 0.017 AU ($\sim$400 $R_\oplus$). The range uncertainties were 30-40 meters for Goldstone data and 25-75 meters for Arecibo data, and the Doppler uncertainties were 0.15-0.20 Hz for Goldstone data and 0.20-0.40 Hz for Arecibo data. In total, for 2001 SN263 we obtained 128 ranges and 128 Doppler measurements for each satellite, and for 1994 CC we had 112 ranges and 112 Doppler measurements for Beta and 78 ranges and 78 Doppler measurements for Gamma. Observations are available upon request.

Using these observations, the orbits, masses, and J_2 values of 2001 SN263 and 1994 CC were obtained using a model that includes the mutual gravitational interactions of all three bodies. To calculate the orbital evolution of the triples' components to fit to observations, we used a general Bulirsch-Stoer algorithm from an N-body integrator package called `MERCURY`, version 6.2 (Chambers 1999). The Bulirsch-Stoer algorithm, although slow, was chosen for its computational accuracy. For our long-term integrations to test for stability, we used a fast hybrid symplectic/Bulirsch-Stoer algorithm, also part of the `MERCURY` package. Since the satellites for both systems are deep in the potential wells of their respective central bodies, we ignored perturbations from the Sun and planets during the orbit-fitting process. The Hill radius $r_{\rm Hill}$ of the central body (2001 SN263: ∼345 km, 1994 CC: ∼86 km), defined as the spherical region where the central body's gravity dominates the attraction of its satellites compared to the Sun, is much larger than the outer satellite's semi-major axis a (2001 SN263: ∼16.6 km, 1994 CC: ∼6.1 km) in both systems. For 2001 SN263, $a_{\rm inner}/r_{\rm Hill}$ is 0.011 and $a_{\rm outer}/r_{\rm Hill}$ is 0.048. In the case of 1994 CC, $a_{\rm inner}/r_{\rm Hill}$ is 0.020 and $a_{\rm outer}/r_{\rm Hill}$ is 0.071. The assumption that we can ignore effects from external bodies breaks down during the long-term evolution of these triples and during close planetary encounters, which we address in Section 4.

2.1. Short-Term Integrations: Orbit Fitting

Solving for the orbits, masses, and J_2 of the triple systems is a highly non-linear least-squares problem that requires 16 parameters, which we fitted simultaneously. This included two sets of six osculating orbital elements (semi-major axis, eccentricity, inclination, argument of pericenter, longitude of the ascending node, and mean anomaly at epoch), three masses, and a J_2 for the central body. To solve this minimization problem, we attempted to search for a global minimum using the Levenberg-Marquardt algorithm `mpfit` (Markwardt 2008), written in IDL. We ran `mpfit` with thousands of initial conditions to search for the best-fitting parameters.

For both systems, we constrained some parameters with upper and lower bounds (Table 1), and all others were allowed to float without restraint. The initial guesses for orbital parameters and masses were guided by hundreds of two-body Keplerian solutions, but substantially augmented from these to explore wide regions of parameter space including "outlier" cases to be sure we covered all of the possibilities. Tables 2 and 3 show the ranges

Table 1: Orbit Model Constraints

	2001 SN263	1994 CC
Central Mass (kg)	10^{10} - none	10^{10} - none
Beta (kg)	10^{9} - none	10^{7} - none
Gamma (kg)	10^{7} - none	10^{6} - none
a (km)	0 - none	0 - none
e	0 - 0.9	0 - 0.9
J_2	0 - 0.25	0 - 0.25

These are a priori constraints that put limits on fitted parameters, so that a parameter can be bounded on the lower and/or upper side during the fitting process. The lower bounds on the masses were obtained by using size estimates from radar images and unit density, then dividing by a conservative factor of $\sim$100. In this table, 'none' means that no limit was set and the parameter was allowed to float without limits in that direction.

of starting guesses for our minimization routine as well as the maximum stepsize intervals between trial values. Typical stepsizes were significantly smaller than the maximum values listed. For the starting J_2 value of the central body, we adopted current estimates of axial ratios from shape modeling efforts (Nolan et al., in prep., Brozovic et al., in prep.) and a uniform density assumption. This resulted in initial J_2 values of 0.016 for 2001 SN263 and 0.013 for 1994 CC.

The non-spherical nature of the central body (Alpha) introduces additional non-Keplerian effects. The distribution of mass within Alpha can be represented by the J_n terms in its gravitational potential (Murray & Dermott 1999), where the largest contribution is due to the lowest-order gravitational moment, the quadrupole term J_2 (there is no n=1 term since the origin of coordinates is Alpha's center of mass). J_2 is a good approximation for describing the oblateness of primary bodies with substantial axial symmetry and as a result, we ignored higher-order terms. As we will see, even J_2 is not well-constrained, so there was no need to go to higher-order terms. It is related to three moments of inertia, A, B, and C, of the central body (Murray & Dermott 1999):

$$J_2 = \frac{C - \frac{1}{2}(A+B)}{MR^2} \approx \frac{C-A}{MR^2} \tag{1}$$

where M is the total mass and R is Alpha's equatorial radius. J_2 is an observable quantity because the oblateness of a body modifies the gravitational field experienced by orbiting satellites; in our case, the orbits of Beta and Gamma precessed through space as a consequence of Alpha's J_2.

In most cases, we aligned Alpha's pole direction with the normal to Beta's orbital plane, consistent with the generally accepted formation process by spin-up and mass shedding (Margot et al. 2002; Pravec et al. 2006; Walsh et al. 2008). To be thorough, we also searched for situations where Alpha's pole might not be aligned with Beta's orbit normal by surveying a comprehensive range of right ascension (RA) and declination (DEC) values for Alpha's pole orientation. We also performed numerical integrations where we set the

Table 2: 2001 SN263: Range of Initial Conditions

	Alpha	Maximum Stepsize
Mass (10^{10} kg)	850 - 980	$\lesssim$20
J_2	0.0001 - 0.09	$\lesssim$0.03
	Gamma (Inner)	Maximum Stepsize
Mass (10^{10} kg)	1 - 20	$\lesssim$6
a (km)	3.5 - 6.0	$\lesssim$2.2
e	0 - 0.4	$\lesssim$0.3
	Beta (Outer)	Maximum Stepsize
Mass (10^{10} kg)	7 - 100	$\lesssim$38
a (km)	16 - 24	$\lesssim$6.8
e	0 - 0.4	$\lesssim$0.3

Ranges of initial conditions with the maximum stepsize, defined as the largest interval between two consecutive initial values. Most stepsizes were significantly smaller than those listed. All angles were examined over their full range with typical stepsizes of 5-10 degrees.

value of J_2 to fixed values (i.e. 0.005, 0.010, 0.015) such that it was no longer a floating parameter, which reduced the number of parameters to 15. In the particular case of 1994 CC, we also iterated through a list of pole orientations for Alpha suggested by the shape modeling process (Brozovic et al., in prep.). With these poles, we explored another vast grid of starting parameters. This resulted in thousands of additional fits; however, the vast majority of them yielded poor fits or converged to unlikely J_2 values.

Using the `MERCURY` integrator, we chose a timestep interval (~1500 seconds for 2001 SN263 and ~4000 seconds for 1994 CC) such that the maximum interpolation error (calculated by comparing interpolated values with those from an integration with one-second timesteps) was at least an order of magnitude less than the smallest observation uncertainty. Cubic spline interpolation was performed to compute state vectors of the satellites at the exact observation epochs to enable comparison with observational data. For both triple systems, these timesteps were small enough to resolve at least 1/25 of the inner body's orbit. Using the integrator, we were able to obtain the positions and velocities of the satellites with respect to the central body, Alpha, as a function of time. We used line-of-sight vector orientations from the JPL HORIZONS system to project these positions and velocities and to calculate the range and Doppler separations at every observation epoch for each satellite. Comparison between observed and computed range and Doppler values then yielded a measure of the goodness-of-fit according to

$$\chi^2 = \sum_i \frac{(O_i - C_i)^2}{\sigma_i^2} \tag{2}$$

where χ^2 is the chi-square obtained by summing over i comparisons: O and C are the observed and computed values and σ is the observation uncertainty.

Solutions with Gamma more massive than Beta were eliminated because they are inconsistent with radar size estimates. In our list of best fits, for 2001 SN263 our lowest reduced chi-square was ~0.093 with 496 degrees of freedom (DOF), and in the case of 1994 CC, our lowest reduced chi-square was ~0.27 with 364 degrees of freedom. The likely cause of a reduced chi-square less than 1 is the overestimation of observation uncertainties. We

Table 3: 1994 CC: Range of Initial Conditions

	Alpha	Maximum Stepsize
Mass (10^{10} kg)	10 - 75	$\lesssim$25
J_2	0.0001 - 0.09	$\lesssim$0.03
	Beta (Inner)	**Maximum Stepsize**
Mass (10^{10} kg)	0.05 - 3	$\lesssim$1
a (km)	0.5 - 4	$\lesssim$2
e	0 - 0.6	$\lesssim$0.5
	Gamma (Outer)	**Maximum Stepsize**
Mass (10^{10} kg)	0.0008 - 0.5	$\lesssim$0.3
a (km)	3 - 15	$\lesssim$5
e	0 - 0.7	$\lesssim$0.5

Ranges of initial conditions with the maximum stepsize, defined as the largest interval between two consecutive initial values. Most stepsizes were significantly smaller than those listed. All angles were examined over their full range with typical stepsizes of 5-10 degrees.

considered only those solutions within a 1-σ increase in the lowest reduced chi-square value (Press et al. 1992):

$$\chi^2_{\nu,1\sigma} = \chi^2_{\nu,\min} + \chi^2_{\nu,\min} * \frac{\sqrt{2 * \mathrm{DOF}}}{\mathrm{DOF}} \tag{3}$$

where $\chi^2_{\nu,1\sigma}$ represents the chi-square value calculated from a 1-σ increase of the minimum chi-square value $\chi^2_{\nu,\min}$. This resulted in $\chi^2_{\nu,1\sigma} \sim 0.1$ for 2001 SN263 and $\chi^2_{\nu,1\sigma} \sim 0.29$ for 1994 CC. Such criteria further narrowed our list of fits, but contained solutions that were near-duplicates. For ease of presentation we marked and removed nearly duplicate fits that met both of the following conservative criteria: differences in masses (Alpha, Beta, and Gamma) were less than 2% and differences in orbital orientations were less than 5 degrees. The other orbital elements were relatively consistent, and we did not incorporate them into the filter.

2.2. Long-Term Integrations: Stability

To further discriminate between our remaining least-squares solutions and to study stability, we looked at their orbital evolution over time through long-term integrations. Only orbital solutions that were stable over the course of longer-term numerical integrations were regarded as satisfactory solutions. Since the dynamical lifetimes of these asteroids are ~10 Myrs (Gladman et al. 1997), we ran extensive stability tests (~5 Myrs) for our remaining orbital fits. This resulted in a subset of likely solutions that met our constraints. The timestep interval was chosen such that we could resolve at least 1/20 of the inner body's orbit for both triple systems, which is small enough to capture the dynamics of the system. In these long-term integrations, we incorporated collisions and ejections using a hybrid symplectic/Bulirsch-Stoer algorithm.

To include collisions, it was necessary to specify physical sizes for all components. For Alpha, we used their known radii: for 2001 SN263, R ~ 1.3 km (Nolan et al. 2008b) and for 1994 CC, R ~ 315 m (Brozovic et al. 2010). For Beta and Gamma we used our mass solutions and scaled from Alpha assuming identical bulk densities.

Ejections were defined as events where the satellite was no longer within 1 Hill radius of Alpha. The Hill radius equation for Alpha is the following:

$$r_{\mathrm{Hill}} = a_{\odot} \left(\frac{M_{\mathrm{Alpha}}}{3M_{\odot}} \right)^{1/3} \tag{4}$$

where M_{Alpha} and $M_{\odot}$ represent the masses of Alpha and the Sun, respectively, and $a_{\odot}$ is Alpha's semi-major axis with respect to the Sun.

2.3. Precession Rates

Non-Keplerian effects potentially provide powerful constraints on component masses. We measured the precession rates of our best-fit solutions and compared them to analytical expressions of the precession due to an oblate primary and secular perturbations. For primary oblateness described by J_2, the analytical expressions are (Murray & Dermott 1999):

$$\frac{d\omega}{dt} \approx \frac{3}{2} \frac{nJ_2}{(1-e^2)^2} \left(\frac{R}{a} \right)^2 \left(\frac{5}{2} \cos^2 I - \frac{1}{2} \right) \tag{5}$$

$$\frac{d\Omega}{dt} \approx -\frac{3}{2} nJ_2 \left(\frac{R}{a} \right)^2 \frac{\cos I}{(1-e^2)^2} \tag{6}$$

where ω and Ω represent the argument of pericenter and the longitude of the ascending node, respectively. The precession rate for the longitude of pericenter is simply the sum of the rates for the argument of pericenter and longitude of the ascending node. The other variables are defined as follows: n is the mean motion of the satellite, J_2 is the unitless quantity describing the oblateness of the central body, e is the eccentricity, R is the radius of the central body in the same units as the satellite's semi-major axis a, and I is the orbital inclination with respect to Alpha's equator.

We also calculated the analytical precession rates due to secular perturbations. Over long timescales and in the absence of any mean-motion resonances or additional perturbations, the secular equations adequately describe the evolution of orbital elements. The secular equations can be obtained by examining the solution to Lagrange's equations corresponding to the secular part (terms that do not depend on the mean longitudes of either body) of the disturbing function, which describes a body's gravitational perturbations by other bodies (Murray & Dermott 1999). The secular equations can be written with convenient variables:

$$h_j = e_j \sin(\varpi_j) \qquad p_j = I_j \sin(\Omega_j) \tag{7}$$

$$k_j = e_j \cos(\varpi_j) \qquad q_j = I_j \cos(\Omega_j) \tag{8}$$

where h, k, p, and q are new variables as defined above, e is the eccentricity, ϖ is the longitude of pericenter, I is the inclination with respect to Alpha's equator, Ω is the longitude of the ascending node, and j denotes the body being perturbed. Their solutions are of the following form:

$$h_j = \sum_{i=1}^{2} e_{ji} \sin(g_i t + \beta_i) \quad p_j = \sum_{i=1}^{2} I_{ji} \sin(f_i t + \gamma_i) \tag{9}$$

$$k_j = \sum_{i=1}^{2} e_{ji} \cos(g_i t + \beta_i) \quad q_j = \sum_{i=1}^{2} I_{ji} \cos(f_i t + \gamma_i) \tag{10}$$

where i denotes the eigenmodes, g_i and f_i represent the eigenfrequencies, and β_i and γ_i are the phases (Murray & Dermott 1999). From these secular solutions, we were able to calculate $e(t)$, $\varpi(t)$, $I(t)$, and $\Omega(t)$ to find the analytical precession rates corresponding to secular theory.

Our measurements of the precession rates used our best-fit solutions to the observations. We numerically integrated these solutions to detect the evolution of the argument of pericenter, longitude of ascending node, and longitude of pericenter for both satellites in each system. Due to fast, short-term fluctuations in the orbital elements as a function of time, it was necessary to perform linear regressions to obtain estimates of the rates over typical timescales of 100s of days. In the case of 2001 SN263 Beta, we looked at longer timescales of thousands of days due to its relatively slow precession. Since the rates also changed over time, we computed them near the epoch at which we solved for the orbits. By measuring the numerical rates at which these orbital elements precess, we were able to compare them with those calculated from analytical methods above, which included J_2 and secular contributions.

2.4. Resonances

We searched for mean-motion resonances between Beta and Gamma in both systems. To do this, we first looked for integer values (-150 to +150) of j_1 and j_2 where the following resonant argument varied “slowly” (<100 deg/day):

$$\phi \approx j_1 n_2 + j_2 n_1 \tag{11}$$

where n_1 and n_2 denote the mean motions of the inner and outer bodies, respectively. For values of j_1 and j_2 that met our first criterion, we searched through integer values (-30 to +30) of j_3, j_4, j_5, and j_6 for which there was libration of the general resonant argument (Murray & Dermott 1999):

$$\phi = j_1\lambda_2 + j_2\lambda_1 + j_3\varpi_2 + j_4\varpi_1 + j_5\Omega_2 + j_6\Omega_1 \tag{12}$$

where λ is the mean longitude, ϖ is the longitude of pericenter, and Ω is the longitude of the ascending node. The d’Alembert relation:

$$\sum_{i=1}^{6} j_i = 0 \tag{13}$$

describes how the integer values of j_i ($1 \leq i \leq 6$) are related. Lastly, we repeated the second criterion for different permutations of the satellites’ mean longitudes representing the highest and lowest possible values that captured the full range of uncertainties on mean motions.

3. Orbit-Fitting Results

In this section, we describe the best-fit orbital solutions that passed the constraints described in Table 1 and Section 2. Our initial fits resulted in 174 and 901 possible solutions within a 1-σ increase in the lowest reduced chi-square value for 2001 SN263 and 1994 CC, respectively. Of these, 53 and 582 were eliminated by the mass bounds, J_2 constraints, and duplicate filtering. After further eliminating solutions that did not meet our long-term integration criterion, we were left with a list of stable solutions for both systems (2001 SN263: 113 fits, 1994 CC: 262 fits), which were used for post-orbit-fitting determinations of orbital parameter uncertainties. The majority of our unstable fits reached instability quickly–typically within 1000 years for both systems.

A significant fraction (2001 SN263: ∼25%; 1994 CC: ∼45%) of our fits resulted in a retrograde orbit of either Beta or Gamma (orbital direction opposite to Alpha's spin direction). This occurred because we were able to fit the data with a wide range of spin axis orientations for Alpha even though the orbital orientations of Beta and Gamma were fairly well determined. While it is more likely that the orbits of Beta and Gamma are prograde with respect to Alpha, some of our retrograde solutions are stable over ∼Myrs (in the case of no external perturber) and at this point we cannot rule them out.

Diagrams showing the best-fit orbits of the satellites in 2001 SN263 and 1994 CC projected onto Alpha's equatorial plane are shown in Figure 1. The best-fit models match the data well (Figures 2 and 5), where the residuals shown are defined as (observation - model)/uncertainty. For both triples, the total angular momentum budget (orbital and spin) is dominated by Alpha's spin angular momentum. For 2001 SN263, Alpha contributes 77%, Gamma (inner body) contributes 4%, and Beta (outer body) contributes 19% of the total angular momentum. For 1994 CC, Alpha contributes 85%, Beta (inner body) contributes 12%, and Gamma (outer body) contributes 3% of the total angular momentum. In both systems, ∼97% of the angular momentum is contained in the spin of Alpha and the orbit of Beta, which justifies a posteriori our decision to align Beta's orbit with Alpha's equatorial plane, consistent with a spin-up formation process.

3.1. 2001 SN263

The best-fit parameters (Table 4) are valid at the epoch MJD 54509.0, where the reduced chi-square for this orbital solution is $\chi^2_\nu = 0.099$ (DOF = 496). While a sizeable fraction

Table 4: 2001 SN263: Best-Fit Parameters and Formal 1-σ Errors

	Gamma (inner)	Beta (outer)
Mass (10^{10} kg)	9.773 $\pm$ 3.273	24.039 $\pm$ 7.531
a (km)	3.804 $\pm$ 0.002	16.633 $\pm$ 0.163
e	0.016 $\pm$ 0.002	0.015 $\pm$ 0.009
i (deg)	165.045 $\pm$ 12.409	157.486 $\pm$ 1.819
ω (deg)	292.435 $\pm$ 53.481	131.249 $\pm$ 21.918
Ω (deg)	198.689 $\pm$ 61.292	161.144 $\pm$ 13.055
M (deg)	248.816 $\pm$ 11.509	212.658 $\pm$ 10.691
P (days)	0.686 $\pm$ 0.00159	6.225 $\pm$ 0.0953
		Alpha (central body)
Mass (10^{10} kg)		917.466 $\pm$ 2.235
J_2		0.013 $\pm$ 0.008
Pole Solution (deg)		RA: 71.144 $\pm$ 13.055
		DEC: -67.486 $\pm$ 1.819

The masses are listed in 10^{10} kg, a is the semi-major axis, e is the eccentricity, i is the inclination, ω is the argument of pericenter, Ω is the longitude of the ascending node, M is the mean anomaly at epoch, and P is the period. These orbital elements are valid at MJD 54509 in the equatorial frame of J2000. Alpha's pole solution is given in right ascension (RA) and declination (DEC). This table lists formal 1-σ statistical errors; see text for adopted 1-σ uncertainties.

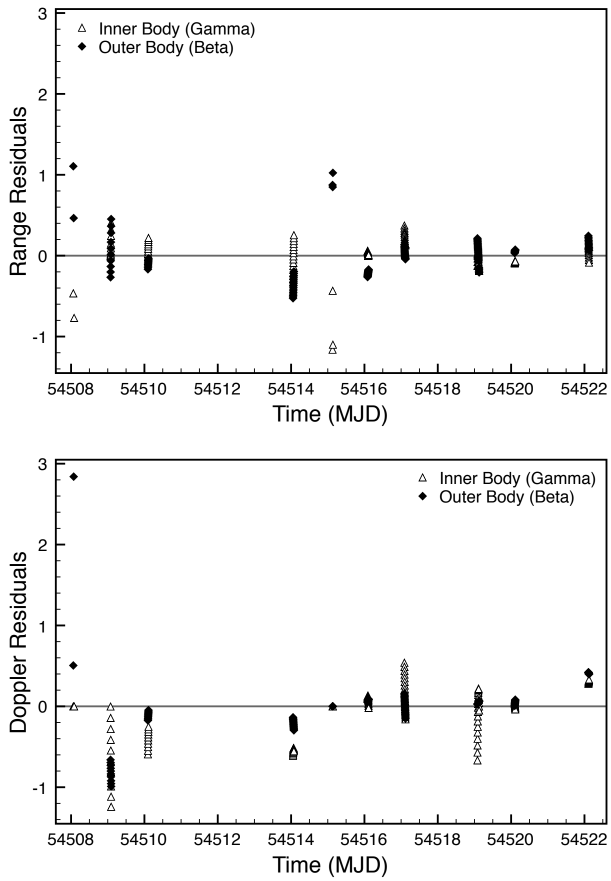

Fig. 2.— 2001 SN263 Best-Fit Solution: Range and Doppler Residuals. The second Doppler residual at MJD 54508.0708 is a clear outlier. We obtained similar solutions whether we included this data point or not. We also note that there seems to be an apparent sinusoidal signature in the residuals for 2001 SN263, which may indicate that our model is not capturing the full dynamics of the system. Other good orbital solutions with plausible mass ratios and J_2 values also produce similar residuals.

of our orbital fits had a lower chi-square, the adopted solution described in this section and Table 4 has the most plausible combination of Beta/Gamma mass ratio and J_2 value (lower chi-square solutions with a Beta/Gamma mass ratio less than 2 or a J_2 of 0 were not considered based off of radar size and shape estimates). For discussion regarding masses and J_2, see Section 3.3. The formal 1-σ errors listed in Table 4 certainly underestimate the actual errors; here we list plausible 1-σ uncertainties alongside parameter values with guard digits by examining the range of parameter values in our 113 acceptable fits. The mass of Alpha is $917.466^{+19}_{-5} \times 10^{10}$ kg, and the masses of Gamma and Beta are $9.773 \pm 7 \times 10^{10}$ and $24.039^{+7}_{-17} \times 10^{10}$ kg, respectively. Using preliminary size estimates from radar images, we calculate a density of $\sim$0.997 g/cm^3 for Alpha. If we apply Alpha's density to the range of satellite masses that are within uncertainties, their equivalent radii range from 188 - 342 m for Gamma and 213 - 420 m for Beta.

The orbit of Gamma has a semi-major axis of $3.804^{+0.01}_{-0.02}$ km and an eccentricity of $0.016^{+0.005}_{-0}$. The orbit of Beta is also nearly circular with an eccentricity of $0.015^{+0.022}_{-0.010}$ and a semi-major axis of $16.633^{+0.39}_{-0.38}$ km. The orbital periods of Gamma and Beta are 0.686 ± 0.01 and 6.225 ± 0.5 days, respectively. Assuming that Beta orbits in Alpha's equatorial plane, the mutual inclination between the satellites' orbital planes is $\sim$14 degrees. We estimate orbit pole angular uncertainties of $\sim$10 degrees for Beta and $\sim$15 degrees for Gamma. Alpha's floating J_2 value converged to $0.013^{+0.050}_{-0.013}$.

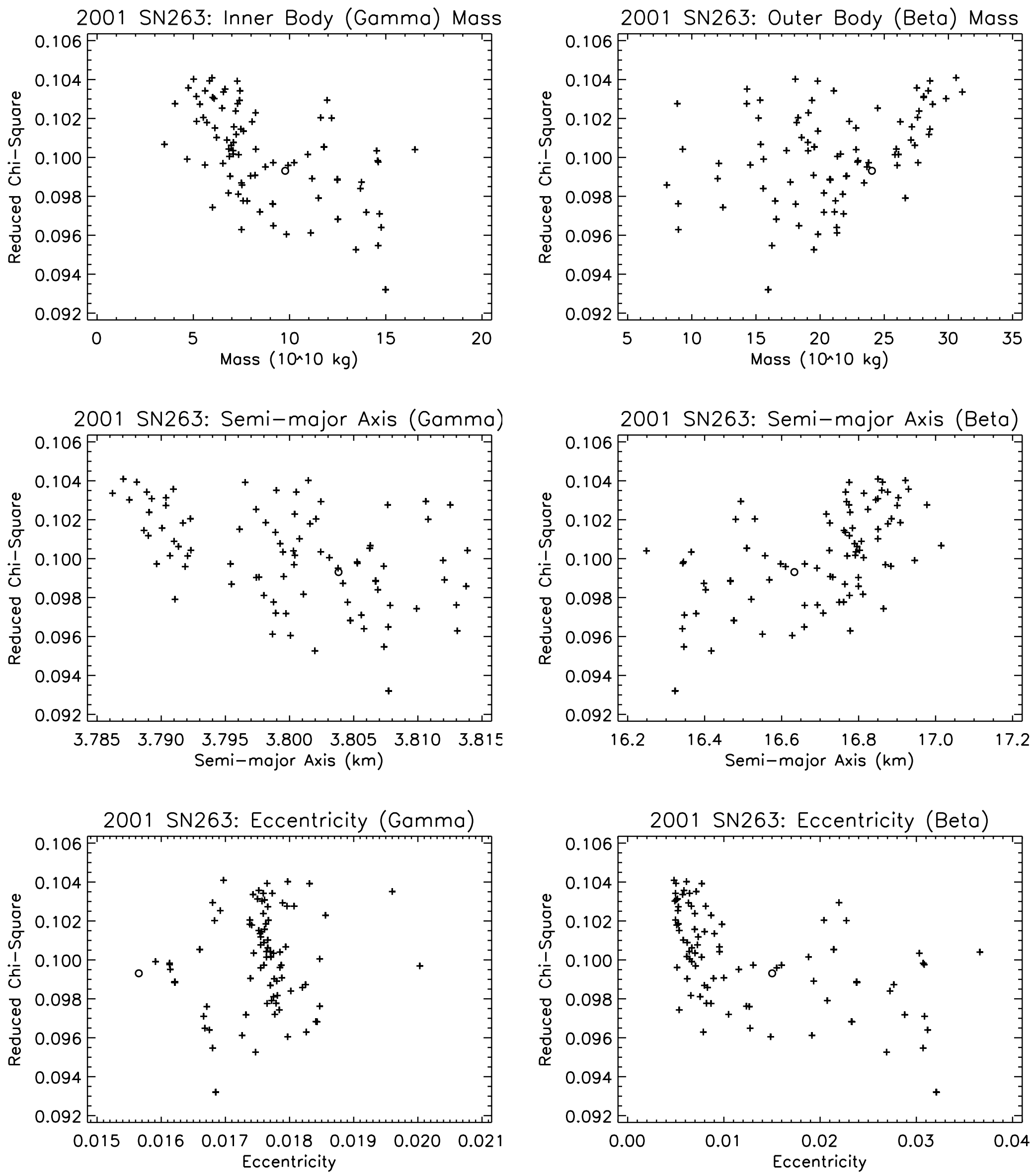

Fig. 3.— 2001 SN263: Reduced chi-square as a function of orbital parameters: mass, semi-major axis, and eccentricity. The points plotted here include the statistically equivalent best-fit orbital solutions that passed the constraints listed in Table 1 and Section 2. Our adopted value is shown as an open circle, and solutions with lower chi-squares were ruled out on the basis of implausible J_2 and Beta/Gamma mass ratios.

Table 5: 2001 SN263 Precession Rates

Quantity	**Gamma (inner)**				**Beta (outer)**			
	Analytical:			Numerical	Analytical:			Numerical
	Secular	J_2	Total	Total	Secular	J_2	Total	Total
$\dot{\omega}$ (deg/day)	0.314	2.239	2.552	2.466	0.110	0.014	0.124	0.093
$\dot{\Omega}$ (deg/day)	-0.167	-1.171	-1.338	-1.295	-0.081	-0.007	-0.087	-0.063
$\dot{\varpi}$ (deg/day)	0.146	1.068	1.214	1.120	0.030	0.007	0.037	0.030

This table includes the argument of pericenter rate $\dot{\omega}$, the longitude of the ascending node rate $\dot{\Omega}$, and the longitude of pericenter rate $\dot{\varpi}$. For each satellite, the first 3 columns represent our analytical calculations and the fourth column shows our measured numerical rates.

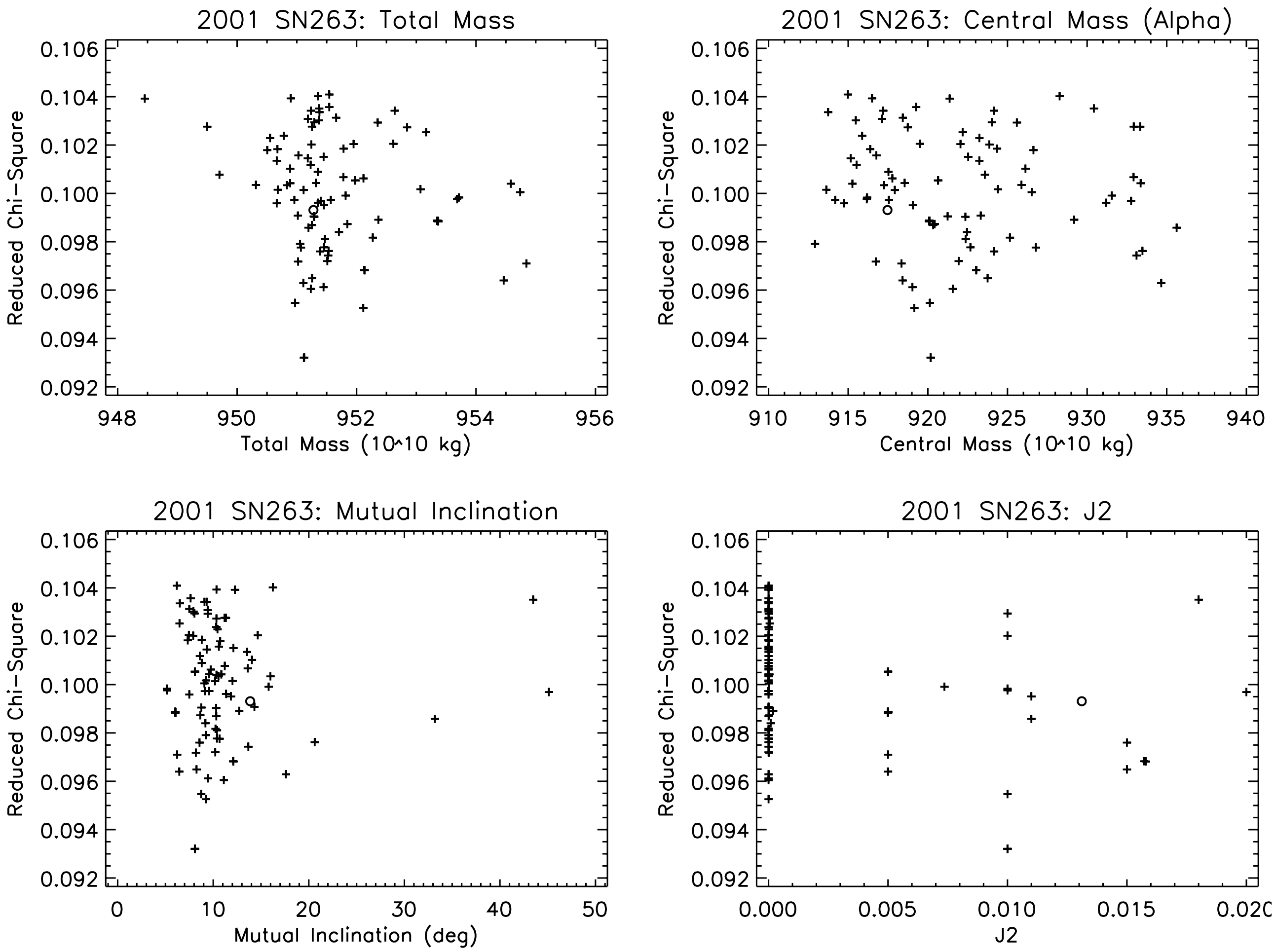

Fig. 4.— 2001 SN263: Reduced chi-square as a function of masses, mutual inclination, and J_2. The points plotted here include the statistically equivalent best-fit orbital solutions that passed the constraints listed in Table 1 and Section 2. Our adopted value is shown as an open circle, and solutions with lower chi-squares were ruled out on the basis of implausible J_2 and Beta/Gamma mass ratios.

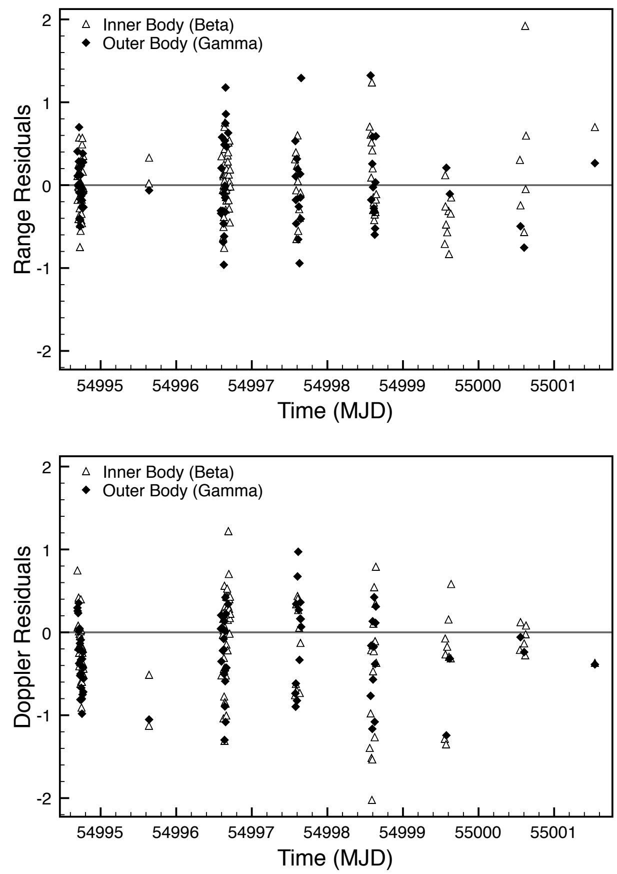

Fig. 5.— 1994 CC Best-Fit Solution: Range and Doppler Residuals.

Plots showing our statistically equivalent (within 1-σ level) best fits are shown in Figures 3 and 4. It is clear from these plots that we can fit the data with a range of parameters. For the set of orbital parameters and masses listed in Table 4, we measured precession rates from numerical integrations and calculated analytical precession rates (Table 5) for each satellite, where the analytical contributions consist of secular and J_2 calculations. The secular eigenfrequencies are $g_1 \sim 0.138$ deg/day (or period of 7.2 years), $g_2 \sim 0.024$ deg/day (period of 41.9 years), $f_1 \sim$ -0.161 deg/day (period of 6.1 years), and $f_2 \sim 0$ deg/day. Overall, there is good agreement between analytical estimates and the rates observed from numerical integrations. Our analytical precession rates are affected by uncertainties in orbital parameters, mainly by those in semi-major axes. Although precession measurements can potentially provide powerful constraints on component masses and primary oblateness, the limited observational span prevents us from making stronger conclusions.

Table 6: 1994 CC: Best-Fit Parameters and Formal 1-σ Errors

	Beta (inner)	Gamma (outer)
Mass (10^{10} kg)	0.580 ± 0.331	0.091 ± 1.644
a (km)	1.729 ± 0.008	6.130 ± 0.108
e	0.002 ± 0.015	0.192 ± 0.014
i (deg)	83.376 ± 11.158	71.709 ± 8.994
ω (deg)	130.980 ± 43.647	96.229 ± 5.017
Ω (deg)	59.209 ± 3.910	48.479 ± 4.741
M (deg)	233.699 ± 43.941	6.070 ± 6.187
P (days)	1.243 ± 0.0329	8.376 ± 0.404
		Alpha (central body)
Mass (10^{10} kg)		25.935 ± 1.315
J_2		0.014 ± 0.383
Pole Solution (deg)		RA: -30.791 ± 3.910
		DEC: 6.624 ± 11.158

The masses are listed in 10^{10} kg, a is the semi-major axis, e is the eccentricity, i is the inclination, ω is the argument of pericenter, Ω is the longitude of the ascending node, M is the mean anomaly at epoch, and P is the period. These orbital elements are valid at MJD 54994 in the equatorial frame of J2000. Alpha's pole solution is given in right ascension (RA) and declination (DEC). This table lists formal 1-σ statistical errors; see text for adopted 1-σ uncertainties.

Table 7: 1994 CC Precession Rates

Quantity	Beta (inner)				Gamma (outer)			
	Analytical:			Numerical	Analytical:			Numerical
	Secular	J_2	Total	Total	Secular	J_2	Total	Total
$\dot{\omega}$ (deg/day)	-0.612	0.392	-0.219	-0.058	0.135	0.005	0.139	0.131
$\dot{\Omega}$ (deg/day)	-0.043	-0.196	-0.239	-0.143	-0.068	-0.002	-0.070	-0.072
$\dot{\varpi}$ (deg/day)	-0.655	0.196	-0.459	-0.202	0.067	0.002	0.069	0.061

This table includes the argument of pericenter rate $\dot{\omega}$, the longitude of the ascending node rate $\dot{\Omega}$, and the longitude of pericenter rate $\dot{\varpi}$. For each satellite, the first 3 columns represent our analytical calculations and the fourth column shows our measured numerical rates.

3.2. 1994 CC

The best-fit parameters at MJD 54994.0 yield a reduced chi-square of 0.27 (Table 6) with DOF = 364. While there are orbital fits with lower chi-squares, the particular solution described in this section and Table 6 has the most plausible combination of Beta/Gamma mass ratio and J_2 value. See Section 3.3 for discussion regarding masses and J_2. As is the case for 2001 SN263, some of the formal 1-σ errors in Table 6 are likely to be underestimates of the actual uncertainties in the parameter values, and here we list our adopted 1-σ uncertainties from examining our best-fit solutions along with parameter values with guard digits. The mass of Alpha is $25.935 \pm 1 \times 10^{10}$ kg, Beta is $0.580^{+0.3}_{-0.5} \times 10^{10}$ kg, and Gamma is $0.0911^{+0.20}_{-0.09} \times 10^{10}$ kg. We estimate a density of $\sim$1.98 g/cm^3 for Alpha, given its preliminary size estimate from radar images. If we apply Alpha's density to the range of Beta and Gamma masses that are acceptable (within uncertainties), we find that their equivalent radii can range from 46 - 102 m for Beta and 11 - 71 m for Gamma. Beta's orbit is nearly circular at $0.002^{+0.009}_{-0.002}$ with a semi-major axis of 1.729 ± 0.02 km and Gamma's orbit has an eccentricity of $0.192^{+0.015}_{-0.022}$ and a semi-major axis of $6.13^{+0.07}_{-0.12}$ km. The orbital periods of Beta and Gamma are 1.243 ± 0.1 and 8.376 ± 0.5 days, respectively. This fit converged to a J_2 value of $0.014^{+0.050}_{-0.014}$, where Alpha's pole was assumed to be aligned with Beta's orbit normal. From this orbital solution, we find a significant mutual inclination of $\sim$16 degrees. We estimate angular uncertainties of $\sim$20 degrees for Beta's orbit pole and $\sim$10 degrees for Gamma's orbit pole.

We show our statistically equivalent (within 1-σ level) best fits in Figures 6 and 7. For 1994 CC, we also compared precession rates (Table 7) between our numerical integrations and analytical calculations and find good agreement for the outer body, Gamma. There is appreciable disagreement for Beta, which will be discussed in Section 3.4. The secular eigenfrequencies are $g_1 \sim 0.016$ deg/day (or period of 60.1 years), $g_2 \sim 0.070$ deg/day (period of 14.1 years), $f_1 \sim 0$ deg/day, and $f_2 \sim$ -0.086 deg/day (period of 11.4 years). As is the case for 2001 SN263, our estimates of precession rates are affected by uncertainties in orbital parameters.

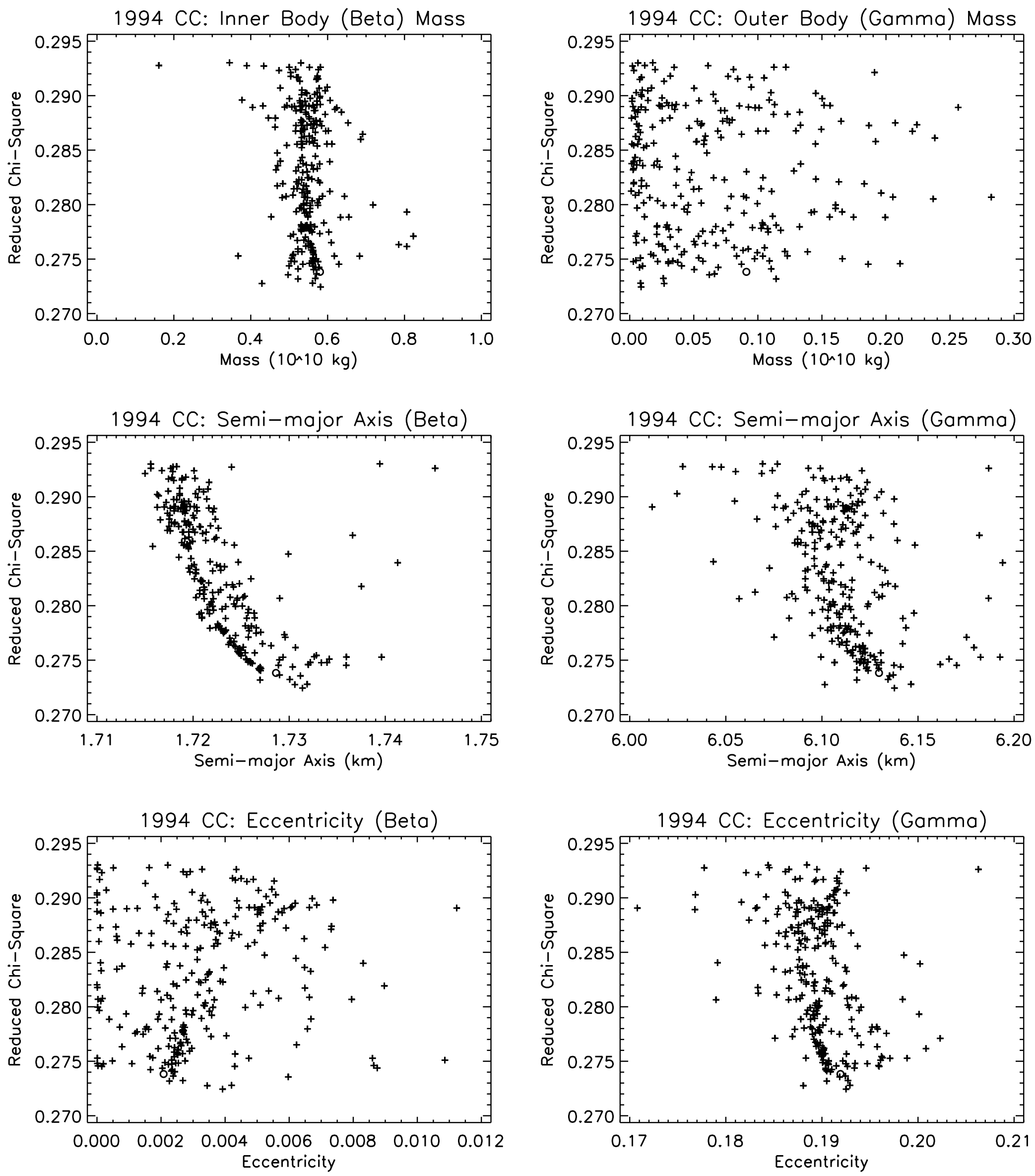

Fig. 6.— 1994 CC: Reduced chi-square as a function of orbital parameters: mass, semi-major axis, and eccentricity. The points plotted here include the statistically equivalent best-fit orbital solutions that passed the constraints listed in Table 1 and Section 2. Our adopted value is shown as an open circle, and solutions with lower chi-squares were ruled out on the basis of implausible J_2 and Beta/Gamma mass ratios.

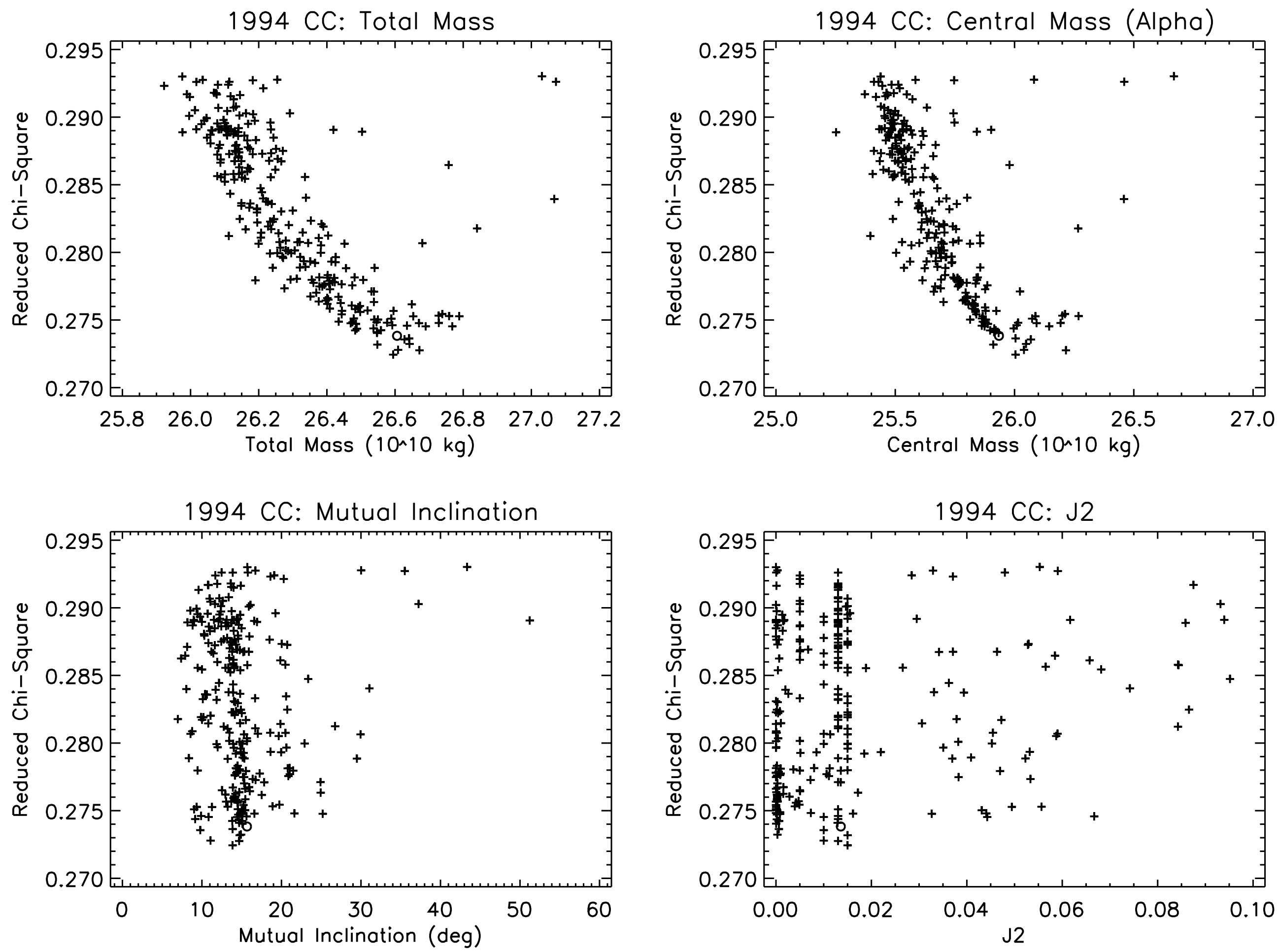

Fig. 7.— 1994 CC: Reduced chi-square as a function of masses, mutual inclination, and J_2. The points plotted here include the statistically equivalent best-fit orbital solutions that passed the constraints listed in Table 1 and Section 2. Our adopted value is shown as an open circle, and solutions with lower chi-squares were ruled out on the basis of implausible J_2 and Beta/Gamma mass ratios. There is structure seen in the J_2 plot due to fits where we constrained the J_2 parameter to be fixed at certain values: 0.005, 0.010, 0.013, and 0.015.

3.3. Masses and J_2

In the case of 2001 SN263, we are limited in our ability to measure the masses of the satellites because the majority of our low chi-square fits with reasonable mass ratios ($m_{\rm Beta} > m_{\rm Gamma}$) have a lower J_2 coefficient ($\sim$0) than the expected value ($\sim$0.016) from shape model estimates (Nolan et al., in prep.). Our fits with reasonable mass ratios typically occurred in integrations where we allowed J_2 to float as a parameter in our least-squares minimization routine, which usually resulted in a very low and unlikely J_2 value of 0. When we attempted to fix J_2 at a range of values, including our best estimate of J_2 from shape model estimates, our low chi-square solutions typically had implausible mass ratios where Gamma was more massive than Beta. Since our best fit shown in Table 4 has a reasonable value of J_2, it is possible that our mass for Beta is an underestimate of its true value. For 1994 CC, we also found orbital solutions where J_2 was driven to 0, but there was a greater fraction of fits with both reasonable mass ratios and J_2 values.

Nevertheless, in both systems we find a wide range of J_2 values (Figures 4 and 7) that produce orbital solutions with low chi-square results. As a result, we cannot constrain J_2 well with the current set of observations. One possibility is that there is a degeneracy between satellite mass (in particular, the outer satellite) and J_2, as suspected for Haumea by Ragozzine & Brown (2009). This behavior can be explained by examining our precession rates for the inner body. For 2001 SN263, we expect that both the mass of the outer satellite and the J_2 of the primary produce an advance of the inner body's longitude of pericenter (Table 5) and for 1994 CC, the effects of the mass of the outer satellite and the J_2 of the primary are opposite (Table 7), which can happen at certain phases of the secular evolution. It is difficult to apportion the respective contributions of the two quantities, J_2 and the mass of the outer body, to the precessional effects of the inner body. Further support for this idea comes from a comparison of the outer body's mass and J_2 values for the ensemble of our valid solutions. We find that the two quantities are appreciably anti-correlated (r = -0.48) for 2001 SN263, with the sum of the two contributions matching the measured rates. In the case of 1994 CC, a mild positive correlation was found between the outer body's mass and J_2 (r = 0.19).

Studies on near-Earth binary 1999 KW4 by Ostro et al. (2006) and Scheeres et al. (2006) have demonstrated some of the complex dynamics that can result from interactions between asymmetrically-shaped components. In particular, Cuk & Nesvorny (2010) found that the libration of an elongated asteroid satellite can result in a negative apsidal precession rate. Since this type of libration-induced precession may take place but is not included in our model, we speculate that the minimization procedure artificially lowers the value of the parameter J_2, which would normally result in a positive apsidal precession rate. Including libration-induced precession requires knowledge of the component shapes that is not available at this time; it is therefore beyond the scope of this paper.

3.4. Precession Rates: Numerical and Analytical Comparisons

There is good agreement in the precession rates for 2001 SN263 (Table 5) between those measured from numerical integrations and our analytical estimates, described in Section 2.3. For 1994 CC, we see good agreement between our analytical and numerical precession rates for the outer body, Gamma (Table 7). For the inner body (Beta), whose orbit lies in Alpha's equatorial plane, there is appreciable disagreement between the total values for the precession rates. We attribute this disagreement to the non-secular terms in the disturbing function; due to the infinite number of short-period terms in the disturbing function, there are differences between the results of our numerical integration and the predictions of secular analytical theory. We verified this by calculating the precession rates from numerical integrations with an outer body mass of near zero, which meant that any precession of the inner body must be due to J_2 only. Indeed, our inner body's precession rate ($\dot{\varpi} \approx 0.197$ deg/day) from numerical integrations with essentially no outer body closely matched the expected analytical precession ($\dot{\varpi} \approx 0.196$ deg/day) due to J_2 only. Thus, it is likely that any disagreement between our numerical and analytical values for Beta can be credited to non-secular terms in the disturbing function. We suspect that the reason we see this discrepancy between numerical and analytical rates for 1994 CC's Beta and not for the other bodies in these triple systems is the fact that the perturber in this case is Gamma, whose orbital plane is both eccentric as well as inclined to Alpha's equatorial plane and Beta's orbital plane.

3.5. Mean-Motion Resonance

The satellites of 2001 SN263 have an orbital period ratio near 9:1 using their nominal orbital elements. However, we did not find any librating resonant arguments over long, secular timescales for either system. We found cases where a resonant argument appeared to librate initially and then circulated thereafter; an example of this is shown in Figure 8 for 1994 CC. In this example, we see a distinct onset of circulation as a result of the secular precession of the longitudes of pericenter and the ascending node. Both of these longitudes are changing over time (see Table 7), causing the resonant argument in this situation to cease its apparent libration and to start circulating over all possible angles.

4. Orbital Origin and Evolution

It is interesting to find a non-zero eccentricity ($\sim$0.19) for 1994 CC's outer body, Gamma. Furthermore, our best orbital solutions yielded significant mutual inclinations (2001 SN263: $\sim$14 degrees, 1994 CC: $\sim$16 degrees) between the orbital planes of the satellites. Other known systems with a significant inclination include the main-belt asteroid triple (45) Eugenia, whose satellites have been reported to be inclined 9 and 18 degrees with respect to the primary's equator (Marchis et al. 2010) and the dwarf planet Haumea, whose two satellies have a mutual inclination of 13.41 degrees (Ragozzine & Brown 2009).

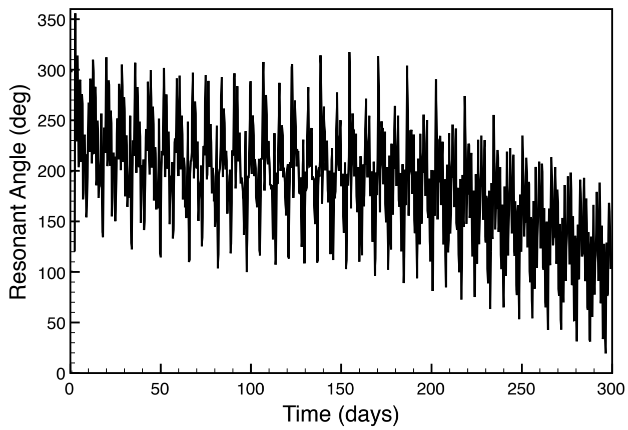

Fig. 8.— This figure shows a sample resonant argument for 1994 CC, where there initially appears to be libration (oscillating motion) followed by circulation through all angles.

Possible mechanisms to excite orbital eccentricity and inclination include Kozai resonance, evection resonance, mean-motion resonance crossings, close planetary encounters, and a combination of these effects. In the subsequent sections, we calculate the eccentricity and inclination damping timescales and investigate each of these possible mechanisms.

4.1. Eccentricity and Inclination Damping Timescales

Tidal damping of a synchronous satellite's orbit is a competing process between tides raised on the satellite by the primary (causing the eccentricity to decay) and tides on the primary due to the satellite (causing both the semi-major axis and eccentricity to grow). Tidal dissipation in the satellite's interior due to the primary can heat the satellite and circularize its orbit. The corresponding eccentricity damping timescale $\tau_{\mathrm{e,damp}}$ (Murray & Dermott 1999) is:

$$\tau_{\mathrm{e,damp}} = \frac{4}{63}\frac{m}{M}\left(\frac{a}{r}\right)^5\left(\frac{\tilde{\mu}_s Q_s}{n}\right) \tag{14}$$

and the competing timescale for tides raised on the primary is:

$$\tau_{\mathrm{e,excite}} = \frac{16}{171}\frac{M}{m}\left(\frac{a}{R}\right)^5\left(\frac{\tilde{\mu}_c Q_c}{n}\right) \tag{15}$$

where M is the central body's mass, m is the mass of the satellite, a is the semi-major axis, R is the central body's mean radius, r is the satellite's mean radius, $\tilde{\mu}$ is a measure of a body's rigidity, Q is the tidal dissipation function, and n is the mean motion. The subscripts c and s represent the central body and the satellite, respectively. The effective rigidity $\tilde{\mu}$, a unitless quantity as defined in Murray & Dermott (1999), is uncertain but can be estimated for gravitational aggregates ("rubble piles") as shown in Goldreich & Sari (2009): we find $\tilde{\mu}_s \sim 3.1 \times 10^6$ for Gamma ($r \sim 45$ m). The factor Q is even harder to determine, but available evidence suggests that Q $\sim 10^2$ for monoliths and potentially smaller for rubble piles. With these values as well as our best-fit solution (Table 6) for 1994 CC, the eccentricity damping timescale for Gamma, if synchronously rotating, is $\tau_{\mathrm{e,damp}} \sim 10^{13}$ years. There is evidence that Gamma is, in fact, not synchronously rotating (Brozovic et al. 2010); however, even if Gamma is synchronous, we have shown that its eccentricity cannot damp on billion-year timescales because it is too small and distant.

Assuming identical composition and Q values for Alpha and Gamma, the ratio of the timescales of eccentricity damping and excitation for rubble piles are

$$\frac{\tau_{\mathrm{e,damp}}}{\tau_{\mathrm{e,excite}}} = \frac{19}{28} \tag{16}$$

which shows that tides will always damp the eccentricity for a synchronously rotating satellite regardless of the system's size and mass ratios (Goldreich & Sari 2009). The tidal despinning timescale, which is the time for a satellite to reach synchronous rotation with its central body, can be estimated for the satellites in both systems. For 2001 SN263, Gamma (inner) has a despinning timescale on the order of 10^5 years and Beta's (outer) timescale is on the order of 10^9 years. For 1994 CC, Beta (inner) has a timescale on the order of 10^7 years and Gamma's (outer) timescale is on the order of 10^{11} years. 2001 SN263 Gamma and 1994 CC Beta are therefore plausible synchronous rotators. If 1994 CC Beta was once closer to Alpha, its despinning timescale would be accordingly shorter.

The inclination damping timescale $\tau_{\mathrm{I,damp}}$ is related to the eccentricity damping timescale

(Yoder & Peale 1981):

$$\tau_{\rm I,damp} = \frac{7}{4}\tau_{\rm e,damp}\left(\frac{\sin I}{\sin\epsilon}\right)^2 \tag{17}$$

where I is the inclination of the orbit with respect to the central body's equator and ϵ is the obliquity of the satellite's spin axis relative to the orbit normal. To arrive at an estimate of this timescale, we assume $\epsilon \sim 1$ deg and find that $\tau_{\rm I,damp}$ is on the order of 10^{15} years for 1994 CC Gamma. These long eccentricity and inclination damping timescales indicate that tides cannot damp out e and I on timescales comparable to possible excitations of the system, which we now examine, nor the dynamical and collisional lifetimes of the system.

4.2. Kozai Resonance

Kozai resonance (Kozai 1962; Murray & Dermott 1999) is an angular momentum exchange process between a satellite's eccentricity and inclination that takes place under the influence of a massive outer perturber, provided that the relative inclination between the orbits of the satellite and the perturber exceeds a limiting value.

When considering the outer satellite as the perturber, we find that the Kozai process is not active, as the mutual inclinations do not exceed the required value. For instance, the limiting Kozai inclination corresponding to 2001 SN263's semi-major axis ratio ($a_{\rm inner}/a_{\rm outer} \sim 0.23$) can be estimated as ~37.5 degrees (Kozai 1962). The currently observed mutual inclination between the orbital planes of 2001 SN263 Beta and Gamma is only ~14 degrees.

We also consider the case with the Sun as the massive, outer perturber (as in Perets & Naoz 2009). The respective inclinations between the Sun's apparent orbit around Alpha and the orbits of the satellites are ~8 and ~17 degrees for 2001 SN263 Beta and Gamma and ~76 and ~61 degrees for 1994 CC Beta and Gamma. Consequently, while 2001 SN263 does not satisfy the limiting Kozai inclination (in this case estimated as ~39.2 degrees), 1994 CC can be prone to Kozai oscillations. From numerical integrations corresponding to our best-fit parameters for 1994 CC, we do not see either satellite in Kozai resonance with the Sun. In integrations where we have removed one satellite, such that there were only three bodies total (Alpha, Beta or Gamma, and the Sun), we saw that Gamma is particularly susceptible to Kozai resonance. We observed the telltale signs: strong coupled oscillations of eccentricity and inclination with the relevant period of ~56 years, conservation of the Delaunay quantity $H_k = \sqrt{(1-e^2)}\cos I$, and libration of the argument of pericenter. The differences between the two cases is that when the inner body is present, it causes the outer body's argument of pericenter to precess too fast for libration to occur. When both satellites are present, Kozai oscillations due to the Sun are suppressed. Therefore, Kozai interactions are not likely to explain the observed mutual inclinations and eccentricity.

4.3. Evection Resonance

Evection resonance can occur when the satellite's orbit around Alpha has a longitude of pericenter ϖ that precesses at the same rate as the Sun's apparent mean longitude λ_s with respect to Alpha. This results in libration of the argument $\phi = 2\lambda_s - 2\varpi$, and can produce a change in the eccentricity of the orbit (Touma & Wisdom 1998).

None of the satellites are currently in a configuration where the evection resonance can affect their evolution. However, as the semi-major axes change over time due to tidal or radiation effects, the precession rates evolve and Beta or Gamma can cross the evection resonance. However, as in the case of Kozai resonance, mutual perturbations will likely suppress the evection resonance or prevent it from being active for very long. Therefore, evection interactions are not likely to explain the observed mutual inclinations and eccentricity.

4.4. Passage Through Mean-Motion Resonances

Tidal evolution and binary YORP (BYORP; Cuk & Nesvorny 2010), which affects synchronous satellites, can change the orbits and lead to mean-motion resonances in the system. The outer bodies in both triple systems cannot be directly affected by BYORP as there is evidence that they are not in synchronous rotation (Nolan et al. 2008b; Brozovic et al. 2010). For the inner bodies where the synchronization condition is more likely to be met, it is possible that BYORP will cause migration of their orbits. This can result in an increase or decrease of the semi-major axis, depending on the satellite's shape. Previous work have shown that outward migration can cause an increase in the orbit's eccentricity (Cuk & Burns 2005), but inward migration can lead to a decrease in free eccentricity and is thought to be the most likely result of its evolution (Cuk & Nesvorny 2010). On the contrary, other studies (McMahon & Scheeres 2010a; McMahon & Scheeres 2010b) find that over long timescales, the eccentricity changes in the opposite direction of the semi-major axis. As for tidal evolution, this process will change the semi-major axis as $da/dt \propto a^{(-11/2)}$ (Murray & Dermott 1999), leading to converging orbits.

Whether due to tidal or BYORP evolution, a change in semi-major axes can lead to capture or passage through mean-motion resonances, which in turn can excite eccentricity and inclination (Dermott et al. 1988; Ward & Canup 2006). Such processes may therefore be responsible for the observed mutual inclinations and eccentricity.

4.5. Close Planetary Encounters

We tested the possibility that 1994 CC Gamma's nonzero eccentricity and both systems' mutual inclinations are due to close encounters with terrestrial planets. We performed systematic numerical simulations of the triple asteroid system and an Earth-sized body with over 5,000 permutations of orbital elements: inclinations with respect to Earth's equator, longitudes of the ascending node, and mean anomalies for both satellites. We started our simulations with equatorial, coplanar and circular orbits for Beta and Gamma, and integrated various close encounter distances up to 60 $R_\oplus$ with an encounter velocity v_∞ of 12 km/s (typical for Earth-crossing asteroids). We validated this procedure by comparing with results from Bottke & Melosh (1996) for a binary system.

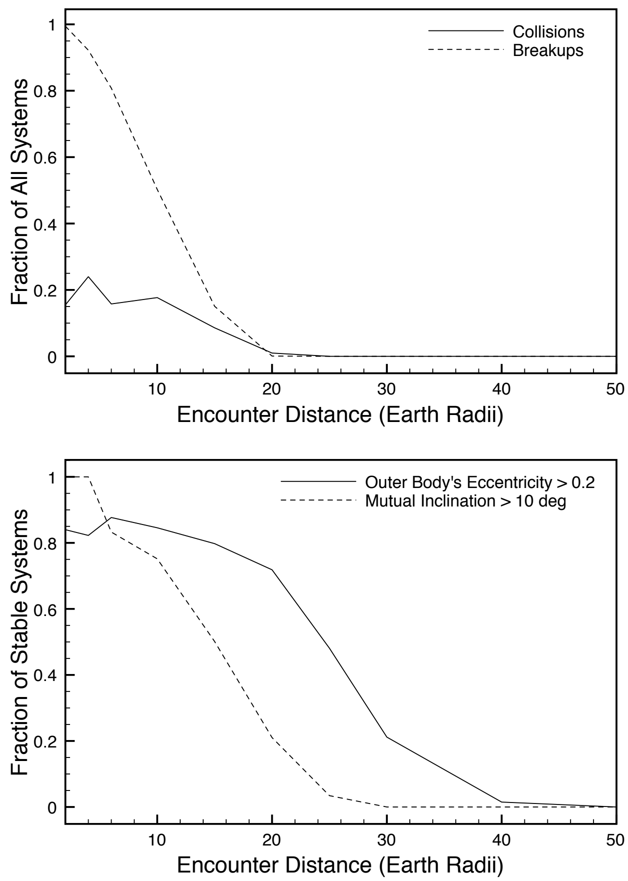

Fig. 9.— 2001 SN263: These figures show the close encounter statistics for the onset of instability (top) and excitation (bottom). The top diagram shows the fraction out of all systems; the bottom diagram shows the fraction out of only stable systems, defined as those with no collisions and ejections.

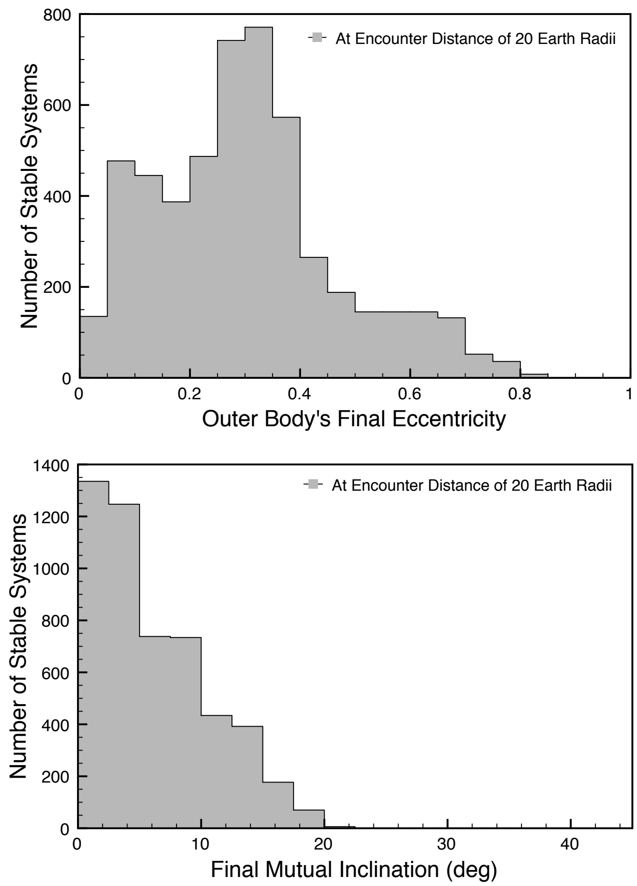

Fig. 10.— 2001 SN263: These histograms show the distribution of final eccentricities (top) and final mutual inclinations (bottom) for stable systems after close approaches of 20 $R_{\oplus}$.

Our close encounter results are shown in Figures 9-12, where we looked for (a) collisions between any of the bodies (Alpha, Beta, Gamma, and Earth-sized perturber) or (b) break-up of the system defined as ejection of either the inner or outer body, or both. For stable systems in which there were neither collisions nor break-ups, we examined cases where there were (c) excited eccentricities in the outer body of at least $\sim$0.2 seen in our orbit fitting for 1994 CC or (d) mutual inclinations greater than 10 degrees. The final eccentricities and inclinations were calculated from the mean of the osculating elements during the final few orbital periods.

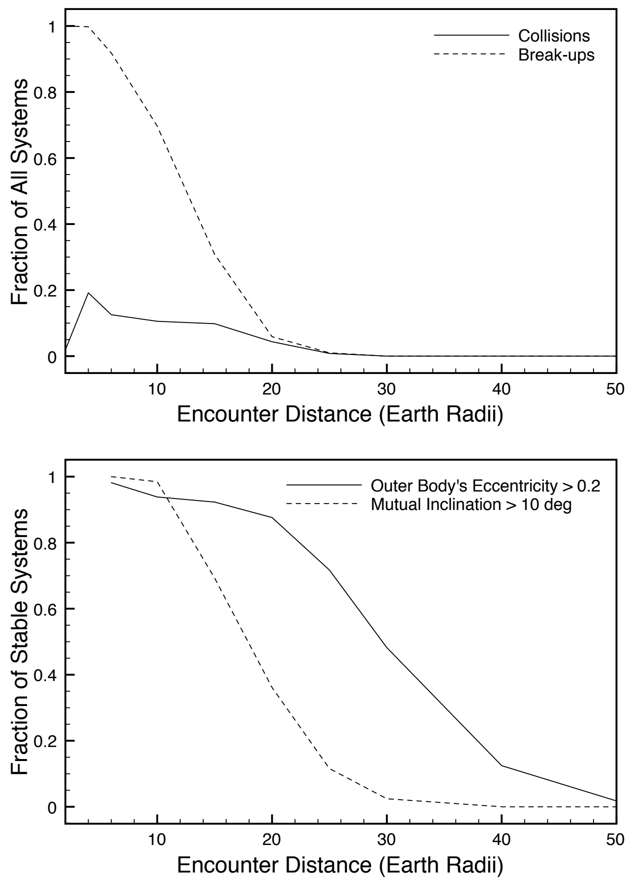

Fig. 11.— 1994 CC: These figures show the close encounter statistics for the onset of instability (top) and excitation (bottom). The top diagram shows the fraction out of all systems; the bottom diagram shows the fraction out of only stable systems, defined as those with no collisions and ejections. At encounter distances $\lesssim 5\ R_{\oplus}$, there are no stable systems left and as a result, we do not have excitation statistics for those very close encounters.

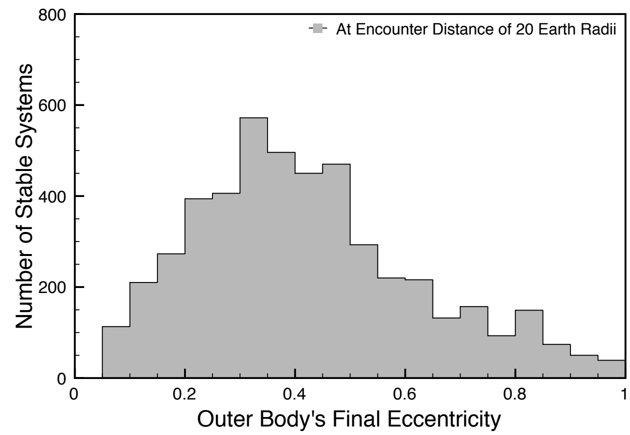

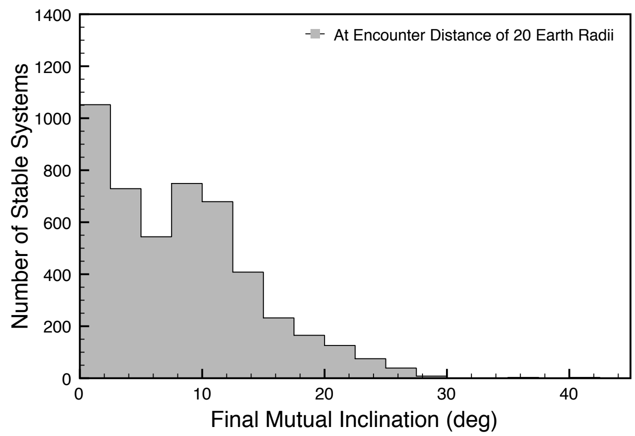

Fig. 12.— 1994 CC: These histograms show the distribution of final eccentricities (top) and final mutual inclinations (bottom) for stable systems after close approaches of 20 $R_\oplus$.

It is clear from Figures 9-12 that 1994 CC is more easily disrupted and excited than 2001 SN263, which agrees with our earlier calculation of $a_{\rm satellite}/r_{\rm Hill}$ in Section 2. During close approaches with Earth, the outer body was easily excited to eccentricities of at least 0.2 as far away as encounter distances of $\sim$40 $R_\oplus$ for 2001 SN263 and $\sim$50 $R_\oplus$ for 1994 CC. The orbital planes of the satellites gained mutual inclinations of at least 10 degrees starting at encounter distances of $\sim$25 $R_\oplus$ for 2001 SN263 and $\sim$30 $R_\oplus$ 1994 CC. Unbound systems due to break-up/ejection scenarios started occurring at $\sim$20 $R_\oplus$ encounter distances for 2001 SN263 and $\sim$25 $R_\oplus$ for 1994 CC. The distribution of the outer body's final eccentricity and final mutual inclination between satellite orbits at a close encounter distance of 20 $R_{\oplus}$ are shown for 2001 SN263 (Figure 10) and 1994 CC (Figure 12). We note that in Figures 9 and 11, at very close encounter distances (less than 5 $R_{\oplus}$) there are few stable systems left due to a high rate of ejections. As a result, for very close encounter distances the statistics shown for fraction of stable systems with excited eccentricities and mutual inclinations are more uncertain.

From these hyperbolic flyby simulations, we found that close planetary encounters could affect the orbits at distances as large as 50 $R_{\oplus}$. Such close approaches to Earth cannot at present happen, based on the current value of the minimum orbital intersection distance (MOID): $\sim$1190 $R_{\oplus}$ for 2001 SN263 and $\sim$380 $R_{\oplus}$ for 1994 CC (see Table 8). The MOID is the minimum separation between the osculating ellipses of the orbits of two bodies, without regard to position of the bodies in their orbits (Sitarski 1968); it remains valid as long as the osculating elements approximate the actual orbits. Over time, these elements will change, and it is likely that the observed high eccentricity and mutual inclinations were acquired during planetary encounters at a time when the MOID was lower and allowed for closer approaches.

Table 8: Minimum Orbital Intersection Distance (MOID)

	2001 SN263	1994 CC
Mercury MOID (AU)	0.695	0.508
Venus MOID (AU)	0.320	0.233
Earth MOID (AU)	0.0506	0.0162
Mars MOID (AU)	0.169	0.112

This table shows the current minimum orbital intersection distance (MOID) between the triple-asteroid systems and the terrestrial planets using orbital elements that are valid at MJD 54509.0 (2001 SN263) and MJD 54994.0 (1994 CC).

We can calculate a rough estimate for how often close planetary encounters occur for generic near-Earth systems (Chauvineau et al. 1995):

$$t \sim \frac{2\tau_{\rm coll} R_\oplus^2}{b^2} \tag{18}$$

where t represents the time between encounters up to an impact parameter b and $\tau_{\rm coll}$ is the asteroid's lifetime against impact with the terrestrial planets. For Earth, the average interval between impacts is $\sim 4 \times 10^6$ and $\sim 3 \times 10^5$ years for objects similar in size to 2001 SN263 and 1994 CC, respectively (Stuart & Binzel 2004). There are approximately $\sim$150 near-Earth asteroids with a size comparable to 2001 SN263 and $\sim$2000 for 1994 CC, and accordingly, we estimate $\tau_{\rm coll} \sim 6 \times 10^8$ years for both 2001 SN263 and 1994 CC.

In our simulations with planetary encounters, break-up of the asteroid triples occurred in 50% of our systems at impact parameters $b \sim 10R_\oplus$ for 2001 SN263 and $b \sim 13R_\oplus$ for 1994 CC. Thus, we calculate t to be $\sim$12 Myrs for 2001 SN263 and $\sim$7 Myrs for 1994 CC, which represent the estimated lifetimes of the systems due to such scattering encounters. These timescales are comparable to the $\sim$10 Myr dynamical lifetimes calculated by Gladman et al. (1997). A similar calculation for the time interval between planetary encounters that could excite 1994 CC Gamma's eccentricity using $b \sim 30R_\oplus$ (when 50% of our simulations showed excited eccentricities of at least 0.2) yields $\sim$1 Myrs. As a result, close planetary encounters that occur on million-year timescales can reproduce the observed eccentricity and inclinations. These generic timescales could be improved with encounter calculations for specific near-Earth asteroids, such as those performed by Nesvorny et al. (2010).

We note that while close planetary encounters can explain the excited eccentricity and mutual inclinations in near-Earth triple systems like 2001 SN263 and 1994 CC, different processes are required for main belt asteroids and those trans-neptunian objects that have not experienced strong planetary scattering events.

5. Conclusion

In this work, we found dynamical solutions for two triple systems, 2001 SN263 and 1994 CC, where we have derived the orbits, masses, and Alpha's J_2 gravitational harmonic using full N-body integrations. We used range and Doppler data from Arecibo and Goldstone to solve this non-linear least-squares problem with a dynamically interacting three-body model that provided an excellent match to our radar observations. Given the three-body nature of these systems, we also measured the precession rates of the apses and nodes, and compared them to our corresponding analytical expressions from J_2 and secular contributions. No resonant arguments were found to be librating in either triple system.

For both systems, we detected significant mutual inclinations (2001 SN263: $\sim$14 deg, 1994 CC: $\sim$16 deg) between the orbital planes of Beta and Gamma. We also found a nonzero orbital eccentricity ($\sim$0.2) for 1994 CC's outer body, Gamma. The eccentricity and inclination damping timescales are long, suggesting that both systems are in excited states. We investigated excitation mechanisms that could explain the observed orbital configurations, including Kozai and evection resonances, mean-motion resonance crossings, and close encounters with the terrestrial planets. Close encounters that occur on million-year timescales can reproduce the observed mutual inclinations in both systems and 1994 CC Gamma's eccentricity.

REFERENCES

Benecchi, S.D., Noll, K.S., Grundy, W.M., Levison, H.F. 2010, Icarus, 207, 978

Bottke, W.F., Jr. & Melosh, H.J. 1996, Icarus, 124, 372

Brown, M.E., van Dam, M.A., Bouchez, A.H., Le Mignant, D., Campbell, R.D., Chin, J.C.Y., Conrad, A., Hartman, S.K., Johansson, E.M., Lafon, R.E., Rabinowitz, D.L., Stomski, P.J., Jr., Summers, D.M., Trujillo, C.A., Wizinowich, P.L. 2006, ApJ, 639, L43

Brozovic, M., Benner, L.A.M., Nolan, M.C., Howell, E.S., Magri, C., Giorgini, J.D., Taylor, P.A., Margot, J.L., Busch, M.W., Shepard, M.K., Carter, L.M., Jao, J.S., van Brimmer, J., Franck, C.R., Silva, M.A., Kodis, M.A., Kelley, D.T., Slade, M.A., Bramson, A., Lawrence, K.J., Pollock, J.T., Pravec, P., Reichart, D.E., Ivarsen, K.M., Haislip, J., Nysewander, M.C., Lacluyze, A.P. 2009, IAU Circ., 9053

Brozovic, M., Benner, L.A.M., Nolan, M.C., Howell, E.S., Magri, C., Giorgini, J.D., Taylor, P.A., Margot, J.L., Busch, M.W., Shepard, M.K., Scheeres, D.J., Carter, L.M. 2010, AAS/Division for Planetary Sciences Meeting Abstracts, 42

Brozovic, M. et al., in preparation

Chambers, J.E. 1999, MNRAS, 304, 793

Chauvineau, B. & Farinella, P. 1995, Icarus, 115, 36

Cuk, M. & Burns, J. 2005, Icarus, 176, 418

Cuk, M. & Nesvorny, D. 2010, Icarus, 207, 732

Dermott, S.F., Malhotra, R., Murray, C.D. 1988, Icarus, 76, 295

Gladman, B.J., Migliorini, F., Morbidelli, A., Zappala, V., Michel, P., Cellino, A., Froeschle, C., Levison, H.F., Bailey, M., Duncan, M. 1997, Science, 277, 197

Goldreich, P. & Sari, R. 2009, ApJ, 691, 54

Hudson, S. 1993, Remote Sensing Reviews, 8, 195

Kozai, Y. 1962, AJ, 67, 591

Lee, M.H. & Peale, S.J. 2006, Icarus 184, 573

Magri, C., Ostro, S.J., Scheeres, D.J., Nolan, M.C., Giorgini, J.D., Benner, L.A.M., Margot, J. 2007, Icarus, 186, 152

Marchis, F., Descamps, P., Hestroffer, D., Berthier, J. 2005, Nature, 436, 565

Marchis, F., Baek, M., Descamps, P., Berthier, J., Hestroffer, D., Vachier, F. 2007, IAU Circular, 8817

Marchis, F., Descamps, P., Berthier, J., Emery, J.P., 2008a, IAU Circular, 8980

Marchis, F., Pollock, J., Pravec, P., Baek, M., Greene, J., Hutton, L., Descamps, P., Reichart, D.E., Ivarsen, K.M., Crain, J.A., Nysewander, M.C., Lacluyze, A.P., Haislip, J.B., Harvey, J.S. 2008b, IAU Circ., 8928

Marchis, F., Lainey, V., Descamps, P., Berthier, J., van Dam, M., de Pater, I., Macomber, B., Baek, M., Le Mignant, D., Hammel, H.B., Showalter, M., Vachier, F. 2010, ApJ, 210, 635

Margot, J.L., Nolan, M.C., Benner, L.A.M., Ostro, S.J., Jurgens, R.F., Giorgini, J.D., Slade, M.A., Campbell, D.B. 2002, Science, 296, 1445

Margot, J.L., Brown, M.E., Trujillo, C.A., Sari, R., Stansberry, J.A. 2005, DPS, 37, 737

Markwardt, C.B. 2008, ASPC, 411, 251M, arXiv:astro-ph/0902.2850v1

McMahon, J. & Scheeres, D. 2010a, CMDA, 106, 261

McMahon, J. & Scheeres, D. 2010b, Icarus, 209, 494

Merline, W.J., Weidenschilling, S.J., Durda, D.D., Margot, J.L., Pravec, P., Storrs, A.D. 2002, Asteroids III

Murray, C.D. & Dermott, S.F. 1999, Solar System Dynamics

Nesvorny, D., Bottke, W.F., Vokrouhlicky, D., Chapman, C.R., Rafkin, S. 2010, Icarus, 209, 510

Nolan, M.C., Howell, E.S., Benner, L.A.M., Ostro, S.J., Giorgini, J.D., Busch, M.W., Carter, L.M., Anderson, R.F., Magri, C., Campbell, D.B., Margot, J.L., Vervack, R.J., Jr., Shepard, M.K. 2008a, IAU Circ., 8921

Nolan, M.C., Howell, E.S., Becker, T.M., Magri, C., Giorgini, J.D., Margot, J.L. 2008b, AAS/Division for Planetary Sciences Meeting Abstracts, 40

Nolan, M.C. et al., in preparation

Noll, K.S., Grundy, W.M., Chiang, E.I., Margot, J.L., Kern, S.D. 2008, The Solar System Beyond Neptune, 354

Ostro, S.J., Margot, J., Benner, L.A.M., Giorgini, J.D., Scheeres, D.J., Fahnestock, E.G., Broschart, S.B., Bellerose, J., Nolan, M.C., Magri, C., Pravec, P., Scheirich, P., Rose, R., Jurgens, R.F., De Jong, E.M., Suzuki, S. 2006, Science, 314, 1276

Perets, H.B. & Naoz, M. 2009, ApJ, 699, L17

Pravec, P., and 56 other colleagues 2006, Icarus, 181, 63

Press, W.H., Flannery, B.P., Teukolsky, S.A., Vetterling, W.T. 1992, Numerical Recipes in C: The Art of Scientific Computing

Ragozzine, D. & Brown, M.E., 2009, AJ, 137, 4766

Scheeres, D.J., Fahnestock, E.G., Ostro, S.J., Margot, J.-L., Benner, L.A.M., Broschart, S.B., Bellerose, J., Giorgini, J.D., Nolan, M.C., Magri, C., Pravec, P., Scheirich, P., Rose, R., Jurgens, R.F., De Jong, E M., Suzuki, S. 2006, Science, 314, 1280

Shepard, M.K., Margot, J.-L., Magri, C., Nolan, M.C., Schlieder, J., Estes, B., Bus, S.J., Volquardsen, E.L., Rivkin, A.S., Benner, L.A.M., Giorgini, J.D., Ostro, S.J., Busch, M.W. 2006, Icarus, 184, 198

Sitarski, G. 1968, Acta Astronomica, 18, 2

Stuart, J.S. & Binzel, R.P. 2004, Icarus, 170, 295

Tholen, D.J., Buie, M.W., Grundy, W.M., Elliott, G.T. 2008, AJ 135, 777

Touma, J. & Wisdom, J. 1998, AJ, 115, 1653

Walsh, K.J., Richardson, D.C., & Michel, P. 2008, Nature, 454, 188

Ward, W.R. & Canup, R.M. 2006, Science, 313, 1107

Weaver, H.A., Stern, S.A., Mutchler, M.J., Steffl, A.J., Buie, M.W., Merline, W.J., Spencer, J.R., Young, E.F., Young, L.A. 2006, Nature, 439, 943

Winter, O.C., Boldrin, L.A.G., Vieira Neto, E., Vieira Martins, R., Giuliatti Winter, S.M., Gomes, R.S., Marchis, F., Descamps, P. 2009, MNRAS, 395, 218

Yoder, C. & Peale, Stanton 1981, Icarus, 47, 1

Chapter 2

Orbits, Masses, and Evolution of Main Belt Triple (87) Sylvia

Reproduced by permission of the AAS (Fang, J., Margot, J.L., Rojo, P., 2012, The Astronomical Journal, 144, 70).

1. Introduction

(87) Sylvia is a triple asteroid residing in the main belt, with heliocentric semi-major axis 3.5 AU, eccentricity 0.085, and inclination 11° relative to the ecliptic. Sylvia's outer satellite, named Romulus, was discovered in 2001 using the W. M. Keck Telescope (Brown & Margot 2001; Margot & Brown 2001), and was also detected in Hubble Space Telescope (HST) images (Storrs et al. 2001). The inner satellite, Remus, was not discovered until the advent of improved adaptive optics systems in 2004 using the European Southern Observatory's Very Large Telescope (VLT) (Marchis et al. 2005). The diameter of the primary has been estimated at ∼280 km through shape fits to adaptive optics images (Marchis et al. 2005); this estimate is consistent with stellar occultation observations (Lin et al. 2009). Assuming this primary size, approximate sizes for the individual satellites have been estimated by adopting the same albedo as the primary and measuring each satellite's brightness relative to the primary. The diameter estimates are ∼7 km for Remus and ∼18 km for Romulus (Marchis et al. 2005).

Sylvia was the first triple asteroid system announced, even though the triple nature of 2002 CE26 was being actively discussed during the acquisition of the Sylvia observations (Shepard et al. 2006). Additional discoveries of multiples in the Solar System have followed. They include near-Earth triples (153591) 2001 SN263 (Nolan et al. 2008) and (136617) 1994 CC (Brozovic et al. 2009), main belt triples Kleopatra (Descamps et al. 2011), Eugenia (Merline et al. 1999; Marchis et al. 2007), Balam (Merline et al. 2002; Marchis et al. 2008), and Minerva (Marchis et al. 2011), and trans-Neptunian systems (47171) 1999 TC36

(Margot et al. 2005; Benecchi et al. 2010), Haumea (Brown et al. 2005, 2006), and the Pluto/Charon system (Weaver et al. 2006).

Following these discoveries, characterization of multiple systems have unearthed a wealth of information about their fundamental physical properties such as masses and densities, dynamical processes, and constraints on formation and evolutionary mechanisms. Such research has been possible because we can derive the masses of the individual components of a triple or higher-multiplicity system by analyzing their mutual gravitational interactions, which is possible in binary systems only when reflex motion is detected (Margot et al. 2002; Ostro et al. 2006; Naidu et al. 2011). These masses in conjunction with size estimates can provide densities. Using this method, Fang et al. (2011) performed a detailed analysis of 2001 SN263 and 1994 CC, including masses, densities, and dynamical evolution. Similarly, work on the Pluto/Charon system and dwarf planet Haumea and its satellites have yielded information about their physical properties, tidal interactions, and evolutionary processes (Lee & Peale 2006; Tholen et al. 2008; Ragozzine & Brown 2009). The high scientific return from studies of binaries and triples has been reviewed by Merline et al. (2002) and Noll et al. (2008).

To date, no such dynamical orbit solution nor detailed analysis has been performed for Sylvia. Previous work by Marchis et al. (2005) approximated the actual orbits of Remus and Romulus with individual two-body fits that included primary oblateness. However, drawbacks of such methods include the failure to account for third-body perturbations as well as the inability to solve for individual component masses. Additional researchers based their studies on the published two-body orbits (Marchis et al. 2005) plus unspecified component mass assumptions to study Sylvia's long-term evolution (Winter et al. 2009; Frouard & Compere 2012), even though component masses are undetermined and can span several orders of magnitude.

In this work, we report additional Keck and VLT imaging data for Sylvia (Section 2). Using primary−satellite separations measured from these data plus published astrometry, we present a fully dynamical 3-body orbital and mass solution for Sylvia, by accounting for mutually interacting orbits as well as the primary's non-sphericity (Section 3). Although the orbital periods of the satellites are near a 8:3 ratio, we do not find that the system is currently in such a resonance (Section 4). We also analyze Sylvia's short-term and long-term future evolution (Section 5). Lastly, we investigate the past orbital evolution of Remus and Romulus by modeling passage through the 3:1 mean-motion resonance (Section 6). A summary of main conclusions is given in Section 7.

2. Observations

We report new observations of Sylvia in 2011 from both Keck and VLT, as well as summarize existing observations taken in 2001−2004 using Keck, HST, and VLT. Astrometry derived from these datasets are used for orbit fits described in the next section (Section 3).

2.1. New Data in 2011

Our observations in 2011 are summarized in Table 1. In total, we obtained 7 partial nights of service (or "queue") mode observing at VLT and 4 partial nights of visitor mode at Keck. At the VLT, we used the NACO (NAOS-CONICA) high-resolution IR imaging camera (Rousset et al. 2003; Lenzen et al. 2003) in its S13 mode using the H filter, with a plate scale value reported as 0.013221 arcseconds per pixel[1]. We used four offset positions in a box pattern, with an integration time of 120 seconds per offset position. These four offset positions sampled the four quadrants of the CCD to calibrate and mitigate against detector defects. At Keck, we used NIRC2 (Near Infrared Camera 2) imaging in the H filter, with a plate scale of 0.009942 arcseconds per pixel[2]. Our Keck observations used four offset

[1]http://www.eso.org/sci/facilities/paranal/instruments/naco/doc

[2]http://www2.keck.hawaii.edu/inst/nirc2/genspecs.html

positions in a similar box pattern as with the VLT exposures, with an exposure time of 60 seconds per offset position. All observations using both VLT and Keck were performed with natural guide star adaptive optics, using Sylvia as the guide star (its apparent magnitude varied from V$\sim$11.7 to V$\sim$12.7 throughout the period of our 2011 observations).

We performed basic data reduction analysis for VLT and Keck images. Each frame (at each dither position) is flat-fielded and its bad pixels are corrected using a bad pixel mask obtained from outlier pixels present in all frames. Sky subtraction is performed by subtracting frames in pairs, where each frame is subtracted by another frame where the target has been offset. We performed subpixel 2-D Gaussian fitting to obtain precise centroids of the target in each sky-subtracted frame, and these centroids were used to align and combine all frames into one composite image. See Figure 1 for an example of a composite image obtained using Keck.

At each observation epoch, we detected either one or both satellites (see Table 1). As the satellites orbit the primary, they are occasionally obscured by the bright primary and this occurs most often for the inner satellite Remus. In cases where only one satellite is detected, we determined the identification of the satellite through orbit fitting. An incorrect identification of a satellite is easily shown as an obvious outlier in orbit fits. In all cases examined here, when only one satellite is detected, it is the outer satellite Romulus.

For all satellite detections, we measure the astrometric positions of the satellite relative to the primary by taking the difference between the centroids of the primary and the satellite. Specifically, we measure the position angle (degrees East of North) and separation of the satellite relative to the primary. These measurements are performed on the reduced composite image obtained at each observation epoch. These measurements are provided in Table 2.

Table 1: Summary of 2011 Observations

UT Date	MJD	Filter	Telescope	Detections
2011 Oct 7	55841.1097	H	VLT	Remus, Romulus
2011 Nov 6	55871.0856	H	VLT	Romulus
2011 Nov 8	55873.1289	H	VLT	Remus, Romulus
2011 Nov 10	55875.0451	H	VLT	Remus, Romulus
2011 Nov 15	55880.0256	H	VLT	Romulus
2011 Nov 16	55881.0466	H	VLT	Remus, Romulus
2011 Nov 20	55885.0460	H	VLT	Romulus
2011 Dec 15	55910.2129	H	Keck	Remus, Romulus
2011 Dec 15	55910.2288	H	Keck	Remus, Romulus
2011 Dec 15	55910.2698	H	Keck	Remus, Romulus
2011 Dec 16	55911.1877	H	Keck	Romulus
2011 Dec 16	55911.2510	H	Keck	Romulus
2011 Dec 17	55912.2615	H	Keck	Remus, Romulus
2011 Dec 18	55913.1972	H	Keck	Romulus
2011 Dec 18	55913.2035	H	Keck	Romulus

Summary of our 2011 adaptive optics observations at VLT and Keck. Epochs are provided in Universal Time (UT) dates as well as the Modified Julian Date (MJD). Remus is the inner satellite and Romulus is the outer satellite.

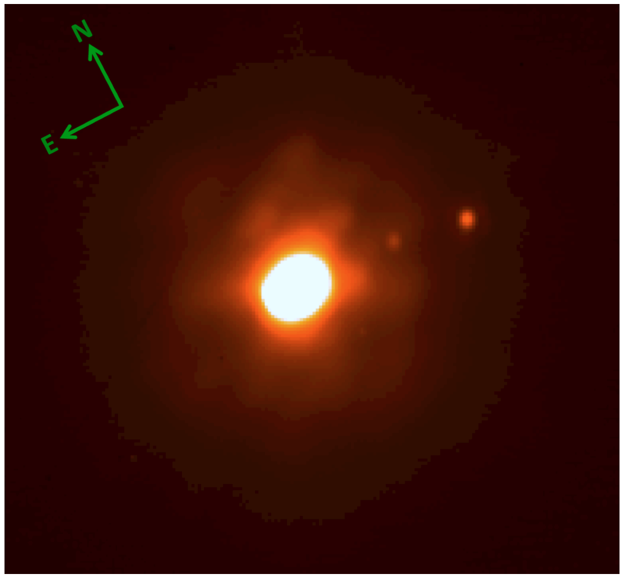

Fig. 1.— Keck H-band adaptive optics image on 2011 December 15 (corresponding modified Julian Date 55910.2129) of Sylvia with inner satellite Remus and outer satellite Romulus. In this image, the primary−Remus separation is about 0.34 arcseconds, and the primary−Romulus separation is about 0.57 arcseconds.

Table 2: Astrometry From 2011 Data

Satellite	MJD	PA (deg)	Sep. (arcsec)	x (arcsec)	y (arcsec)	σ (arcsec)
Remus	55841.1097	265.07	0.392	0.391	-0.034	0.0132
Remus	55873.1289	75.25	0.226	-0.218	0.057	0.0132
Remus	55875.0451	270.33	0.342	0.342	0.002	0.0132
Remus	55881.0466	87.23	0.381	-0.381	0.018	0.0132
Remus	55910.2129	268.16	0.341	0.341	-0.011	0.0099
Remus	55910.2288	267.49	0.343	0.342	-0.015	0.0099

Remus	55910.2698	267.80	0.325	0.325	-0.012	0.0099
Remus	55912.2615	84.22	0.349	-0.348	0.035	0.0099
Romulus	55841.1097	264.09	0.702	0.698	-0.072	0.0132
Romulus	55871.0856	92.92	0.369	-0.368	-0.019	0.0132
Romulus	55873.1289	271.41	0.606	0.606	0.015	0.0132
Romulus	55875.0451	88.92	0.643	-0.643	0.012	0.0132
Romulus	55880.0256	284.49	0.183	0.177	0.046	0.0132
Romulus	55881.0466	266.17	0.671	0.670	-0.045	0.0132
Romulus	55885.0460	264.34	0.357	0.355	-0.035	0.0132
Romulus	55910.2129	264.30	0.571	0.568	-0.057	0.0099
Romulus	55910.2288	263.66	0.572	0.568	-0.063	0.0099
Romulus	55910.2698	265.11	0.541	0.539	-0.046	0.0099
Romulus	55911.1877	95.41	0.392	-0.391	-0.037	0.0099
Romulus	55911.2510	92.09	0.446	-0.446	-0.016	0.0099
Romulus	55912.2615	78.76	0.423	-0.415	0.082	0.0099
Romulus	55913.1972	272.80	0.528	0.528	0.026	0.0099
Romulus	55913.2035	272.09	0.521	0.521	0.019	0.0099

Astrometry measured from 2011 data for Remus (inner) and Romulus (outer) at specific MJD epochs. We measured the position angle (PA; degrees East of North) and the separation of each satellite relative to the primary. These values are converted to positions x and y, where positive x direction is towards the West, and positive y direction is towards the North. We assign the instrument plate scale as the positional uncertainty σ for x and y.

2.2. Existing Data From 2001−2004

Publicly-available astrometry datasets for Sylvia include Keck data in 2001 (Margot & Brown 2001), HST data in 2001 (Storrs et al. 2001), and VLT data in 2004 (Marchis et al. 2005). For the 2004 VLT data, the paper by Marchis et al. (2005) contains their astrometric measurements of the satellites relative to the primary expressed as $x-y$ pairs, where they define x and y as positive in the East and North directions, respectively. However, they failed to indicate the signs (positive or negative) for their x and y measurements of Remus. In addition, at one epoch (MJD 53253.1738) their published astrometry give Remus an implausibly large separation from the primary. To fix these inaccuracies, we fit orbits to the astrometric points and have determined the correct signs for their measurements (note that we define x to be positive in the West direction). At epoch MJD 53253.1738, it appears that they have confused Remus and Romulus, and so we have swapped measurements for these two bodies at that epoch. These corrections, along with astrometry for the Keck and HST data in 2001, are given in Table 3.

In total, our baseline of observations spans a decade from 2001 to 2011. For Remus, which is never visible in data obtained prior to 2004, our 2011 observations add an additional 8 epochs to the existing 12 epochs for a total of 20 epochs of astrometry, extending the baseline of observations from about 1 month to 7 years. For Romulus, our 2011 observations add an additional 15 epochs to the existing 30 epochs for a total of 45 epochs of astrometric measurements, extending the baseline of observations from 3 years to 10 years. All of these astrometry positions, given in Tables 2 and 3, are used for dynamical three-body orbit fits described in the next section.

Table 3: Existing Astrometry From 2001−2004 Data

Satellite	MJD	PA (deg)	Sep. (arcsec)	x (arcsec)	y (arcsec)	σ (arcsec)	Reference
Remus	53227.3042	...	...	-0.411	0.002	0.0132	3
Remus	53249.2470	...	...	-0.239	-0.101	0.0132	3
Remus	53249.2532	...	...	-0.228	-0.101	0.0132	3
Remus	53251.2985	...	...	0.246	0.107	0.0132	3
Remus	53252.3627	...	...	0.421	0.000	0.0132	3
Remus	53253.1738	...	...	-0.445	-0.025	0.0132	3
Remus	53255.1091	...	...	0.435	0.002	0.0132	3
Remus	53256.2886	...	...	0.268	-0.072	0.0132	3
Remus	53261.1432	...	...	-0.394	0.033	0.0132	3
Remus	53261.2298	...	...	-0.430	-0.008	0.0132	3
Remus	53263.2146	...	...	0.412	0.004	0.0132	3
Remus	53263.2202	...	...	0.416	0.001	0.0132	3
Romulus	51958.4810	97.00	0.564	-0.559	-0.069	0.0168	1
Romulus	51959.3660	60.30	0.425	-0.369	0.211	0.0168	1
Romulus	51959.4200	54.10	0.383	-0.310	0.225	0.0168	1
Romulus	51960.4010	271.90	0.615	0.614	0.020	0.0168	1
Romulus	51962.4070	88.30	0.696	-0.696	0.021	0.0168	1

Romulus	51963.5700	306.00	0.330	0.267	0.194	0.0250	2
Romulus	53227.3042	...	...	-0.377	0.144	0.0132	3
Romulus	53246.3105	...	...	-0.785	-0.097	0.0132	3
Romulus	53246.3659	...	...	-0.755	-0.117	0.0132	3
Romulus	53249.2470	...	...	-0.547	0.139	0.0132	3
Romulus	53249.2532	...	...	-0.555	0.136	0.0132	3
Romulus	53249.3516	...	...	-0.654	0.109	0.0132	3
Romulus	53251.2985	...	...	0.763	-0.058	0.0132	3
Romulus	53252.3627	...	...	0.156	0.214	0.0132	3
Romulus	53253.1738	...	...	-0.791	0.049	0.0132	3
Romulus	53253.3445	...	...	-0.834	-0.018	0.0132	3
Romulus	53254.1603	...	...	-0.172	-0.214	0.0132	3
Romulus	53255.1091	...	...	0.835	0.003	0.0132	3
Romulus	53255.3928	...	...	0.793	0.105	0.0132	3
Romulus	53256.2886	...	...	-0.272	0.202	0.0132	3
Romulus	53259.2030	...	...	0.683	0.165	0.0132	3
Romulus	53261.1432	...	...	-0.546	-0.186	0.0132	3
Romulus	53261.2298	...	...	-0.449	-0.205	0.0132	3
Romulus	53262.1602	...	...	0.724	-0.073	0.0132	3
Romulus	53262.2759	...	...	0.786	-0.035	0.0132	3

Romulus	53262.2815	...	...	0.791	-0.032	0.0132	3
Romulus	53263.2146	...	...	0.221	0.230	0.0132	3
Romulus	53263.2202	...	...	0.215	0.231	0.0132	3
Romulus	53297.0193	...	...	-0.752	-0.038	0.0132	3
Romulus	53298.0064	...	...	0.101	-0.186	0.0132	3

Existing astrometry measured from 2001−2004 data for Remus (inner) and Romulus (outer) at specific MJD epochs, taken from [1] Margot & Brown (2001), [2] Storrs et al. (2001), and [3] Marchis et al. (2005) (the latter with corrections; see text). An ellipsis (...) means that the value was not reported. Measurements include the position angle (PA; degrees Earth of North) and the separation of each satellite relative to the primary. These values can be converted to positions x and y, where positive x direction is towards the West, and positive y direction is towards the North. As in Table 2, we assign the instrument plate scale as the positional uncertainty σ for x and y.

3. Orbital and Mass Solution

We fit a fully dynamical 3-body model to the astrometric measurements described in the previous section, taking into account mutually interacting orbits. Our model simultaneously fits for 16 parameters, including a set of 6 orbital parameters per satellite (semi-major axis, eccentricity, inclination, argument of pericenter, longitude of the ascending node, and mean anomaly at epoch), 3 masses for the three bodies, and the parameter J_2 representing the oblateness of the primary. The semi-major axis and eccentricity describe the size and shape of the orbit, both the inclination and longitude of the ascending node describe the orientation of the orbit, the argument of pericenter describes the location of pericenter (minimum radial distance of the orbit), and the mean anomaly at epoch can be used to determine the location of the satellite in its orbit at a particular time.

We describe these fitted parameters in more detail. The orbital elements of each satellite are relative to the primary body, and are defined with respect to the Earth equatorial reference frame of epoch J2000. Given that these orbital elements change over time due to perturbations in the three-body system, these are defined as *osculating* orbital elements. They are valid at a specific epoch, MJD 53227.0, corresponding to UT date 2004 August 10 00:00. The fitted masses are derived assuming $G = 6.67 \times 10^{-11}$ m^3 kg^{-1} s^{-2} for the gravitational constant. The primary's non-spherical nature, which can introduce additional non-Keplerian effects, is represented by an oblateness coefficient J_2. The distribution of mass within the primary can be represented by terms in a spherical harmonic expansion of its gravitational potential, and the quadrupole term J_2 is the lowest-order gravitational moment. J_2 is related to the primary's three principal moments of inertia ($C \geq B \geq A$) as

$$J_2 = \frac{C - \frac{1}{2}(A + B)}{MR^2}, \tag{1}$$

where the denominator is a normalization factor including the primary's mass M and equatorial radius R (i.e., Murray & Dermott 1999). In all of our fits, the radius R is assumed to be 140 km. The inclusion of J_2 in our fits also requires a primary spin pole direction to be specified, and typically we fix the primary pole to the orbit pole of the most massive satellite.

With a total of 16 parameters and 130 data measurements (Tables 2 and 3), we have 114 degrees of freedom (number of data points minus the number of parameters). We adopt a least-squares approach to this problem by minimizing the chi-square χ^2 statistic, where $\chi^2 = \sum_i (O_i - C_i)^2/\sigma_i^2$ for a set of $N (1 \leq i \leq N)$ observations with σ_i uncertainties and observed O_i and computed C_i values. We utilize a Levenberg-Marquardt non-linear least-squares algorithm written in IDL called `mpfit` (Markwardt 2009). With 16 parameters, this is a very computationally intensive problem, given the large amount of parameter space to explore as well as the computationally expensive 3-body orbital integrations that need to be performed. Especially for least-squares problems with a large number of parameters, it is impossible to guarantee that a global χ^2 minimum has been found. More often than not, the minimization procedure converged on a local minimum and therefore it was necessary to re-fit with different starting conditions. In total, we started the fitting procedure with tens of thousands of sets of starting conditions, and we performed up to 20 iterations (equaling hundreds of χ^2 evaluations) for each set of starting conditions.

These starting conditions included plausible ranges of parameter space for fitted parameters. We explored all possible values of eccentricity (0−1), orbital angles (0−360°), semi-major axes (500−900 km for Remus and 1100−1500 km for Romulus), and J_2 values (0−0.2). Starting values ranged from on the order of 10^{18} to 10^{20} kg for the primary's mass and from on the order of 10^{13} to 10^{17} kg for each satellite's mass. Ranges for satellite masses covered all possible mass values by sampling various size (Remus: ∼5−9 km in diameter, Romulus: ∼14−22 km in diameter; Marchis et al. 2005) and density (0.1−10 g cm^{-3}) ranges.

In addition, we also explored various primary spin axis orientations for the primary. This was possible with this data set because the perturbations due to the oblateness of the primary are detectable, and because those perturbations depend on the spin axis orientation. These effects are captured by three fitted parameters: two for the primary spin axis orientation, and one for the value of J_2. We systematically explored the entire celestial sphere for the primary spin axis orientation, but we also tested specific poles that had been favored by previous studies. These specific spin axis orientations include RA=355° and DEC=82° (close to satellite orbital poles) suggested from light curve analysis (Kaasalainen et al. 2002), RA=68° and DEC=78° from a compilation of previous data (Kryszczyńska et al. 2007), and RA=100° and DEC=62° derived using adaptive optics imaging data (Drummond & Christou 2008). From these fits, we find that primary spin poles misaligned with satellite orbit poles do not provide good solutions (such as poles by Kryszczyńska et al. (2007) and Drummond & Christou (2008)). Instead, we determined that the best-fit spin axis direction was nearly aligned with the satellites' orbital poles, which are almost coplanar. As a result, for nearly all fits, we aligned the primary's spin pole to the orbital pole of the most massive satellite. The fact that both satellites orbit in or near the equator of the primary provides an important constraint on satellite formation mechanisms.

For each set of starting conditions, our orbit-fitting method proceeded as follows. First, we performed N-body numerical integrations using the `Mercury` integration package (Chambers 1999), which takes into account mutually interacting orbits as well as the effects due to primary oblateness. We used a Bulirsch-Stoer algorithm for our integration method, which is computationally slow but accurate, and we chose an initial time step that samples finer than 1/25th of the innermost orbital period. These 3-body integrations need to cover all epochs of observation, which span about a decade (2001−2011). From these integrations, we determined the positions and velocities of each satellite relative to the primary at all epochs of observation (corrected for light travel time) by interpolation. The length and resolution of these integrations were the limiting factors in the computational speed of each minimization. Second, we obtained the vector orientation of Sylvia's position relative to an observer on Earth for all epochs of observation (again, corrected for light time), taking into account aspect variations due to geocentric distance variations and Sylvia's motion across the sky. Third, we used these orientations to project and compute primary−satellite separations on the plane of the sky at each observation epoch. These computed separations were compared with our observed separations (Tables 2 and 3) to determine the χ^2 goodness-of-fit statistic. These methods benefit from the heritage of over a decade of work on orbit fitting as well as our work on fitting 3-body models to datasets of triples, including near-Earth asteroids (Fang et al. 2011).

Table 4 shows the best-fit orbit solution. The chi-square is 73.55, and with 114 degrees of freedom, this corresponds to a reduced chi-square of 0.6452. This indicates that the fit is very good, and that uncertainties were likely slightly overestimated. This best-fit solution is also visually illustrated in an orbit diagram in Figure 2, where the orbits are projected onto the primary's equatorial plane. Residuals of the best-fit solution are shown in Figure 3 for Remus and Figure 4 for Romulus, where each figure's panel shows the residuals for a particular year of observation (2001, 2004, or 2011). The residual is defined as $\chi_i = (O_i - C_i)/\sigma_i$ for observation epoch i.

There are two types of 1σ uncertainties given in Table 4: formal and adopted. The *formal* 1σ uncertainties are obtained using the covariance matrix resulting from the least-squares fitting procedure. These formal 1σ uncertainties may not always be accurate representations of the actual uncertainties. Accordingly, the *adopted* 1σ uncertainties are obtained through a more rigorous method by determining each parameter's 1σ confidence levels (e.g., Cash 1976; Press et al. 1992). To determine each parameter's uncertainties, we hold the parameter fixed at a range of plausible values while simultaneously fitting for all other parameters. Since one parameter is held fixed at a time, a 1σ confidence region is prescribed by the range of solutions that yield chi-square values within 1.0 of the lowest chi-square. This is a computationally intensive process, and we performed this method to determine uncertainties for the primary's pole (R.A. and Dec.) as well as for each fitted parameter with the exception of the arguments of pericenter and mean anomalies at epoch. We consider the adopted uncertainties to be more accurate representations of the actual uncertainties than the formal uncertainties. We note that these adopted uncertainties do not preclude any systematic errors that may have occurred, such as during the measurement of astrometry from the images.

Most solve-for parameters are well constrained by the data, with formal uncertainties of 10% or less, and as low as $\sim$1% for the mass and oblateness of the primary. One notable exception is the mass of Romulus. The formal uncertainty on this parameter amounts to $\sim$60% of the nominal value, indicating that it is not well constrained by the data. As for orbit pole orientations, they are determined to $\sim$1.5 degrees uncertainty (1σ) for Remus and $\sim$1 degree for Romulus, and the primary spin axis orientation is determined to $\sim$1 degree. Given the near-circular nature of the orbits, the arguments of pericenter ω and hence mean anomalies at epoch M are not well-defined (but the satellite positions, or $\omega + M$, are in fact well-defined).

Table 4: Best-fit Parameters and 1σ Uncertainties

Parameter	**Best-fit**	**Formal 1σ**	**Adopted 1σ**
	Remus (inner):		
Mass (10^{14} kg)	7.333	± 0.717	$^{+4.7}_{-2.3}$
a (km)	706.5	± 0.007	$^{+2.5}_{-2.5}$
e	0.02721	± 0.010	$^{+0.013}_{-0.012}$
i (deg)	7.824	± 0.667	$^{+0.68}_{-0.82}$
ω (deg)	357.0	± 15.14	...
Ω (deg)	94.80	± 5.000	$^{+5.2}_{-5.8}$
M (deg)	261.0	± 13.43	...
P (days)	1.373	...	$^{+0.010}_{-0.010}$
	Romulus (outer):		
Mass (10^{14} kg)	9.319	± 5.406	$^{+20.7}_{-8.3}$
a (km)	1357	± 0.059	$^{+4.0}_{-4.0}$
e	0.005566	± 0.004	$^{+0.005}_{-0.004}$
i (deg)	8.293	± 0.210	$^{+0.21}_{-0.29}$
ω (deg)	61.06	± 18.74	...
Ω (deg)	92.60	± 1.339	$^{+2.9}_{-1.6}$
M (deg)	197.0	± 18.75	...

P (days)	3.654	...	$^{+0.025}_{-0.024}$
Primary:			
Mass (10^{19} kg)	1.484	±0.00017	$^{+0.016}_{-0.014}$
J_2	0.09959	±0.00084	$^{+0.0004}_{-0.0010}$
R.A. (deg)	2.597	±1.339	$^{+3.4}_{-1.6}$
Dec. (deg)	81.71	±0.210	$^{+0.29}_{-0.71}$

Best-fit parameters including individual masses, orbital parameters (semi-major axis a, eccentricity e, inclination i, argument of pericenter ω, longitude of the ascending node Ω, mean anomaly at epoch M), primary oblateness J_2, and primary spin pole (R.A. and Dec.). These orbital elements are valid at epoch MJD 53227 in the equatorial frame of J2000. We derived an effective orbital period P from the best-fit values of semi-major axis and mass of the considered satellite plus all interior masses. Two types of uncertainties are listed: formal 1σ statistical errors are derived from the least-squares covariance matrix, and adopted 1σ errors are obtained for select parameters through a more rigorous method (see text). For parameters ω and M with no adopted 1σ errors, we recommend using the formal 1σ errors.

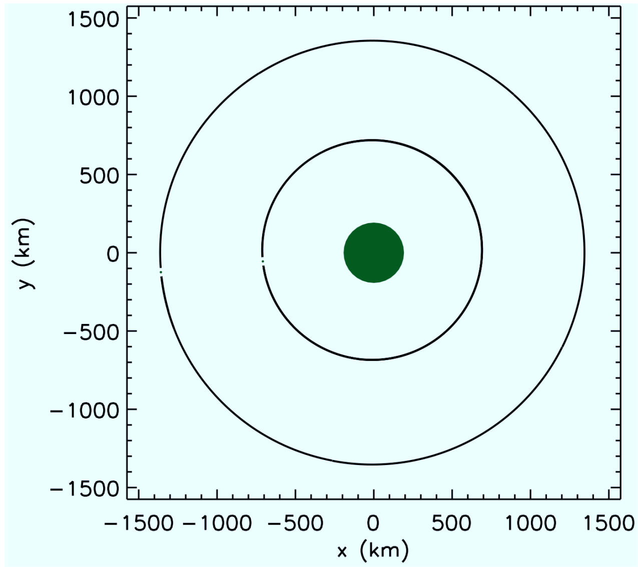

Fig. 2.— Diagram of best-fit orbits for satellites Remus (inner) and Romulus (outer), projected onto the primary's equatorial plane. These orbits show the actual trajectories from numerical integrations. The relative sizes of the bodies are shown to scale using green circles, assuming these diameters: 10.6 km for Remus, 10.8 km for Romulus, and 280 km for the primary. All bodies are located at their positions at MJD 53227 with the primary centered on the origin.

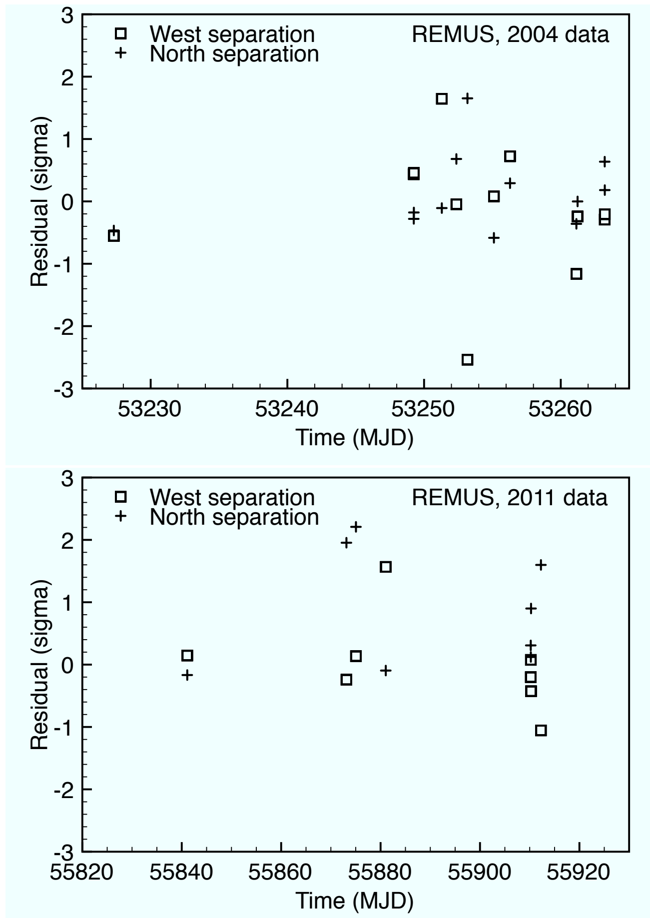

Fig. 3.— Residuals for separations in the West and North directions corresponding to the best-fit orbit (Table 4) for inner satellite Remus. The two panels represent distinct epochs of observations (2004, 2011).

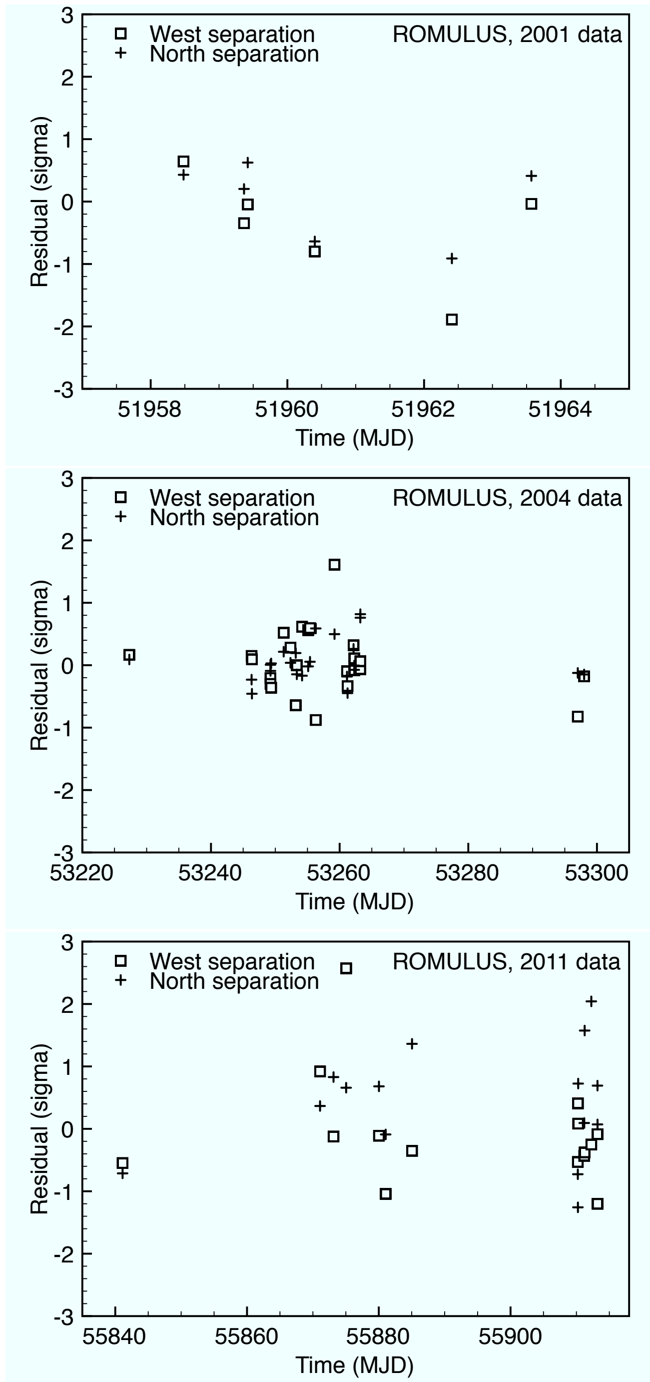

Fig. 4.— Residuals for separations in the West and North directions corresponding to the best-fit orbit (Table 4) for outer satellite Romulus. The three panels represent distinct epochs of observations (2001, 2004, 2011).

The best-fit orbital solution indicates that the satellites follow relatively circular orbits at semi-major axes of about 5 and nearly 10 primary radii. The mutual inclination (relative inclination) between the orbital planes of the satellites is $0.56°^{+1.5}_{-0.5}$. The low mutual inclination indicates that the orbital planes are nearly coplanar. This alignment supports a satellite formation mechanism in which the satellites would tend to remain close to the equatorial plane of the primary (e.g., a sub-catastrophic collision). The alignment is likely indicative of formation conditions rather than evolution, as tidal damping of inclinations can be a lengthy process. Assuming various models (monolithic or rubble pile) for tidal dissipation, inner satellite Remus could take on the order of 10^8 years up to the age of the Solar System to damp from 2 degrees to 1 degree.

Information about size, shape, and density can be derived from our best-fit orbital solution. We obtain a density of $1.29{\pm}0.39$ g cm^{-3} for the primary by assuming a diameter of 280 km (lacking realistic error bars on the size of the primary, we assumed volume uncertainties of 30%). The density error is dominated by the volume error since the mass of the primary is known to ∼1%. The primary is also oblate, with a well-constrained J_2 value of about 0.09959 which corresponds to an axial ratio $c/a = 0.7086$ if we assume equatorial symmetry and uniform density. Size estimates for Remus and Romulus can be obtained by assuming that they have a bulk density equal to that of the primary, and by considering the adopted 1σ confidence interval of satellite masses. We find radii of ∼4.5−6.1 km for Remus and ∼2.6−8.2 km for Romulus. These ranges would have to be modified if the density of the primary or of the satellites was different from the nominal value assumed here, but only slightly as the dependence is $\rho^{-1/3}$.

We compare our best-fit solution in Table 4 to the solution previously reported by Marchis et al. (2005). We find close agreement in semi-major axes (within uncertainties). The eccentricities are marginally consistent. Orbital plane orientations differ by about $\lesssim$2 degrees. The largest discrepancy between our orbital solutions is the value of J_2. Our fits yield a very well-constrained J_2 value with a 1σ confidence range of 0.0985−0.1. Marchis et al.

(2005) report two estimates for J_2 of 0.17 ± 0.05 and 0.18 ± 0.01, inconsistent with our value. Using axial ratios from lightcurve analysis (Kaasalainen et al. 2002) and a uniform density assumption, we find $J_2 = 0.1$, in excellent agreement with our dynamical value.

There are several possibilities to explain the discrepancies between our orbital solutions and those of Marchis et al. (2005). First, our orbital fits are based on a much longer baseline of observations (2001−2011) than their dataset (only 2004). Second, our orbital solution is the result of fully dynamical, N-body orbital fits that simultaneously fitted for all parameters in the system, using numerical integrations taking into account mutually interacting orbits and primary oblateness. The fit obtained by Marchis et al. (2005) used two-body approximations (one satellite's orbit is fit at a time, ignoring effects by the other satellite). These differences in dataset and technique allowed us to obtain better-constrained orbital parameters with smaller uncertainties as well as individual masses, which were not previously known.

4. Examination of Mean-Motion Resonance Occupancy

The orbital periods (ratio ≈ 2.661) of our best-fit solution in Table 4 have a ratio near 8:3 (ratio ≈ 2.667). To determine resonance occupation, we search for librating resonance arguments using a general form of the resonance argument (Murray & Dermott 1999)

$$\phi = j_1\lambda_2 + j_2\lambda_1 + j_3\varpi_2 + j_4\varpi_1 + j_5\Omega_2 + j_6\Omega_1. \quad (2)$$

In Equation (2), ϕ is the resonant argument or angle, λ is the mean longitude, ϖ is the longitude of pericenter, and Ω is the longitude of the ascending node. Subscripts 1 and 2 represent the inner and outer satellites, respectively. The j_i values (where $i = 1 - 6$) are integers and their sum must equal zero (d'Alembert's rule). For the fifth-order 8:3 mean-motion resonance, $j_1 = -8$ and $j_2 = 3$ so we search through integer values (-30 to $+30$) of the remaining j_i values to determine if there is libration of the resonant argument over timescales ranging from 10 to 100 years. To perform this search, we determined the evolution of the relevant angles in Equation (2) using 3-body numerical integrations with the best-fit orbital, mass, and J_2 solution in Table 4. We do not find any librating resonance arguments, and therefore we conclude that the current system is not in the 8:3 mean-motion resonance.

5. Short-term and Long-term Stability

In this section, we discuss the results of forward N-body integrations of the best-fit orbital solution at MJD 53227 given in Table 4. We perform short-term (50 yr) and long-term (1 Myr) simulations to determine how the orbital elements fluctuate with time and to assess the stability of this three-body system. Both short-term and long-term integrations are performed using a Bulirsch-Stoer algorithm in `Mercury` (Chambers 1999) with an initial timestep of 0.05 days, and include the gravitational effects of the three bodies and the primary's oblateness. For long-term integrations, we also include the effect of solar gravitational perturbations.

The results of our short-term integrations are shown in Figure 5. This figure illustrates how the semi-major axes and eccentricities of both satellites evolve over a span of 50 years. From this figure, we can compute the mean value of orbital elements, in contrast to the osculating orbital elements provided in Table 4 that are valid at the specific epoch of MJD 53227.0. The semi-major axes for both Remus and Romulus have small oscillations spanning less than 1 km, and have mean values of 706.57 km and 1356.83 km, respectively. The mean eccentricity values are 0.029 for Remus and 0.0074 for Romulus. The eccentricity variations are especially apparent for Remus, whose eccentricity can vary from 0.023 to 0.035. These short-period fluctuations are due to the effect of the oblateness J_2 of the primary. The force due to the primary's gravitational field can be modified to account for primary J_2, and this modified force affects a satellite's orbit by inducing short-period fluctuations in the semi-major axis, mean motion, eccentricity, and mean anomaly. Its effect on eccentricity can be mathematically approximated as (Brouwer 1959; Greenberg 1981)

$$\Delta e \approx 3J_2(R_p/a)^2, \tag{3}$$

where Δe is the maximum eccentricity excursion from minima to maxima and R_p is the primary's radius. Plugging in values of $J_2 = 0.09959$, $R_p = 140$ km, and $a = 706.57$ km (Remus) and 1356.83 km (Romulus), we compute $\Delta e \approx 0.0117$ for Remus and $\Delta e \approx 0.00318$ for Romulus. These values are consistent with the maximum excursions seen in numerical simulations that are plotted in Figure 5. Since Remus has a smaller separation ($\sim$5 R_p) from the primary than Romulus ($\sim$9.7 R_p), its perturbation by primary J_2 is stronger, hence the larger eccentricity variations seen in Figure 5. As for precession of the orbital planes, there is significant precession due to J_2 and the presence of the other satellite. For example, Remus' longitude of pericenter precesses $\sim$560° per year due to J_2 and $\sim$1° per year due to Romulus.

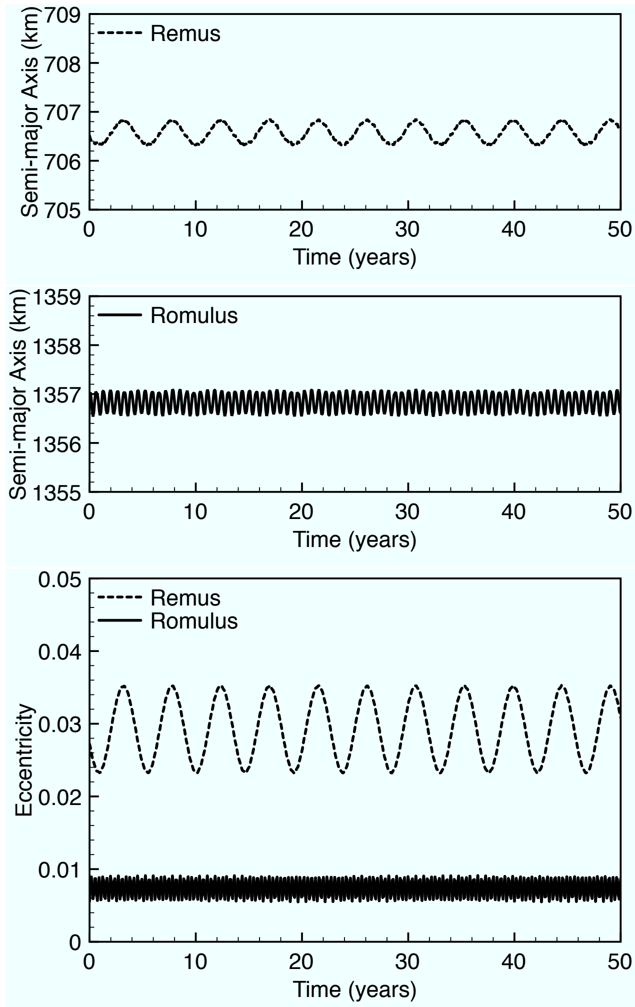

Fig. 5.— Variation of semi-major axis and eccentricity over a 50-year time span.

The results from our long-term integrations show that this triple system is stable over 1 Myr, and the variations in semi-major axis and eccentricity do not noticeably exceed the fluctuations shown in Figure 5 for the short-term integrations. Accordingly, we find that Sylvia is in a very stable configuration, as suggested by its near circular and coplanar orbital state. We find that the inclusion of the Sun's gravitational effect does not appreciably affect the semi-major axes and eccentricities of Sylvia's satellite orbits. If we consider Sylvia's Hill sphere of gravitational influence, defined as $r_{\rm Hill} = a_\odot (M/(3M_\odot))^{1/3}$ ($a_\odot$ is the heliocentric semi-major axis, M is the primary's mass, and $M_\odot$ is the mass of the Sun), we calculate that the satellites orbit at ∼1% and ∼2% of the Hill radius. As a result, they are both well within the primary's sphere of gravitational dominance over the Sun.

Our stability results are in agreement with two previous investigations on Sylvia's stability. Winter et al. (2009) performed stability analyses of the system, including the effects of the Sun and Jupiter. They find that Sylvia is not stable unless the primary has at least a minimal amount of oblateness (0.1% of their assumed primary J_2 of 0.17). They show that the inclusion of primary oblateness gives rise to a secular eigenfrequency that is much faster than those induced by other gravitational perturbations, which provides a stabilizing effect on the satellites' orbital evolution. Frouard & Compere (2012) investigated Sylvia's short-term (20 years) and long-term evolution (6600 years) including the primary's non-sphericity (assuming $J_2 \approx 0.14$) and solar perturbations. They also varied the semi-major axis and eccentricity of the satellites' orbits to determine the extent of their stability zones. They find that the current configuration of the system lies in a very stable zone. Authors from both papers (Winter et al. 2009; Frouard & Compere 2012) mention that the effect of Jupiter is negligible compared to the effect of the Sun.

6. Evolution of Orbital Configuration

In this section, we investigate the past orbital evolution of Remus and Romulus. We find that tidal perturbations can cause the orbits to evolve and to cross mean-motion resonances. This resonance passage may perturb orbits by increasing eccentricities. First we discuss how tidal processes likely caused the satellites to encounter the 3:1 mean-motion resonance in their past, then we describe our numerical modeling methods, and lastly we present plausible past evolutionary pathways as suggested by our simulation results.

6.1. Tidal Theory

Tidal evolution can cause the semi-major axis of an orbit to expand due to tides raised on the primary by its satellite (Goldreich 1963; Goldreich & Soter 1966). Tides raised on the satellite by the primary have an insignificant effect on the semi-major axis. The rate of semi-major axis evolution is given as

$$\frac{da}{dt} = 3\frac{k_p}{Q_p}\frac{M_s}{M_p}\left(\frac{R_p}{a}\right)^5 na, \tag{4}$$

where a is the semi-major axis, k is the tidal Love number, Q is the tidal dissipation factor, M is the mass, R is the radius, and n is the mean motion. The subscripts p and s denote quantities for the primary and satellite, respectively. It is likely that tidal evolution is causing the orbits of Remus and Romulus to expand, and that their orbits were in a more compact configuration in the past. We discuss the relative importance of tides compared to another important evolutionary process (BYORP) at the end of this subsection.

We expect that orbital expansion by tides is causing the relative orbits of Remus and Romulus to slowly converge towards each other. Two orbits are converging if $\dot{a}_1/\dot{a}_2$ is greater than one, and here subscripts 1 and 2 represent Remus (inner) and Romulus (outer), respectively. Using Equation (4), we can express this criterion as

$$\frac{\dot{a}_1}{\dot{a}_2} = \frac{M_1}{M_2}\left(\frac{a_2}{a_1}\right)^{11/2} > 1. \tag{5}$$

Assuming best-fit values for the semi-major axes of Remus and Romulus (Table 4), their orbits are currently converging as long as their mass ratio satisfies $M_1/M_2 > 0.0276$. Taking into account the range of the 1σ adopted confidence interval in masses (from Table 4), we find that this ratio is satisfied in all cases and therefore we expect that their orbits are converging. The steep dependence of tidal evolution on semi-major axis causes the orbit of Remus to expand much faster than the orbit of Romulus. Given that their orbits are slowly converging over time, we can determine the most recent mean-motion resonance passage encountered by the satellites. By considering all first, second, third, and fourth order resonances (where a $p+q$:p resonance is qth order), we expect that the most recent resonance encountered by the system is the second-order 3:1 resonance. Accordingly, in our analysis here we focus on the 3:1 resonance and its effect on the satellites' eccentricity evolution.

We describe how tidal evolution causes the eccentricity of an orbit to increase or decrease. This is a competing process between the opposing effects of tides raised on the primary (eccentricity increases) and tides raised on the satellite (eccentricity decreases). These two opposing effects are contained in two terms in the equation (Goldreich 1963; Goldreich & Soter 1966)

$$\frac{de}{dt} = \frac{57}{8}\frac{k_p}{Q_p}\frac{M_s}{M_p}\left(\frac{R_p}{a}\right)^5 ne - \frac{21}{2}\frac{k_s}{Q_s}\frac{M_p}{M_s}\left(\frac{R_s}{a}\right)^5 ne, \tag{6}$$

which gives the evolution of eccentricity e. The variables and subscripts in Equation (6) are the same as for Equation (4).

We discuss models for the tidal Love number k in Equations (4) and (6) used for calculations of tidal evolution in asteroids. These models are dependent on the asteroid's radius R. First, we consider the monolith model where

$$k \approx \frac{1.5}{1 + 2\times 10^8 \left(\frac{1\ \mathrm{km}}{R}\right)^2}, \tag{7}$$

and this model is appropriate for asteroids that are idealized as uniform bodies with no voids (Goldreich & Sari 2009). Second, we consider a rubble pile model by Goldreich & Sari (2009) with the following Love number formalism:

$$k \approx 1\times 10^{-5}\left(\frac{R}{1\ \mathrm{km}}\right). \tag{8}$$

Rubble pile models are appropriate for asteroids idealized as gravitational aggregates. Another rubble pile model is given by Jacobson & Scheeres (2011) where

$$k \approx 2.5\times 10^{-5}\left(\frac{1\ \mathrm{km}}{R}\right). \tag{9}$$

Equation (9) was obtained by fitting to the configurations of known asteroid binaries and assuming they are in an equilibrium state with tidal and BYORP effects canceling each other. Comparison between these three Love number models are given in Figure 6.

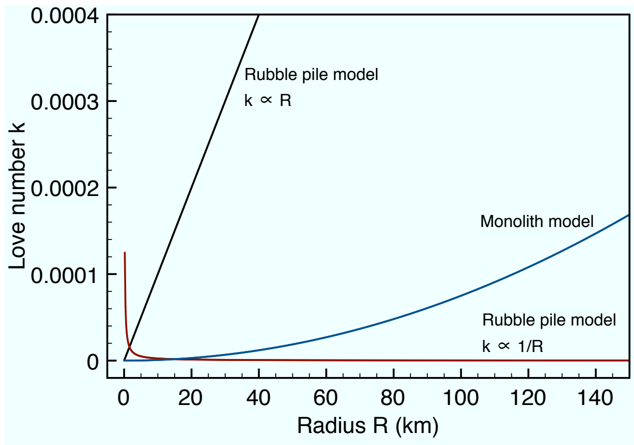

Fig. 6.— Tidal Love number models (Equations 7−9) as a function of radius. Intersections between the $k \propto 1/R$ model and the other two models occur at 1.58 km and 14.94 km.

Here we assume that tidal evolution is a dominant process and we do not analyze other evolutionary processes such as BYORP perturbations. BYORP is a radiative effect that is predicted to cause orbital evolution of a synchronous satellite on short timescales (Ćuk & Burns 2005; Ćuk 2007), and has not been observationally verified yet. BYORP effects dominate at larger semi-major axes, and tides dominate at smaller semi-major axes (Jacobson & Scheeres 2011). Tides result in an increase of the semi-major axes, but BYORP can result in an increase or a decrease, depending on the shapes of the satellites, which are unknown. For the purpose of our evolution calculations, the relevant semi-major axis rate is the *relative* migration rate of the satellites, and we compare the contributions by tides and BYORP by calculating $|(\dot{a}_{\rm tides,1} - \dot{a}_{\rm tides,2})/(\dot{a}_{\rm byorp,1} - \dot{a}_{\rm byorp,2})|$, with subscripts 1=inner and 2=outer. We find that this quantity is ∼1.4−3.3 (taking into account whether BYORP acts in the same or opposite directions for both satellites), and therefore we expect that tidal evolution will dominate the relative rate of the satellites' orbits as they converge. This calculation assumes current semi-major axes, $Q_p = 100$, and a monolith tidal Love number model for the primary. If BYORP causes the orbits of the satellites to converge, then joint evolution by tides and BYORP will result in a higher relative migration rate than the tides-only evolution considered here. If BYORP works against tides, then their joint evolution will be slower. Given the order-of-magnitude uncertainties already inherent in unknown tidal parameters such as Q and k as well as uncertainties in whether BYORP will expand or contract the satellites' orbits, we do not include the effects of BYORP in our simulations.

6.2. 3:1 Eccentricity-type Resonances

The 3:1 mean-motion resonance is the most recent low-order resonance encountered by Remus and Romulus, and here we briefly describe the relevant eccentricity-type resonances that can affect orbital eccentricities. We do not consider 3:1 inclination-type resonances in our simulations. There are 3 eccentricity-type resonances for the 3:1 mean-motion resonance: e_2^2 resonance which perturbs only the outer satellite's eccentricity, $e_1 e_2$ mixed resonance which perturbs both satellites' eccentricities, and the e_1^2 resonance which perturbs only the inner satellite's eccentricity. Subscripts 1 and 2 represent Remus (inner) and Romulus (outer), respectively.

The relevant resonance arguments ϕ for these three 3:1 eccentricity resonances are (e.g., Murray & Dermott 1999)

$$e_2^2: \qquad \phi = 3\lambda_2 - \lambda_1 - 2\varpi_2, \tag{10}$$

$$e_1 e_2: \qquad \phi = 3\lambda_2 - \lambda_1 - \varpi_1 - \varpi_2, \tag{11}$$

$$e_1^2: \qquad \phi = 3\lambda_2 - \lambda_1 - 2\varpi_1, \tag{12}$$

where λ is the mean longitude and ϖ is the longitude of pericenter. Occupation of any of these resonances requires libration of the considered resonance argument (exact resonance occurs when $\dot{\phi} = 0$). Note that $\dot{\lambda} = n$, where n is the mean motion and is related to the semi-major axis.

The resonance arguments given in Equations (10)−(12) are listed in the order that these resonances are encountered due to tidal migration: first the e_2^2 (at $a_1/a_2 \approx 0.481$), then the e_1e_2 (at $a_1/a_2 \approx 0.483$), and lastly the e_1^2 (at $a_1/a_2 \approx 0.485$), where the resonance locations a_1/a_2 must be adjusted depending on the exact starting values of a_1 and a_2. These resonances are not located at the same semi-major axes; differentiation of Equations (10)−(12) shows that the various resonant arguments will librate at different values of n_1 and n_2. Such "resonance splitting" occurs because perturbations such as the effect of primary J_2, and to a lesser degree (in this case, 2−3 orders of magnitude smaller), secular perturbations, causes ϖ of the satellites to precess at different rates. In Section 6.4, we will discuss the capture of Remus and Romulus into any of these resonances. Next, we describe our methods regarding the implementation of tidal effects using direct N-body integrations.

6.3. Methods

Our methods and implementation for simulating a 3:1 resonant passage due to tidal migration are as follows. We use an N-body integrator with a variable-timestep Bulirsch-Stoer algorithm from `Mercury` (Chambers 1999). We implement additional terms in the equations of motion due to the effects of tides on semi-major axis and eccentricity by following the numerical methods described in Appendix A of Lee & Peale (2002). Specifically, we used Equations (4) and (6) to model the tidal evolution in time of a and e. We have tested our implementation by reproducing results in Lee & Peale (2002) as well as matching the analytical expectations (Equations (4) and (6)) of semi-major axis drift and eccentricity evolution outside of resonance.

Actual tidal timescales can be computationally prohibitive, and we incorporate a "speedup" factor to artificially increase the rate of tidal evolution in our simulations. Such speedup factors have also been numerically implemented in previous studies of tidal migration (i.e., Ferraz-Mello et al. 2003; Meyer & Wisdom 2008; Zhang & Nimmo 2009), where they adopted values up to 1000 and found that their results were not sensitive to the choice of speedup factor in the range 1-1000. In our implementation, we incorporate a speedup factor by multiplying Equations (4) and (6) by typical speedup factors of $100 - 1000$. In agreement with previous studies, we find that our results are not sensitive to the choice of speedup factors up to 1000 for select test cases.

We integrate the system for artificial durations of 1-10 Myr, which, because of the speedup factors, represent 1 Gyr of tidal evolution. Our figures show the tidal evolution timescale, not the artifical timescale used in the integrator. The 1 Gyr timescale is constrained by the lifetime of Sylvia's satellite system. Work by Vokrouhlický et al. (2010) investigating the collisionally-born asteroid family related to Sylvia suggests that the family members (and hence the satellites) are at least 10^8 years old. We can also estimate the lifetime of the satellites by considering how much time would pass before a collision between one of the satellites and another main belt asteroid. We estimate this timescale to be roughly 10^9 years (Farinella et al. 1998; Bottke et al. 2005) by assuming that the smallest satellite has a diameter of 10.6 km, as suggested by our orbital fit analysis (Section 3). Accordingly, we consider 1 Gyr to be a reasonable time within which tidal evolution can have taken place, and we typically do not run simulations longer than 1 Gyr.

For the default set of initial conditions in our simulations, the masses of all bodies and primary oblateness (J_2) are taken from Table 4. Simulations are started with coplanar and nearly circular ($e = 0.001$) orbits. Angles for the argument of pericenter and mean anomaly are given a random value from 0° to 360°. Initial semi-major axes for Remus and Romulus are 654 km and 1352.5 km, just inside the 3:1 resonance location. To simulate tidal evolution, we also need to adopt values for the Love number k and tidal dissipation factor Q. To calculate the Love number, we use the tidal monolith model for these bodies (see e.g., Goldreich & Sari 2009). For all bodies, we assume $Q = 100$, a reasonable assumption for rocky monoliths.

We also ran additional sets of simulations where we varied the initial eccentricities of both satellites (0.001−0.050), primary J_2 (5−10% lower and higher than its best-fit value), satellite masses that spanned the range of adopted 1σ confidence intervals (low−high, low−low, high−low, high−high combinations), and repeats of the nominal configuration for additional randomized initial angles of the argument of pericenter and mean anomaly. We did not specifically vary the tidal quantity k/Q, as the effect of varying k/Q is the same as varying the speedup factor since they both contribute linearly to $\dot{a}$ and $\dot{e}$. We describe our results in the next subsection.

6.4. Results: Evolutionary Pathways

Here we describe the results stemming from our simulations of a 3:1 resonant passage between Remus and Romulus. These results suggest three evolutionary pathways: capture into resonance with no escape, temporary capture followed by escape, and no capture. We describe each of these evolutionary pathways in the following paragraphs.

6.4.1. Capture with no escape

This scenario, where resonant capture occurs with no escape during the 1 Gyr evolution, was typically observed for the e_2^2 resonance. An example of such evolution is shown in Figure 7. Given that (a) the satellites are not currently observed in the 3:1 resonance and (b) these simulations show no escape from such resonant capture within a reasonable system lifetime of 1 Gyr, we conclude that this evolutionary pathway did not occur and we do not discuss it further.

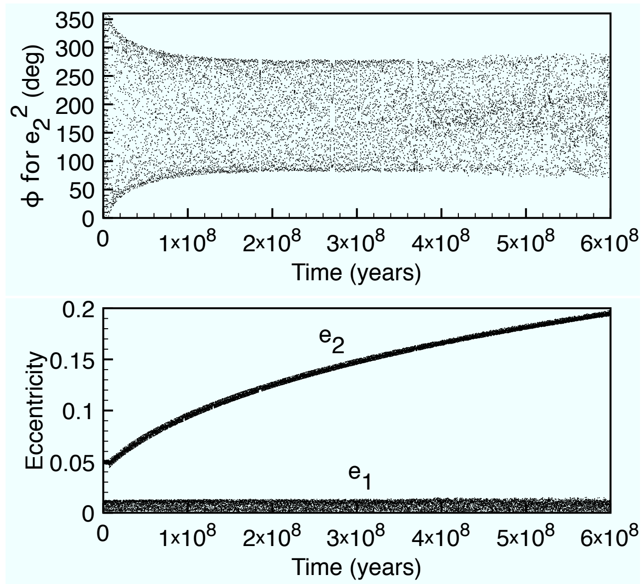

Fig. 7.— Example of a simulation with resonant capture into e_2^2 and no escape. Dots show results from numerical simulations for the libration angle ϕ and eccentricity e as a function of time. Subscripts 1 and 2 represent the inner and outer satellites, respectively. The simulation was started at $a_1/a_2 = 654.0/1352.5 = 0.4835$ and reached the e_2^2 resonance at $a_1/a_2 = 655.2/1352.5 = 0.4844$, roughly 8 Myr after the start of the simulation. The outer satellite's eccentricity will continue to increase due to the resonance effects, but the tidal damping effects will increase as the eccentricity grows, such that an equilibrium value for e may be reached.

6.4.2. Temporary capture followed by escape

In this event, resonant capture occurs and is followed by eventual escape due to growth of the resonant argument. This was a common outcome for each of the 3 types of resonances. Examples of such evolution are shown in Figure 8. Final eccentricities at the end of our simulations ranged from their initial values up to ∼0.3. We are unable to place lower bounds on the final eccentricities because we cannot assess how long the satellites may have been captured in the resonance. If high eccentricities resulted from temporary resonance capture, then sufficient eccentricity damping may have subsequently occurred to bring high post-resonance eccentricities to low observed eccentricities.

We investigated whether such eccentricity damping was possible within a conservative timeframe of 1 Gyr. To do so, we integrated the $\dot{a}$ and $\dot{e}$ tidal expressions in Equations (4) and (6) and considered all Love number models (Equations 7−9), various post-resonance eccentricities up to 0.25, and tidal dissipation Q values (10−1000). We assumed that both satellites had densities equal to that of the primary (1.29 g cm^{-3}).

For Remus, we find that eccentricity damping to observed values is only possible if we assume rubble pile Love number models (either $k \propto R$ or $k \propto 1/R$) for Remus (there is no restriction on the primary). If we make this assumption, damping to observed values is possible by adopting reasonable values of $Q_p = 100$ and $Q_s = 10-100$. When we assume that Remus is monolithic, even when we adopt very favorable conditions for eccentricity damping[3], tidal damping to its observed value is only possible if we assume a post-resonance eccentricity of ∼0.032 or less. These calculations suggest that if its post-resonance eccentricity exceeded ∼0.032, it is likely that Remus may have an interior structure more akin to a rubble pile aggregate than a monolithic body.

For Romulus, damping to observed eccentricities is possible only if the eccentricity was barely affected while in the resonance (as well as assuming favorable dissipations conditions: $Q_p = 1000$ and $Q_s = 10$). If the eccentricity reached even modest values (~ 0.023) we find that none of the Love number models and reasonable $Q = 10 - 1000$ values can damp eccentricities to even the highest possible observed eccentricity (0.011) allowed by our fit uncertainties. Therefore, if temporary capture in the 3:1 occurred, it must not have lasted long enough for the eccentricity of Romulus to reach values of ~ 0.023. While such a scenario does not entirely rule out the e_2^2 and $e_1 e_2$ resonances, it does seem to place bounds on the

[3] $Q_p = 1000$ and $Q_s = 10$. Inspection of Equation (6) shows that damping can be speeded up by making Q_p/Q_s as large as possible.

acceptable increase in eccentricity due to the 3:1 resonance.

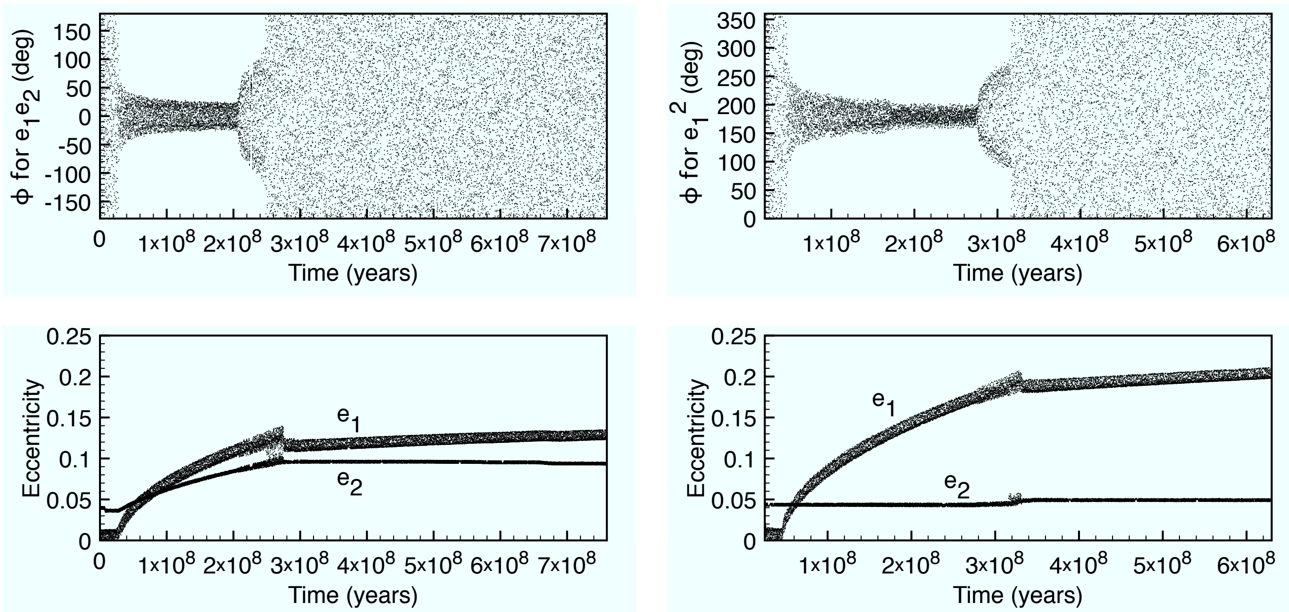

Fig. 8.— Examples of simulations with temporary resonant capture followed by escape. Dots show results from numerical simulations for the libration angle ϕ and eccentricity e as a function of time. Subscripts 1 and 2 represent the inner and outer satellites, respectively. **Left-side plots:** Results of a simulation with temporary capture into e_1e_2 resonance, where both e_1 and e_2 increase. Initial conditions for eccentricity are $e_1 = 0.001$ and $e_2 = 0.04$. **Right-side plots:** Results of a simulation with temporary capture into e_1^2 resonance, where only e_1 increases. Initial conditions for eccentricity are $e_1 = 0.007$ and $e_2 = 0.04$.

6.4.3. No capture

In this case, all eccentricity-type resonances are encountered and none result in capture. For orbits that are slowly converging toward each other, capture is possible depending on their initial eccentricities. When the pre-encounter eccentricity is below a critical eccentricity, capture is guaranteed. When the pre-encounter eccentricity exceeds a critical eccentricity, capture becomes a probabilistic event. For the 3:1 resonance, critical eccentricities can be estimated as (Murray & Dermott 1999)

$$e_{1,\mathrm{crit}} = \left[\frac{3}{32 f_1}\left(3^{2/3}\frac{M_p}{M_2} + 3^{4/3}\frac{M_1}{M_2}\frac{M_p}{M_2}\right)\right]^{-1/2}, \tag{13}$$

$$e_{2,\mathrm{crit}} = \left[\frac{3}{32 f_2}\left(3^{2/3}\frac{M_2}{M_1}\frac{M_p}{M_1} + 9\frac{M_p}{M_1}\right)\right]^{-1/2}, \tag{14}$$

where subscripts p, 1, and 2 represent the primary, Remus, and Romulus, respectively. The f_1 and f_2 terms represent functions of Laplace coefficients $b_{1/2}^{(j)}(\alpha)$. They are (e.g., see Murray & Dermott 1999)

$$f_1 = \frac{1}{8}(-5j + 4j^2 - 2\alpha D + 4j\alpha D + \alpha^2 D^2) b_{1/2}^{(j)}(\alpha), \tag{15}$$

$$f_2 = \frac{1}{8}(2 - 7j + 4j^2 - 2\alpha D + 4j\alpha D + \alpha^2 D^2) b_{1/2}^{(j-2)}(\alpha) - \frac{27}{8}\alpha, \tag{16}$$

where $j = 3$ for the 3:1 resonance, $\alpha = a_1/a_2$ is the ratio of semi-major axes, and $D = d/d\alpha$ is the differential operator. The quantity $-27\alpha/8$ in Equation (16) is the indirect term for the case when $M_2 > M_1$.

Using Equations (13) and (14), we calculate the critical eccentricities to be $e_{1,\mathrm{crit}} = 0.00864$ and $e_{2,\mathrm{crit}} = 0.00410$. Even for initial e_1 values that are low (e.g., osculating value of 0.001), $e_1 < e_{1,\mathrm{crit}}$ will not always be satisfied because short-term eccentricity fluctuations due to primary J_2 will inflate e_1 excursions up to $\sim$0.014 (assuming $a_1 = 654$ km in Equation (3) of Section 5). For Romulus, marooned farther from the primary such that J_2 effects are lessened, if the pre-encounter eccentricity is low enough then it is possible that the eccentriciy will always remain less than the critical eccentricity. These analytical arguments are in agreement with the results from our numerical experiments.

If we contemplate scenarios in which resonant capture never occurred in Sylvia's past, then we must adopt the critical eccentricities as lower limits on the past eccentricities of Remus and Romulus. Their past eccentricities cannot be lower than these limits because otherwise capture would have been guaranteed. We note that these lower limit eccentricities are lower than the nominal observed eccentricities (Table 4), and hence this evolutionary pathway is a plausible scenario without requiring any significant modifications in eccentricity over time.

To summarize these results, from these 3 pathways we find that both (a) temporary capture followed by escape and (b) no capture are plausible scenarios that occurred when Remus and Romulus encountered the 3:1 resonance. If pathway (a) occurred, our calculations of the necessary damping required to bring post-resonance eccentricities to observed values show this is possible for Remus but may be prohibitively long for Romulus, depending on its post-resonance eccentricity. Therefore it is unlikely that a substantial increase in the eccentricity of Romulus occurred, even if the system was temporarily captured in the e_2^2 or $e_1 e_2$ resonances. If pathway (b) occurred, we can set lower limits on past eccentricities of both satellites to be equal to their critical eccentricities.

7. Conclusions

The goals of this study were to characterize Sylvia's current orbital configuration and masses as well as to illuminate the past orbital evolution of this system. Our work can be summarized as follows:

(1) We reported new astrometric observations of Sylvia in 2011 that increased the number of existing epochs of astrometry by over 50%. These new observations extended the existing baseline of observations to 7 years (for Remus) and to 10 years (for Romulus).

(2) We fit a fully dynamical 3-body model to the available astrometric data. This model simultaneously solved for orbits of both satellites, individual masses, and the primary's oblateness (Table 4). We found that the primary has a density of 1.29 ± 0.39 g cm^{-3} and is oblate with a J_2 value in the range of $0.0985-0.1$. Constraints on satellite radii can be obtained from the mass determinations by assuming that the satellites have a bulk density equal to that of the primary; we find $\sim$4.5$-$6.1 km for Remus and $\sim$2.6$-$8.2 km for Romulus.

These ranges would have to be modified if the actual density of the primary or of the satellites was different from the nominal value assumed here. The orbits of the satellites are relatively circular. We find that the primary's spin pole is best fit when aligned to Romulus' orbital pole, and that the satellites' orbit poles are coplanar to within one degree.

(3) We numerically investigated the short-term and long-term stability of the orbits of Sylvia's satellites. There are periodic fluctuations in eccentricity for both satellites, most notably for the inner satellite Remus. We verified that these eccentricity excursions are due to the effects of primary oblateness. From long-term integrations we found that the system is in a very stable configuration, in agreement with previous investigations.

(4) We studied the past orbital evolution of Sylvia's satellites, including the most recent low-order MMR resonance crossing, which is the 3:1. We used direct N-body integrations with forced tidal migration to model such an encounter. To examine the case of resonant capture followed by escape, we calculate the tidal damping timescale to go from the post-encounter eccentricity to the observed value. Using available tidal models, we find that the damping timescale for Romulus can be prohibitively large if its post-resonance eccentricity exceeded $\sim$0.023. This suggests that the system crossed the e_2^2 and $e_1 e_2$ resonances without capture, or that it was not captured in these resonances for a sufficient duration to substantially increase the eccentricity of Romulus. Similar timescale constraints from tidal damping also imply that Remus may have a rubble pile structure if its post-resonance eccentricity exceeded $\sim$0.032. Alternatively, if no capture in any resonance occurred then we are able set lower limits on their past eccentricities ($e_1 = 0.00864$ and $e_2 = 0.00410$).

The detailed characterization of Sylvia presented in this paper has allowed for analyses of its orbital evolution. Such studies of triple systems are important in order to understand their key physical properties, orbital architectures, and intriguing evolutionary histories.

REFERENCES

Benecchi, S., Noll, K., Grundy, W., & Levison, H. 2010, Icarus, 207, 978

Bottke, W. F., Durda, D. D., Nesvorný, D., Jedicke, R., Morbidelli, A., Vokrouhlický, D., & Levison, H. F. 2005, Icarus, 179, 63

Brouwer, D. 1959, AJ, 64, 378

Brown, M. E., Bouchez, A. H., Rabinowitz, D., Sari, R., Trujillo, C. A., van Dam, M., Campbell, R., Chin, J., Hartman, S., Johansson, E., Lafon, R., Le Mignant, D., Stomski, P., Summers, D., & Wizinowich, P. 2005, ApJ, 632, L45

Brown, M. E. & Margot, J. L. 2001, IAU Circ., 7588, 1

Brown, M. E., van Dam, M. A., Bouchez, A. H., Le Mignant, D., Campbell, R. D., Chin, J. C. Y., Conrad, A., Hartman, S. K., Johansson, E. M., Lafon, R. E., Rabinowitz, D. L., Stomski, Jr., P. J., Summers, D. M., Trujillo, C. A., & Wizinowich, P. L. 2006, ApJ, 639, L43

Brozovic, M., Benner, L. A. M., Nolan, M. C., Howell, E. S., Magri, C., Giorgini, J. D., Taylor, P. A., Margot, J. L., Busch, M. W., Shepard, M. K., Carter, L. M., Jao, J. S., van Brimmer, J., Franck, C. R., Silva, M. A., Kodis, M. A., Kelley, D. T., Slade, M. A., Bramson, A., Lawrence, K. J., Pollock, J. T., Pravec, P., Reichart, D. E., Ivarsen, K. M., Haislip, J., Nysewander, M. C., & Lacluyze, A. P. 2009, IAU Circ., 9053, 2

Cash, W. 1976, A&A, 52, 307

Chambers, J. E. 1999, MNRAS, 304, 793

Ćuk, M. 2007, ApJ, 659, L57

Ćuk, M. & Burns, J. A. 2005, Icarus, 176, 418

Descamps, P., Marchis, F., Berthier, J., Emery, J. P., Duchêne, G., de Pater, I., Wong, M. H., Lim, L., Hammel, H. B., Vachier, F., Wiggins, P., Teng-Chuen-Yu, J.-P., Peyrot, A., Pollock, J., Assafin, M., Vieira-Martins, R., Camargo, J. I. B., Braga-Ribas, F., & Macomber, B. 2011, Icarus, 211, 1022

Drummond, J. & Christou, J. 2008, Icarus, 197, 480

Fang, J., Margot, J.-L., Brozovic, M., Nolan, M. C., Benner, L. A. M., & Taylor, P. A. 2011, AJ, 141, 154

Farinella, P., Vokrouhlicky, D., & Hartmann, W. K. 1998, Icarus, 132, 378

Ferraz-Mello, S., Beaugé, C., & Michtchenko, T. A. 2003, Celestial Mechanics and Dynamical Astronomy, 87, 99

Frouard, J. & Compere, A. 2012, Icarus, 220, 149

Goldreich, P. 1963, MNRAS, 126, 257

Goldreich, P. & Sari, R. 2009, ApJ, 691, 54

Goldreich, P. & Soter, S. 1966, Icarus, 5, 375

Greenberg, R. 1981, AJ, 86, 912

Jacobson, S. A. & Scheeres, D. J. 2011, ApJ, 736, L19

Kaasalainen, M., Torppa, J., & Piironen, J. 2002, Icarus, 159, 369

Kryszczyńska, A., La Spina, A., Paolicchi, P., Harris, A. W., Breiter, S., & Pravec, P. 2007, Icarus, 192, 223

Lee, M. H. & Peale, S. J. 2002, ApJ, 567, 596

—. 2006, Icarus, 184, 573

Lenzen, R., Hartung, M., Brandner, W., Finger, G., Hubin, N. N., Lacombe, F., Lagrange, A.-M., Lehnert, M. D., Moorwood, A. F. M., & Mouillet, D. 2003, in Society of Photo-Optical Instrumentation Engineers (SPIE) Conference Series, Vol. 4841, Society of Photo-Optical Instrumentation Engineers (SPIE) Conference Series, ed. M. Iye & A. F. M. Moorwood, 944–952

Lin, C.-L., Zhang, Z.-W., Chen, W. P., King, S.-K., Lin, H.-C., Wang, J.-H., Mondal, S., Alcock, C., Axelrod, T., Bianco, F. B., Byun, Y.-I., Coehlo, N. K., Cook, K. H., Dave, R., de Pater, I., Descamps, P., Lehner, M. J., Kim, D.-W., Lee, T., Lissauer, J. J., Marshall, S. L., Porrata, R., Protopapas, P., Rice, J. A., Schwamb, M. E., Wang, S.-Y., & Wen, C.-Y. 2009, PASP, 121, 359

Marchis, F., Baek, M., Descamps, P., Berthier, J., Hestroffer, D., & Vachier, F. 2007, IAU Circ., 8817, 1

Marchis, F., Descamps, P., Dalba, P., Enriquez, J. E., Durech, J., Emery, J. P., Berthier, J., Vachier, F., Merlbourne, J., Stockton, A. N., Fassnacht, C. D., & Dupuy, T. J. 2011, in EPSC-DPS Joint Meeting 2011, held 2-7 October 2011 in Nantes, France. ¡A href=”http://meetings.copernicus.org/epsc-dps2011”¿http://meetings.copernicus.org/epsc-dps2011¡/A¿, p.653, 653

Marchis, F., Descamps, P., Hestroffer, D., Berthier, J., Brown, M. E., & Margot, J.-L. 2005, IAU Circ., 8582, 1

Marchis, F., Pollock, J., Pravec, P., Baek, M., Greene, J., Hutton, L., Descamps, P., Reichart, D. E., Ivarsen, K. M., Crain, J. A., Nysewander, M. C., Lacluyze, A. P., Haislip, J. B., & Harvey, J. S. 2008, IAU Circ., 8928, 4

Margot, J. L. & Brown, M. E. 2001, in Bulletin of the American Astronomical Society, Vol. 33, AAS/Division for Planetary Sciences Meeting Abstracts #33, 1133

Margot, J. L., Brown, M. E., Trujillo, C. A., Sari, R., & Stansberry, J. A. 2005, in Bulletin of the American Astronomical Society, Vol. 37, AAS/Division for Planetary Sciences Meeting Abstracts #37, 737

Margot, J. L., Nolan, M. C., Benner, L. A. M., Ostro, S. J., Jurgens, R. F., Giorgini, J. D., Slade, M. A., & Campbell, D. B. 2002, Science, 296, 1445

Markwardt, C. B. 2009, in Astronomical Society of the Pacific Conference Series, Vol. 411, Astronomical Data Analysis Software and Systems XVIII, ed. D. A. Bohlender, D. Durand, & P. Dowler, 251

Merline, W. J., Close, L. M., Dumas, C., Chapman, C. R., Roddier, F., Menard, F., Slater, D. C., Duvert, G., Shelton, C., & Morgan, T. 1999, Nature, 401, 565

Merline, W. J., Close, L. M., Siegler, N., Dumas, C., Chapman, C., Rigaut, F., Menard, F., Owen, W. M., & Slater, D. C. 2002, IAU Circ., 7827, 2

Meyer, J. & Wisdom, J. 2008, Icarus, 193, 213

Murray, C. D. & Dermott, S. F. 1999, Solar system dynamics, ed. Murray, C. D. & Dermott, S. F.

Naidu, S. P., Margot, J. L., Busch, M. W., Taylor, P. A., Nolan, M. C., Howell, E. S., Giorgini, J. D., Benner, L. A. M., Brozovic, M., & Magri, C. 2011, in EPSC-DPS Joint Meeting, Vol. 6

Nolan, M. C., Howell, E. S., Becker, T. M., Magri, C., Giorgini, J. D., & Margot, J. L. 2008, in Bulletin of the American Astronomical Society, Vol. 40, AAS/Division for Planetary Sciences Meeting Abstracts #40, 432

Noll, K. S., Grundy, W. M., Chiang, E. I., Margot, J.-L., & Kern, S. D. 2008, Binaries in the Kuiper Belt, ed. Barucci, M. A., Boehnhardt, H., Cruikshank, D. P., Morbidelli, A., & Dotson, R., 345–363

Ostro, S. J., Margot, J. L., Benner, L. A. M., Giorgini, J. D., Scheeres, D. J., Fahnestock, E. G., Broschart, S. B., Bellerose, J., Nolan, M. C., Magri, C., Pravec, P., Scheirich, P., Rose, R., Jurgens, R. F., De Jong, E. M., & Suzuki, S. 2006, Science, 314, 1276

Press, W. H., Teukolsky, S. A., Vetterling, W. T., & Flannery, B. P. 1992, Numerical recipes in C. The art of scientific computing, ed. Press, W. H., Teukolsky, S. A., Vetterling, W. T., & Flannery, B. P.

Ragozzine, D. & Brown, M. E. 2009, AJ, 137, 4766

Rousset, G., Lacombe, F., Puget, P., Hubin, N. N., Gendron, E., Fusco, T., Arsenault, R., Charton, J., Feautrier, P., Gigan, P., Kern, P. Y., Lagrange, A.-M., Madec, P.-Y., Mouillet, D., Rabaud, D., Rabou, P., Stadler, E., & Zins, G. 2003, in Society of Photo-Optical Instrumentation Engineers (SPIE) Conference Series, Vol. 4839, Society of Photo-Optical Instrumentation Engineers (SPIE) Conference Series, ed. P. L. Wizinowich & D. Bonaccini, 140–149

Shepard, M. K., Margot, J. L., Magri, C., Nolan, M. C., Schlieder, J., Estes, B., Bus, S. J., Volquardsen, E. L., Rivkin, A. S., Benner, L. A. M., Giorgini, J. D., Ostro, S. J., & Busch, M. W. 2006, Icarus, 184, 198

Storrs, A., Vilas, F., Landis, R., Wells, E., Woods, C., Zellner, B., & Gaffey, M. 2001, IAU Circ., 7590, 3

Tholen, D. J., Buie, M. W., Grundy, W. M., & Elliott, G. T. 2008, AJ, 135, 777

Vokrouhlický, D., Nesvorný, D., Bottke, W. F., & Morbidelli, A. 2010, AJ, 139, 2148

Weaver, H. A., Stern, S. A., Mutchler, M. J., Steffl, A. J., Buie, M. W., Merline, W. J., Spencer, J. R., Young, E. F., & Young, L. A. 2006, Nature, 439, 943

Winter, O. C., Boldrin, L. A. G., Vieira Neto, E., Vieira Martins, R., Giuliatti Winter, S. M., Gomes, R. S., Marchis, F., & Descamps, P. 2009, MNRAS, 395, 218

Zhang, K. & Nimmo, F. 2009, Icarus, 204, 597

Chapter 3

Architecture of Planetary Systems Based on *Kepler* Data: Number of Planets and Coplanarity

Reproduced by permission of the AAS (Fang, J., and Margot, J.L., 2012, The Astrophysical Journal, 761, 92).

1. Introduction

Knowledge of the architecture of planetary systems can provide important constraints and insights into theories of planet formation and evolution. For instance, planetary systems with a high degree of coplanarity or alignment, such as the Solar System, are consistent with the standard formation model of planets forming in a protoplanetary disk. Additionally, planetary systems with inclined or misaligned orbits can be indicative of past events that increased eccentricities and inclinations (e.g., Kozai oscillations by outlying perturbers, resonant encounters between planets, or planet-planet scattering). Consequently, information on planetary multiplicity and the distribution of inclinations can reveal fundamental events in the lives of planetary systems as well as test theories of planet formation and evolution.

Because of observational biases, it may be difficult to reliably assess the underlying multiplicity of planets and their inclination distributions. Planets may go undetected if they have masses/radii below detection limits or if they are non-transiting (for the case of transit surveys). As for inclinations, mutual (or relative) inclinations between planets in the same system have only been measured in a limited number of cases or indirectly constrained. Examples include the planets orbiting the pulsar PSR B1257+12 (Konacki & Wolszczan 2003), the planets GJ 876 b and c using radial velocity and/or astrometric data (Bean & Seifahrt 2009; Correia et al. 2010; Baluev 2011), υ And planets c and d using astrometric and radial velocity data (McArthur et al. 2010), using transit timing/duration analyses to constrain inclinations in the Kepler-9 system (Holman et al. 2010), Kepler-10 system (Batalha et al. 2011; Fressin et al. 2011), and Kepler-11 system (Lissauer et al. 2011a), and analyzing transits of planets over starspots for Kepler-30 (Sanchis-Ojeda et al. 2012).

However, there now exists substantial knowledge about a large sample of planetary systems that can be used to statistically determine the underlying number of planets in each system and their relative orbital inclinations. In particular, the haul of planetary candidates cataloged by the *Kepler* mission (current count is over 2,300; Borucki et al. 2011a,b; Batalha et al. 2012) provides a large trove of systems to study. These *Kepler* detections are termed planetary candidates, because most of them have not been formally confirmed as real planets by independent observations such as radial velocity detections or successful elimination of false positive scenarios. We will refer to *Kepler* planetary candidates interchangeably as planetary "candidates" or "planets."

In the present study, we use the latest *Kepler* catalog of planetary candidates (identified in Quarters 1 through 6) released by Batalha et al. (2012) to constrain the underlying multiplicity and inclinations of planetary systems discovered by *Kepler*. By "underlying," we are referring to our estimate of the true distributions free of observational biases. In our analysis, we create thousands of model populations, each obeying different underlying multiplicity and inclination distributions. These planetary systems are subject to artificial observations to determine which planets could be transiting and detectable by *Kepler*. The detectable planets and their properties are compared to the observed sample to determine each model's goodness-of-fit to the data. Our results show that the underlying architecture of planetary systems is typically thin (low relative inclinations) with few planets with orbital periods under 200 days. Similarly, other statistical studies have been performed to constrain multiplicity and/or inclinations using different methodologies or data sets (e.g., Lissauer et al. 2011b; Tremaine & Dong 2012; Figueira et al. 2012; Fabrycky et al. 2012; Weissbein et al. 2012; Johansen et al. 2012). Our analysis improves on previous work by including all available *Kepler* quarters, extending to 200-day orbital periods, and fitting models to observables such as normalized transit duration ratios that contain information on mutual orbital inclinations; these improvements lend to a deeper investigation of the intrinsic distributions of planetary systems.

This paper is organized as follows. Section 2 provides details on how we created model populations including choice of stellar and planetary properties. Section 3 describes how we determined detectable, transiting planets from our simulated populations as well as our methods for determining each model's goodness-of-fit compared to observations. Section 4 presents our main results with analysis of our best-fit models. Section 5 includes comparisons of our results with the Solar System and with previous work. Lastly, Section 6 summarizes the main conclusions of our study.

2. Creating Model Populations

This section describes our methods for creating model populations. Each model population consists of approximately 10^6 simulated planetary systems from which we determine planets detectable by *Kepler*. In total, we created thousands of model populations obeying different underlying planet (1) multiplicity and (2) inclination distributions.

2.1. Stellar Properties

Each model population's planetary systems have host stars with parameters drawn from a distribution of stellar properties. For each simulated system, we randomly drew a star from a subset of the quarterly KIC (*Kepler* Input Catalog; Brown et al. 2011) CDPP (Combined Differential Photometric Precision) lists[1] (Christiansen et al. 2012). There is a separate list per quarter, because each file only lists targets observed that quarter and

[1] http://archive.stsci.edu/pub/kepler/catalogs/

their corresponding CDPP noise levels over 3, 6, and 12 hours. These quarterly lists also include basic KIC parameters (unchanging in the quarterly lists) for each observed star such as its *Kepler* magnitude K_p, effective temperature $T_{\rm eff}$, surface gravity parameter $\log(g)$, and radius R_*.

We created a subset of the KIC CDPP lists in the following manner. First, we collected the KIC CDPP lists for Quarters 1 to 6 (Q1-6). Not all stars are observed each quarter and we counted a total of 189,998 unique stars observed at some point during Q1-6. Next, we filtered this list of unique stars such that we only included stars that were observed under the "exoplanet" program, have nonzero values for R_* and CDPP entries, and obey the following restrictions:

$$\begin{gathered} 4100\ \mathrm{K} \leq T_{\rm eff} \leq 6100\ \mathrm{K}, \\ 4.0 \leq \log(g\ [\mathrm{cm\ s^{-2}}]) \leq 4.9, \\ K_p \leq 15\ \mathrm{mag}. \end{gathered} \tag{1}$$

These stellar cuts allowed us to consider the brighter main-sequence stars with well-characterized properties in the KIC (consistent with those in Howard et al. 2012). With such filtering, we were left with a KIC subset of 59,224 remaining unique stars, which is roughly one-third of the original list of unique stars. For each star in this KIC subset, we calculated median CDPP values over 3, 6, and 12 hours from all the values available in the Q1-6 lists. We also used each star's surface gravity parameter $\log(g)$ and R_* values, which are common across the Q1-6 KIC CDPP lists, to calculate each star's mass. Finally, we recorded each star's observing history over Q1-6 as indicated by the quarterly KIC CDPP lists.

Our subset of the KIC with 59,224 stars was the catalog from which we randomly picked stellar hosts (with their corresponding properties) for each simulated planetary system. In the next subsections, we describe how we chose physical and orbital parameters for the planets in each system.

2.2. Planet Period and Radius Distribution

We assigned values for the period and radius of each simulated planet by drawing from debiased distributions. To create such debiased distributions, we started with the observed sample of *Kepler* candidate planets (or *Kepler* Objects of Interest; KOIs) and converted it to a debiased sample of planets using detection efficiencies. First we will discuss how we filtered the KOI catalog, and then we will discuss the calculation and application of detection efficiencies.

Our observed sample of KOIs is based on the February 2012 release (Q1-6) by Batalha et al. (2012) consisting of 2,321 planetary candidates in 1,790 systems. We only considered a subset of this KOI catalog by applying the following filters. First, we only considered planet candidates with positive values for their entries: we removed any planet candidates with negative values of the orbital period because such candidates are only based on a single transit (Batalha et al. 2012), and we also removed KOI 1611.02, the circumbinary planet also known as Kepler-16b (Doyle et al. 2011), because many of its entries in the catalog have negative values. This cut left us with 2,298 remaining candidates. Next, we filtered out any planetary candidates with host stars that did not obey Equation (1) for consistency with the simulated stellar population. This step filtered out about half of the sample; 1,135 candidates remained. Lastly, we made additional cuts based on planet radius, period, and SNR:

$$\begin{gathered} P \leq 200 \text{ days}, \\ 1.5\ R_\oplus \leq R \leq 30\ R_\oplus, \\ \mathrm{SNR}(\rightarrow \mathrm{Q8}) \geq 11.5. \end{gathered} \tag{2}$$

These specific cuts were performed in order to choose a sample of planetary candidates with period, radius, and SNR that are unlikely to be missed by the *Kepler* detection pipeline. It is necessary to choose a sample with a high degree of completeness because we want to compare this sample to simulations, which are normally 100% complete. For orbital periods, a range extending to 200 days ensures that multiple transits are likely to have been observed during Q1-6, which covers approximately 486.5 days. For planet radii, the lower bound on R of 1.5 $R_\oplus$ was chosen because the sample of observed planets with radii $R \lesssim 1.5\ R_\oplus$ has much lower detection efficiencies (e.g., Howard et al. 2012; Youdin 2011). For SNR, we required a SNR$\geq$10 for Q1-6, which corresponds to SNR$\geq$11.5 for Q1-8 by assuming that SNR roughly scales as $\sqrt{N}$, where N is the number of observed transits. This scaling is performed because the SNRs of observed KOIs have been reported for Q1-8, not Q1-6, in Batalha et al. (2012). To investigate incompleteness issues, we have also repeated all analyses in this paper for SNR cuts of 15, 20, and 25.

Now we discuss how we calculated detection efficiencies, and how they were used to debias this filtered sample of planetary candidates. Following the formalism of Youdin (2011), for any given planet the net detection efficiency η is the product of (1) the geometrical selection effect $\eta_{\rm geom}$ and (2) the *Kepler* photometric selection effect $\eta_{\rm phot}$. The geometrical selection effect is due to the probability of transit as planets with longer periods or larger semi-major axes will have a lower probability of crossing in front of the disk of the star as seen from *Kepler*, and is calculated as $\eta_{\rm geom} = R_*/a$, where a is semi-major axis. The *Kepler* photometric selection effect is due to the photometric quality of the star for detecting planets with specified radius and period. Consequently, $\eta_{\rm phot}$ is a function of both planetary radius and period. For a planet with radius R and period P, we calculated $\eta_{\rm phot}$ as the fraction of stars that can detect such a planet with SNR$\geq$10 (see Section 3.1), based on the KIC sample obtained in the previous section. Lastly, we calculated the net detection efficiency as $\eta = \eta_{\rm geom}\eta_{\rm phot}$.

We applied the above methods for obtaining detection efficiencies to our KOI subset of observed planetary candidates. For each candidate planet (or detection) in our KOI subset, we calculated its net efficiency η given its observed period P and radius R. Since η is the ratio of the number of detectable events to the number of actual planets, the inverse of η is equal to an estimate of the actual number of planets represented by each detection. After we calculated the value of $1/\eta$ for each detection in our KOI subset, we created debiased, binned histograms for P and R representing an estimate of the actual number of planets per P or R bin. The normalized versions of these histograms are given in Figure 1. We used these discrete distributions representing debiased planet periods and radii in order to randomly select values for each simulated planet's period and radius.

Our methods of obtaining photometric detection efficiencies (η_{phot}) are the same as the methods described in Howard et al. (2012) used to obtain binned (in P and R) efficiencies that were later analytically fit by Youdin (2011), except for the following differences. First, we applied these methods to Q1-6 data (previous work used Q2 only). Second, we avoided any loss of information that can occur during the binning process and/or the power law fitting process by skipping those steps and directly calculating the detection efficiency for each individual KOI candidate in our filtered sample. Third, we calculated SNR differently by actually using each KIC star's observing history during Q1-6 (e.g., not all stars are observed each quarter) as well as some other minor differences; our methods for calculating SNR are detailed in Section 3.1.

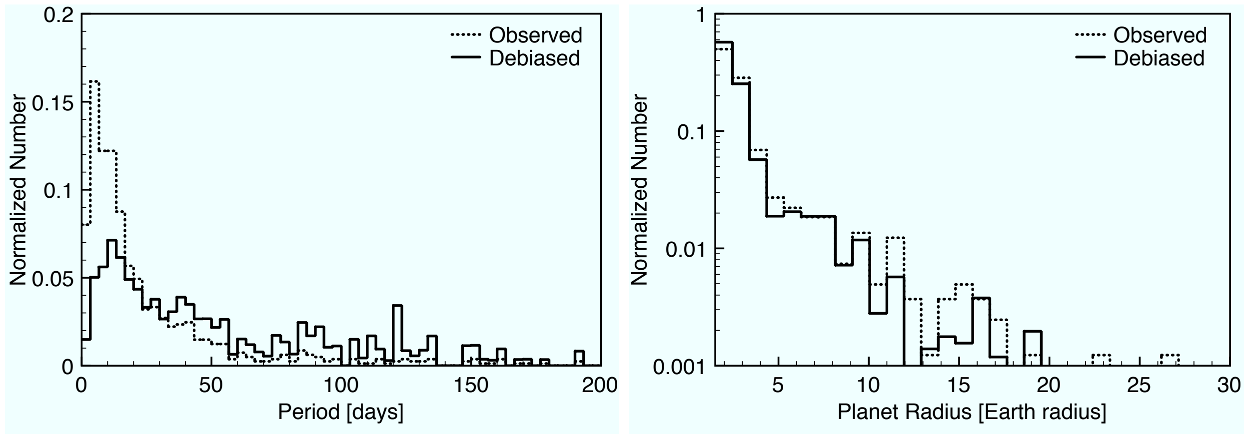

Fig. 1.— Observed and debiased distributions of orbital periods and radii for a subset (Equation (2)) of the planets detected by *Kepler*. The *top* plot for orbital period shows a distribution for 0−200 days divided into 60 equal-sized bins. The observed distribution shows increasing planet frequency at shorter periods, mainly due to the greater geometric probability of observing transiting planets at shorter periods. The *bottom* plot for planet radius shows a distribution for 1.5−30 $R_\oplus$ divided into 30 equal-sized bins.

2.3. Planet Multiplicity Distribution

We chose to represent the multiplicity distribution of simulated planetary systems–the distribution of the number of planets per star–by either a delta-like distribution, a modified Poisson distribution, or a bounded uniform distribution. All distributions are described by a single parameter. We did not consider other distributions such as an exponential distribution, which may result in a bad fit to the data (Lissauer et al. 2011b). All stars in our model populations are assumed to have at least 1 planet, and so our study cannot directly address the question of planet occurrence.

A delta-like distribution is a discrete distribution described by a single parameter D. If the parameter D represents an integer value, than all planetary systems following this distribution will have D planets each. If the parameter D does not represent an integer value, then each planetary system can have either $\lfloor \mathrm{D} \rfloor$ (floor function) or $\lceil \mathrm{D} \rceil$ (ceiling function) planets. For instance, a model population with $D = 3$ means that all of its planetary systems have 3 planets per star, and a model population with $D = 4.75$ means that 25% of its planetary systems have 4 planets and 75% of its planetary systems have 5 planets. As a result, D also represents the mean number of planets per system. This is the same as the "uniform" distribution used by Lissauer et al. (2011b).

A modified Poisson distribution described by parameter λ is a discrete distribution that is equivalent to a regular Poisson distribution with mean value λ, except that we ignore zero values. Therefore, by using a modified Poisson distribution we restrict the regular Poisson distribution so that values picked from the distribution must be greater than 0 (so that each planetary system must have at least 1 planet). As a result, the modified Poisson distribution is not strictly Poisson since its mean value is different from λ, hence the name "modified Poisson." Mathematically, the regular Poisson distribution can be written as

$$\mathrm{P}(k) = \frac{\lambda^k e^{-\lambda}}{k!}, \tag{3}$$

which gives the probability of obtaining a discrete value k from such a distribution.

A bounded uniform distribution is represented by a single parameter λ. For each planetary system, first a modified Poisson distribution (as defined above) with parameter λ is used to draw a value $N_{\max}$ (maximum number of planets). Second, a discrete uniform distribution with range $1{-}N_{\max}$ is used to draw a value representing the number of planets in that system.

We varied the values of the parameter D for the delta-like distribution and the values of the parameter λ for the modified Poisson and bounded uniform distributions. In total, we explored $D = 2 - 7$ and $\lambda = 1 - 6$, each with intervals of 0.25, resulting in a total of 63 possibilities for the multiplicity distribution.

2.4. Planet Inclination Distribution

We chose the inclination distribution in each planetary system to be one of three possibilities: an aligned inclination distribution, a Rayleigh distribution, or a Rayleigh of Rayleigh distribution, as also used by Lissauer et al. (2011b).

An aligned distribution is the straightforward case where relative inclinations in the system are 0°. This is the same as a perfectly coplanar system.

A Rayleigh distribution is a continuous distribution described by a single parameter σ, which determines the mean and variance of the distribution. Its mathematical form is

$$\mathrm{P}(k) = \frac{k}{\sigma^2} e^{-k^2/2\sigma^2}, \tag{4}$$

which gives the probability density function for a value k from this distribution.

A Rayleigh of Rayleigh distribution, with a single parameter σ_σ, means that we draw from two Rayleigh distributions for each planetary system. First, the given parameter σ_σ defines the first Rayleigh distribution from which we draw a value for σ for each planetary system. Second, the drawn value of σ is then used to define the second Rayleigh distribution from which we draw values for the inclinations of planets in that system. This allows for the possibility that planetary systems in a particular model population have Rayleigh inclination distributions with different mean and variance.

We varied σ for the Rayleigh distribution and σ_σ for the Rayleigh of Rayleigh distribution with the same range of values: $1-10°$ with intervals of 1°, as well as values of 15°, 20°, and 30°. In total, all possibilities for the 3 inclination distributions added up to a total of 27 possible inclination distributions.

2.5. Other Planetary Parameters

So far we have defined the distributions used in drawing the orbital periods, radii, multiplicity, and orbital inclinations of simulated planetary systems. Now we discuss all other relevant planetary parameters: planet mass, orbital semi-major axis, eccentricity, and longitude of the ascending node.

To determine planet mass M, we require an $M(R)$ relation to convert from radius to mass. First, we used $(M/M_{\oplus}) = (R/R_{\oplus})^{2.06}$, which is a commonly-used power law derived by fitting to Earth and Saturn (Lissauer et al. 2011b). Results given in this paper are based on this relation. Second, we obtained an alternate $M(R)$ relation by fitting to masses and radii of known transiting exoplanets. This $M(R)$ relation is a broken log-linear fit given as

$$\log_{10}\left(\frac{M}{M_{\rm Jup}}\right) = 2.368\left(\frac{R}{R_{\rm Jup}}\right) - 2.261 \quad \text{for} \left(\frac{R}{R_{\rm Jup}}\right) < 1.062, \tag{5}$$

$$\log_{10}\left(\frac{M}{M_{\rm Jup}}\right) = -0.492\left(\frac{R}{R_{\rm Jup}}\right) + 0.777 \quad \text{for} \left(\frac{R}{R_{\rm Jup}}\right) \geq 1.062. \tag{6}$$

This fit is plotted in Figure 2, along with data of known transiting exoplanets, the $(M/M_{\oplus}) = (R/R_{\oplus})^{2.06}$ relation by Lissauer et al. (2011b), and a $R(M)$ log-quadratic fit by Tremaine & Dong (2012). Our 4-parameter fit is a better match to the data than the 1-parameter prescription of $(M/M_{\oplus}) = (R/R_{\oplus})^{2.06}$ (improvement in χ^2 from 48.1 to 28.8), and this is not simply due to the addition of model parameters (F-test at 99.96% confidence level).

In contrast to the fit by Tremaine & Dong (2012), our fit is an $M(R)$ function and not a $R(M)$ function and hence is useful for cases that require assigning masses corresponding to particular radii (i.e., our fit does not have an ambiguity where some values of R have multiple corresponding values of M, which makes it impossible to select a unique mass for a given radius). In addition, our fit covers the full range of parameter space in radii; the fit by

Tremaine & Dong (2012) has a maximum radius value of about 1.3 Jupiter radii. We have repeated the analysis described in this paper using our fitted $M(R)$ relation in Equations (5)-(6), and we find essentially the same results as when we used $(M/M_{\oplus}) = (R/R_{\oplus})^{2.06}$.

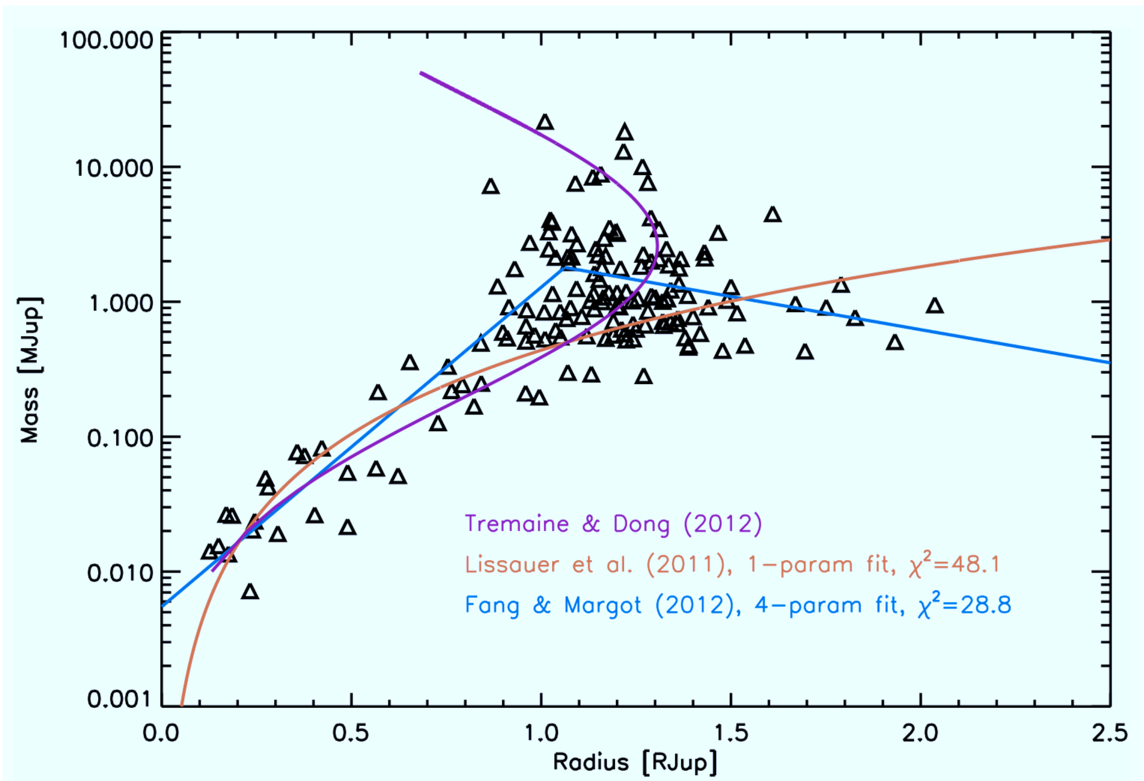

Fig. 2.— Known transiting planets (triangles) and three different mass-radius relations (colored curves). See Section 2.5 for details.

Each planet's semi-major axis is determined using the orbital period and Kepler's Third Law. For eccentricity, we assumed that all planets have circular orbits. *Kepler* candidates do not show evidence for large eccentricities (Moorhead et al. 2011), but we note that even moderate eccentricities (<0.25) could affect transit durations in a manner similar to that caused by differences in inclinations of up to a few degrees. For the longitude of the ascending node of each planet's orbit, we drew an angle from a uniform distribution with values between 0° and 360°.

Now we have described all relevant stellar and planetary parameters to build a fictitious planetary system. In the next subsection, we describe stability constraints placed on these systems.

2.6. Stability Requirements

The first stability constraint is Hill stability, and we describe our implementation using the following example. In the construction of each planetary system, we add a first planet with its parameters chosen according to the methods already described. If the system's assigned multiplicity is greater than one, we add a second planet. The second planet is accepted only if it is Hill stable with the first planet, which occurs when

$$\Delta = \frac{a_2 - a_1}{R_{H1,2}} \gtrsim 3.46, \tag{7}$$

where a is the semi-major axis and $R_{H1,2}$ is the mutual Hill radius defined as

$$R_{H1,2} = \left(\frac{M_1 + M_2}{3M_*}\right)^{1/3} \frac{a_1 + a_2}{2}, \tag{8}$$

(e.g., Gladman 1993; Chambers et al. 1996). Here, M represents mass and subscripts 1 and 2 denote the inner and outer planets, respectively. If the second planet is not accepted because it violates Hill stability with the first planet, then the second planet has its radius and orbital period (or equivalently, mass and semi-major axis) re-drawn until Hill stability is satisfied. We require that all adjacent planet pairs satisfy this Hill stability requirement. The assumption that adjacent planet pairs should be Hill stable is reasonable; out of the 885 planet candidates located in multi-planet systems detected during Q1-6 of the *Kepler* mission, only two pairs of planets are found to be apparently unstable by Fabrycky et al. (2012) on the basis of numerical integrations using nominal mass-radius scalings and circular orbit assumptions.

Following the methods of Lissauer et al. (2011b), we imposed a second stability constraint that any adjacent planet trio (any three neighboring planets) must satisfy

$$\Delta_{\text{inner pair of trio}} + \Delta_{\text{outer pair of trio}} \geq 18. \tag{9}$$

As described for the example above for Hill stability cases, if the constraint in Equation (9) is not satisfied, a planet's properties are re-drawn until this stability requirement is fulfilled.

For the creation of multi-planet systems, we added planets to each system one at a time, where successful addition of a planet occurred when it fulfilled both stability criteria described above. For systems with a large multiplicity, at times it was not possible to satisfy stability constraints given our period range and therefore we allowed a maximum of 1000 attempts per star before discarding it. Therefore, in rare cases, some model populations have a slightly lower number of planetary systems.

2.7. Summary

To summarize this section: we have described the steps taken to assemble various model populations, each consisting of about 10^6 planetary systems. Each of these model populations follows different combinations of (1) multiplicity and (2) inclination distributions. Taking all combinations of the values for the tunable parameters in these distributions, there are a total of 1,701 possibilities. Our goal is to take these model populations, run them through synthetic observations, and see which planets are transiting and detectable. The properties of these detectable planets will then be compared to the actual observed *Kepler* planets to determine which model produces acceptable fits. This allows us to determine the nature of underlying multiplicities and inclinations. In the next section, we discuss how we evaluate these model populations.

3. Evaluating Model Populations

We describe our methods for evaluating each model population: (1) determining detectable, transiting planets, and (2) comparing them to the observed *Kepler* planets using statistical tests.

3.1. Determining Detectable, Transiting Planets

For each model population, we determined which of the planets in each planetary system were *transiting*. From the group of transiting planets, we determined which transiting planets were *detectable* based on SNR requirements. The following paragraphs describe these methods.

For each planetary system, we evaluated whether any of the planets were transiting. First we picked a random line-of-sight (i.e., picking a random point on the celestial sphere) from the observer to the system, and the plane normal to this line-of-sight vector determines the plane of sky. We then computed the planet-star distance projected on the plane of sky (e.g., see Winn 2010). The minimum in that quantity is the *impact parameter*, which we normalized by the stellar radius. A planet transits when its impact parameter is less than 1.

We calculated the SNR of transit events in order to determine whether or not each transiting planet would have been detectable during Q1-6 of the *Kepler* mission. To do so, first we randomly picked a MJD (Modified Julian Date) between the first and last cadence mid-times of Q1-6 by using the dates provided in the *Kepler* Data Release Notes[2] (DRN) 14 and 16. We assumed that the planet transited on this randomly-picked date, and we explored backwards and forwards in time using the planet's orbital period in order to determine the dates of all transits during Q1-6. Next, we eliminated any transits that occurred in the gaps between quarters; such gaps are necessary to roll the spacecraft 90° to keep its solar arrays

[2]The DRN are available for download from MAST at http://archive.stsci.edu/kepler/data_release.html.

illuminated. In addition, not all stars are observed each quarter, for instance, due to CCD module failure. As a result, we used the planet's host star observing log that recorded all observed quarters (see Section 2.1), and eliminated any transits that occurred in quarters where the host star was not observed. Next, we eliminated a small fraction of remaining transits in a random fashion to account for a 95% duty cycle because of observing downtimes (e.g., breaks for data downlink). After accounting for these issues, all remaining N transits for this planet were then counted and used to calculate the detection SNR as

$$\mathrm{SNR} = \left(\frac{R}{R_*}\right)^2 \frac{\sqrt{N}}{\sigma_{\mathrm{CDPP}}}, \tag{10}$$

where the first fraction represents the depth of the transit and σ_{CDPP} represents an adimensional noise metric (quadratically interpolated to the transit duration length using the set of measured {3-hr, 6-hr, 12-hr} CDPP values) for the planet's host star (see Section 2.1). If the SNR is at least the value of the SNR threshold for detection (SNR$\geq$10), then the transiting planet is labeled as detectable.

3.2. Comparing to Observations

Here we describe how we evaluated each model population's goodness-of-fit when compared to observations. All model populations are distinct from each other due to the different parameter values chosen for their underlying multiplicity and inclination distributions. To evaluate how well each model population matches the observations, we compared them using 2 observables: (1) observed multiplicity vector and (2) observed distribution of normalized, transit duration ratios. These observables were computed for both the simulated planets and the KOI candidates.

We discuss these 2 types of observables in greater detail. The multiplicity vector $\boldsymbol{\mu}$ represents the number of systems observed with j transiting planets, where $j = 1, 2, 3, 4, 5, 6, 7+$. In other words, the multiplicity vector describes how many systems are observed to have a single planet, how many systems are observed with 2 planets, etc. Systems with 7 or more planets are placed in the same multiplicity category: $j = 7+$. The normalized, transit duration ratio ξ is defined as (e.g., Fabrycky et al. 2012)

$$\xi = \frac{T_{\mathrm{dur},1}/P_1^{1/3}}{T_{\mathrm{dur},2}/P_2^{1/3}}, \tag{11}$$

where the transit duration T_{dur} is normalized by the orbital period raised to the 1/3 power $P^{1/3}$. Subscripts 1 and 2 represent any pair of planets in the same system where 1 denotes the inner planet and 2 denotes the outer planet. A $j-$planet system has a total of $j(j-1)/2$ pairs. We decided to fit to values of ξ because they contain information on mutual inclinations of observed multi-planet systems. For instance, coplanar systems tend to have values of $\xi > 1$, because the inner planet's impact parameter is smaller and hence its normalized transit duration is longer. Fabrycky et al. (2012) used the observed *Kepler* distribution of ξ to determine that the observed mutual inclinations are low at 1.0-2.3°.

We calculated the ($\boldsymbol{\mu}$, ξ) observables for the subset of KOIs previously obtained in Section 2.2. We also calculated the ($\boldsymbol{\mu}$, ξ) observables for each model population by considering all detectable, transiting planets.

Our next step was to obtain a statistical measure of each model population's goodness-of-fit to the observed population by calculating a test statistic and its corresponding probability. A larger probability indicates a better match to observations. To compare multiplicity vectors $\boldsymbol{\mu}$, we performed chi-square tests, which are appropriate for discrete data. Chi-square tests are valid when the chi-square probability distribution is a good approximation to the distribution of the chi-square statistic (Equation (12)). As shown by theoretical investigations, the approximation is usually good when there are at least 5 discrete categories and at least 5 values in each category for the model population's $\boldsymbol{\mu}$ (e.g., Hoel 1984). These requirements may not always be satisfied in our case, and so we also perform a randomization method to calculate chi-square probabilities, as described below. To compare ξ distributions, we performed Kolmogorov-Smirnov (K-S) tests, which can be used for continuous data. K-S tests have no restrictions on sample sizes, and are also distribution-free and so therefore can be applied for any kind of underlying distribution of the comparison samples (e.g., Stuart & Ord 1991). These tests are described in more detail below.

The chi-square test used for comparing multiplicity vectors uses a chi-square statistic χ^2 computed as (e.g., Press et al. 1992)

$$\chi^2 = \sum_j \frac{(O_j - E_j)^2}{E_j}, \tag{12}$$

where O_j represents an observed quantity, in this case the number of observed planetary systems with j planets, E_j represents an expected or theoretical value, in this case the number of simulated planetary systems with j detectable planets, and j represents the index of the multiplicity vector (i.e., 1 for 1-planet systems, N for N-planet systems, etc.) being summed over. Scaling was performed to adjust the model multiplicity vector such that $\sum O_j = \sum E_j$. Large values of χ^2 represent worse fits and larger deviations between O_j and E_j quantities, meaning it is not likely the O_j values are drawn from the population represented by the E_j values. For comparison between each model population's expected values and observed values, we only considered j indices where $E_j \neq 0$ (noting the appearance of E_j in the denominator of Equation (12)). Since we must ignore categories with $E_j = 0$, we note that there may be cases (i.e., for the delta-like multiplicity distribution) where a given model population with only 1-planet and 2-planet systems may yield a low χ^2 even though it is in fact *not* a good match to the data, e.g., because it does not predict any 3+ planet systems that are actually observed. Model populations based on delta-like multiplicity distributions do not provide a good match to the data (Section 4). Consequently, we will not consider them further and none of the χ^2 probabilities presented in this paper suffer from this issue.

We computed two chi-square probabilities for each calculation of the statistic in Equation (12). First, the standard chi-square probability is an incomplete gamma function that can be computed with knowledge of χ^2 and the number of degrees of freedom. For our case, the number of degrees of freedom is equal to the number of indices with $E_j \neq 0$ subtracted by 1 (to account for the scaling constraint). This standard probability function is a good approximation as long as the number of bins or the number of values in each bin is large. Given that some higher-j categories in our multiplicity vector may have low numbers, we performed a second calculation of the chi-square probability using a more robust randomization method (e.g., Good 2006). In this method, we determined how often we could pick a new distribution from the model distribution with $\chi^2_{\rm new,model}$ (comparing new and model distributions) that was worse than the $\chi^2_{\rm obs,model}$ (comparing observed and model distributions). In practice, we randomly picked 10,000 times per model population and the fraction of them that yielded $\chi^2_{\rm new,model} > \chi^2_{\rm obs,model}$ represented the chi-square probability. We found that in most cases, there was reasonable agreement between the chi-square probabilities from the standard function and from the randomization method. The chi-square probabilities quoted later in this paper are those obtained from the randomization method.

For the K-S test used for comparing ξ distributions, we calculated the K-S statistic and the standard K-S probability (e.g., Press et al. 1992). The K-S statistic D is the maximum difference of the absolute value of two distributions given as cumulative distribution functions, or

$$D = \max|O_{N_1}(\xi) - E_{N_2}(\xi)|, \tag{13}$$

where $O_{N_1}(\xi)$ represents the observed cumulative distribution function of ξ values, $E_{N_2}(\xi)$ represents the expected or model cumulative distribution function, and N_1 and N_2 is the number of ξ values for the observed and expected distributions, respectively. The significance or probability of D represents the chance of obtaining a higher value of D, and can be calculated with knowledge of D and the number of points N_1 and N_2. This test is valid even with an unequal number of points, i.e., $N_1 \neq N_2$. We note that N_2 can vary significantly between model populations and this can affect the reliability of the calculated probability, such as when comparing a probability obtained from one model population to the probability obtained from another model. This is most pertinent for cases with large differences in N_2 (i.e., between model populations with small and large multiplicities), where a poor fit is harder to discern when there are fewer model values N_2 to compare to observed values. This issue can manifest itself as outliers in our results for model populations with fewer number of planets per system. As we will show, we do not find any evidence of such outliers in our results.

In the next section, we describe our calculations of these probabilities to evaluate the match between each model population and the data.

4. Results

In this section, we present the results for the fit between each model population and the KOI subset that obeys Equations (1) and (2), and these results are illustrated in Figures 3−5. We do not show any results incorporating the delta-like multiplicity distribution because it does not provide a good match to the data. We will describe each of these figures in turn.

Figure 3 shows the probabilities resulting from the χ^2 test that compared the observed and model multiplicity vectors (number of 1-planet systems, number of 2-planet systems, etc.). Most models can be ruled out with 3−sigma confidence, and these tend to be systems with many planets and low inclinations or systems with few planets and high inclinations. On the other hand, models that are consistent with the data include systems of few planets with low inclinations or systems of many planets with high inclinations; this degeneracy is evident in the upward slopes in Figure 3. This degeneracy or upward trend is seen because the intrinsic populations corresponding to the observed transits can take a variety of forms: from few planets that are well-aligned to many planets with larger inclinations. The degeneracy exists because systems with many planets and large inclinations are detected by transit surveys as systems with few planets and small inclinations. Models with a bounded uniform multiplicity distribution and a Rayleigh of Rayleigh inclination distribution appear to provide a better fit (higher χ^2 probabilities) than other models.

Figure 4 depicts the probabilities from the K-S test that evaluated the fit between the observed and model ξ (Equation (11)) distributions of multi-planet systems. The distribution of ξ values is used to gauge the extent of coplanarity or non-coplanarity in multi-planet systems. This diagram shows that higher probabilities are obtained for models with low-inclination distributions. Nearly all models with a Rayleigh σ or Rayleigh of Rayleigh σ_σ parameter greater than $3°$ can be ruled out with $3-$sigma confidence. None of the models with perfectly aligned (coplanar) systems provide acceptable fits. The best fits with highest probabilities are Rayleigh or Rayleigh of Rayleigh inclination distributions with $\sigma, \sigma_\sigma = 1°$. The probabilities in this figure appear to be relatively independent of the underlying multiplicity distribution (evident in the long vertical columns of blue colors), because the ξ distribution probes the relative inclination between any pair of planets in a system and is independent of the multiplicity or number of planets. As a result, we find that the K-S test is not very sensitive to the underlying multiplicity model. Comparison between Figures 3 and 4 shows that the degeneracy evident in Figure 3 is broken when considering Figure 4 as well–by also examining Figure 4, we see that only systems with fewer planets and lower inclinations are consistent with the data.

Figure 5 illustrates the combined probabilities from Figures 3 and 4. The combined probability is the product of the χ^2 and K-S probabilities. We make the assumption that these two probabilities are independent. This product of two probabilities is shown in Figure 5, from which it is evident that most models can be ruled out as unacceptable fits. Degeneracies present in both Figures 3 and 4 are broken when the data in these figures are combined in Figure 5. The best fits are models with lower inclinations and lower multiplicities, and in particular, the fits with a bounded uniform distribution in multiplicity and a Rayleigh or Rayleigh of Rayleigh distribution in inclination are most consistent with the data.

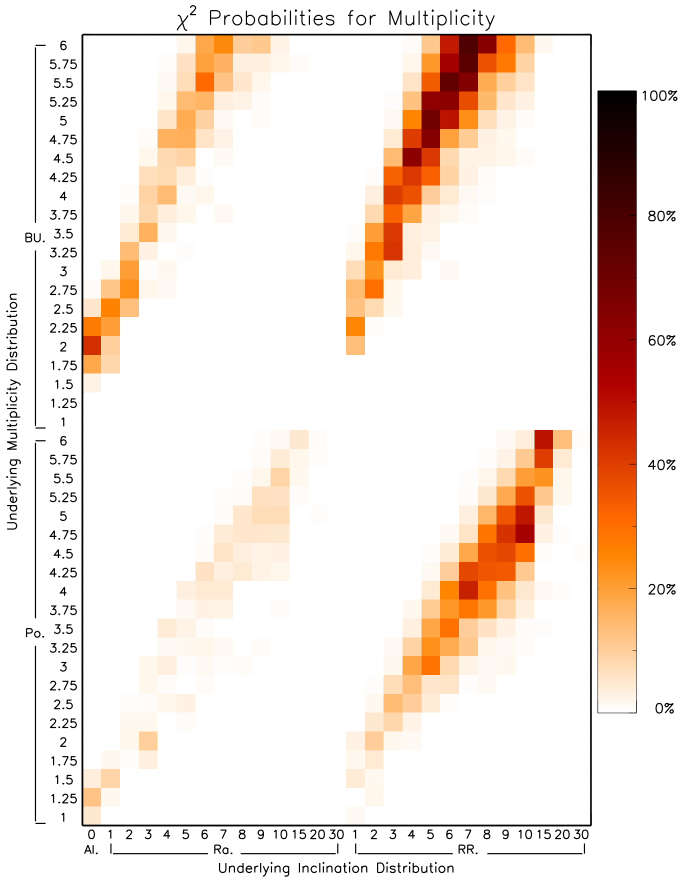

Fig. 3.— Diagram showing probabilities from χ^2 tests that evaluated the goodness-of-fit of various models with respect to planet multiplicity. Each square on this grid represents a different model, and each square's color depicts the probability (the higher the probability, the better the fit). The x-axis shows the *underlying inclination distribution*, and can be aligned (Al.), Rayleigh (Ra.), or Rayleigh of Rayleigh (RR.). For Al., the number given is the inclination, or 0°. For Ra. and RR., the numbers indicate the σ or σ_σ parameter (in degrees) for the distribution. The y-axis shows the *underlying multiplicity distribution*, and can be modified Poisson (Po.) or bounded uniform (BU.). For Po, the number given is λ of the Poisson distribution and represents approximately the mean number of planets per system. For BU., the number given is λ of the Poisson distribution from which the maximum number of planets is drawn. This plot can be approximately divided into 4 quadrants, where in each quadrant the y-axis has the number of planets per system increasing to the top and the x-axis has inclinations increasing to the right.

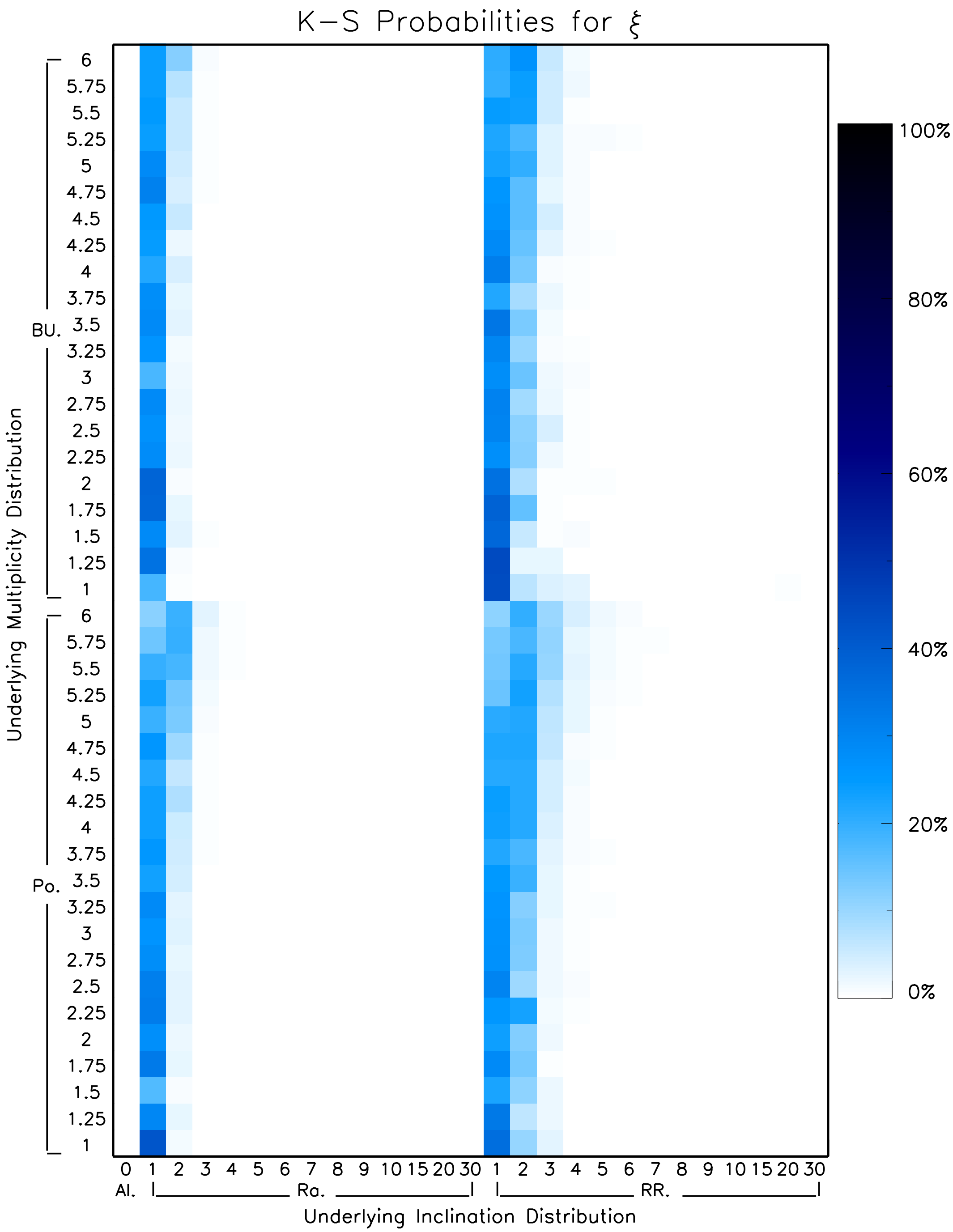

Fig. 4.— Same as Figure 3, except this diagram shows K-S probabilities of ξ distributions. These probabilities represent the goodness-of-fit of various models with respect to orbital inclinations.

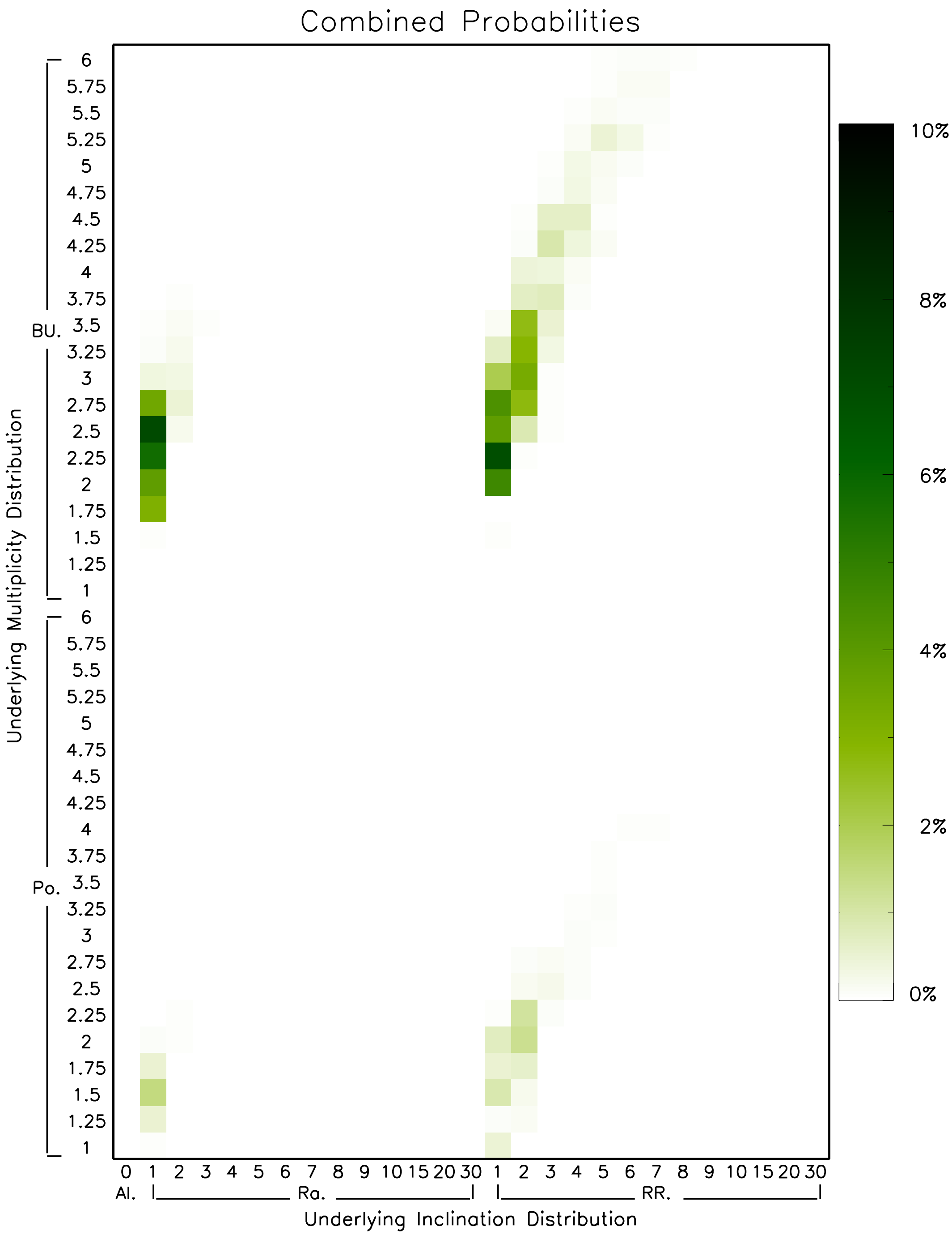

Fig. 5.— Same as Figure 3, except this diagram shows combined (multiplied) probabilities from χ^2 and K-S tests. These probabilities represent the overall goodness-of-fit of various models to the *Kepler* sample.

4.1. Overall Best-Fit Models: Few Planets and Low Inclinations

As seen in Figure 5, the overall best-fit models with the largest combined probabilities are models with low-multiplicity bound uniform distributions (represented by λ) and with low-inclination Rayleigh (represented by σ) or Rayleigh of Rayleigh (represented by σ_σ) distributions. The best-fit model with a bounded uniform and Rayleigh distribution has $\lambda = 2.50$ and $\sigma = 1°$. The best-fit model with a bounded uniform and Rayleigh of Rayleigh distribution has $\lambda = 2.25$ and $\sigma_\sigma = 1°$. There are no qualitative differences between the quality of these two fits. Based on these two best-fit models, we find that 75-80% of planetary systems have 1 or 2 planets with orbital periods less than 200 days. In addition, over 85% of planets have orbital inclinations less than 3 degrees (relative to a common reference plane). These results represent our best estimate of the underlying distributions of *Kepler* transiting systems for the parameter space explored here (Equations (1) and (2)). Assuming that the *Kepler* sample is representative, these distributions also describe the architecture of planetary systems in general.

We analyze the best-fit model with a bounded uniform ($\lambda = 2.25$) and a Rayleigh of Rayleigh ($\sigma_\sigma = 1°$) distribution in greater detail. First, in Figure 6 we plot the underlying multiplicity and inclination distributions. The first and second rows of the figure show the first and second steps of picking multiplicity and inclination values from the distributions. The plots in the bottom two rows show the resulting histograms of values picked from these distributions. Second, we show the comparisons between the best-fit model and the data. Table 1 compares the numbers of observed transiting systems to the numbers of detected transits from the best-fit model. There is a reasonable match in each multiplicity index and an overall match probability of 25.2%. Figure 7 illustrates the comparison between the distribution of ξ values from *Kepler* observations and the distribution of ξ values from simulated detections using the best-fit model. The numbers in each bin have been normalized to enable comparison, and the match between distributions has a probability of 27.5%. Taken together, the probabilities from each fitted observable (χ^2 probability for the multiplicity fit and K-S probability for the ξ distribution fit) are multiplied to yield a combined probability of 6.9%.

The low inclinations in our best-fit models have interesting implications for planet formation and evolution theories. Our findings that these systems are relatively coplanar (at least out to 200 days) are in favor of standard models that suggest planet formation within a protoplanetary disk. In addition, strong influences by external perturbers such as Kozai processes, scattering, or resonances are not likely to play a major, lasting role given that these systems do not generally have high, excited inclinations. Theories of planet formation and evolution can be tested against the architecture of planetary systems illuminated by the *Kepler* mission.

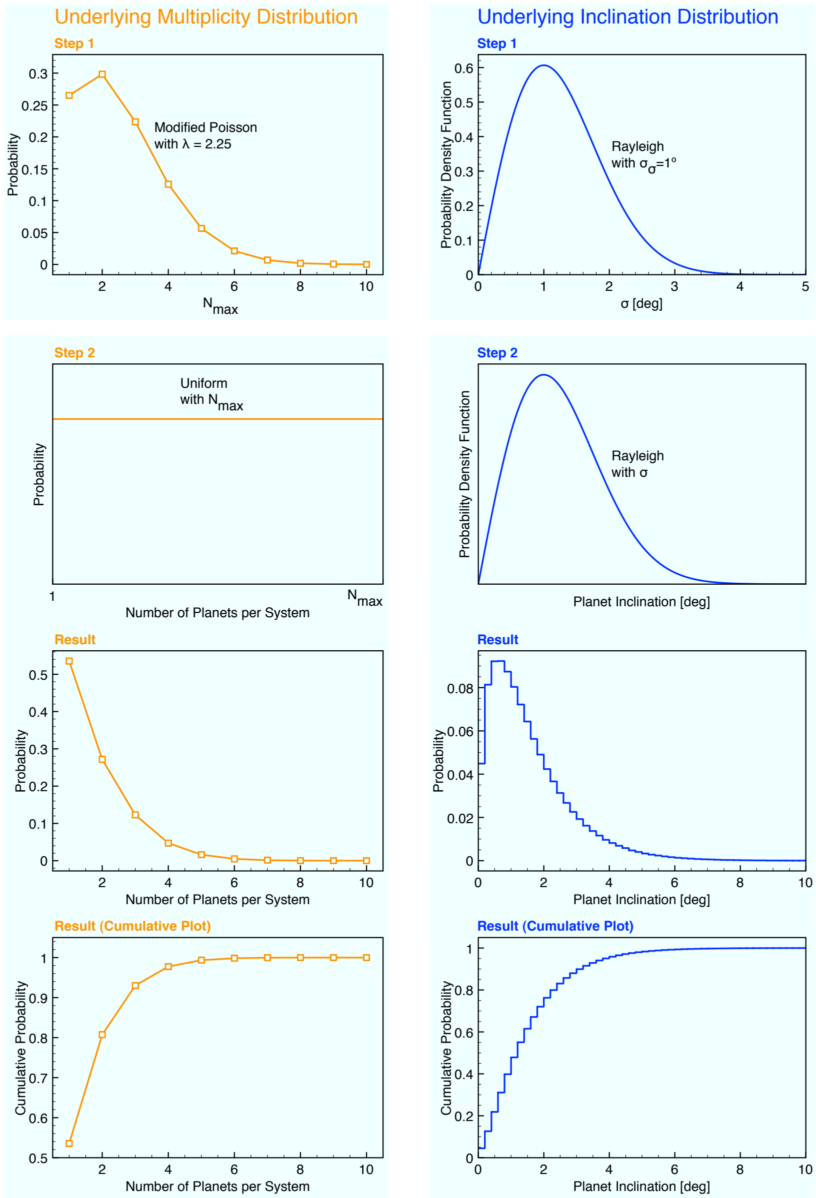

Fig. 6.— One of two best-fit models for multiplicity (*left column*) and inclination (*right column*). The multiplicity distribution is a bounded uniform distribution: for each planetary system (1) we draw a value $N_{\rm max}$ from a modified Poisson distribution with $\lambda = 2.25$, and (2) we choose the number of planets by uniformly picking a value between 1 and $N_{\rm max}$. The resulting distributions of multiplicities are shown in the bottom plots. The inclination distribution is a Rayleigh of Rayleigh distribution: (1) for each planetary system we draw a value for σ from a Rayleigh distribution with parameter $\sigma_\sigma = 1^\circ$, and (2) for each of its planets we draw a value for inclination from a Rayleigh distribution with parameter σ. The resulting distributions of inclinations are shown in the bottom plots.

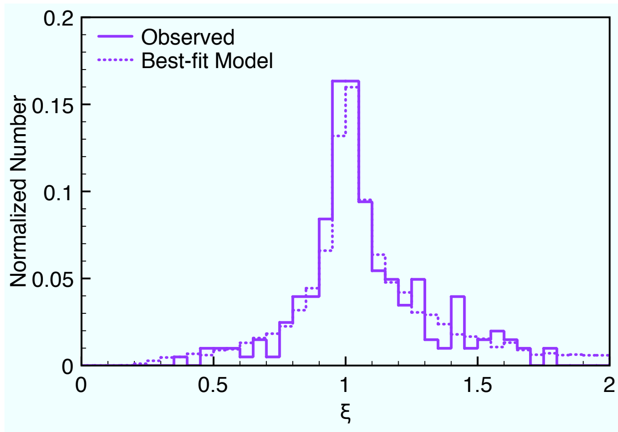

Fig. 7.— Comparison of the ξ distribution between observations and one of two best-fit models, here with $\lambda = 2.25$ and $\sigma_\sigma = 1^\circ$ (Section 4.1). The quantity ξ is sensitive to orbital inclinations in multi-planet transiting systems. The K-S probability for this match is 27.5%.

4.2. Effects of False Positives and Search Incompleteness

The results of our study do not take into account the existence of false positives that mimic real planet transit signals in the KOI dataset. For the *Kepler* sample released by Borucki et al. (2011b), Morton & Johnson (2011) estimated that false positive probabilities

Table 1: Multiplicity Vector:
Number of Systems with j Detectable Planets

Name	$j =$	1	2	3	4	5	6	7+
Observed		542	85	24	4	1	1	0
Best-fit		540.6	92.9	19.1	3.6	0.6	0.2	0.0

Comparison of the multiplicity vector between observations and one of two best-fit models, here with $\lambda = 2.25$ and $\sigma_\sigma = 1^\circ$ (see Section 4.1). The χ^2 probability for this match is 25.2%.

were generally low at $\lesssim 10\%$, and an analysis using binary statistics by Lissauer et al. (2012) estimated that $\sim$98% of the multi-planet systems are real. For the latest *Kepler* sample released by Batalha et al. (2012), Fabrycky et al. (2012) discussed how $\sim$96% of pairs in multi-transiting candidate systems are likely to be real planets using stability arguments. For the purposes of our study, we assumed that all planetary candidates are real. We expect that the existence of false positives can potentially affect the fit between multiplicity vectors (e.g., Table 1), particularly for the case of singly transiting systems where the actual population may actually have lower numbers than reported due to false positives. We do not expect that false positives will significantly influence the fit between normalized transit duration ratios (e.g., Figure 7) since such ratios are only computed for multi-planet systems, which we expect to be a higher-fidelity sample than singly transiting systems.

To determine the effect of false positives on our results, we repeated the entire analysis described in this paper for two cases. In the first case, we removed all false positives described in the literature (Howard et al. 2012; Batalha et al. 2012; Fabrycky et al. 2012; Santerne et al. 2012; Ofir & Dreizler 2012; Colón et al. 2012); a total of 35 false positives were removed from the KOI table. Since we base our debiased period and radius distributions on the observed sample, we created new model populations and repeated our analyses. In the second case, not only did we remove all known false positives but we also added simulated false positives to our artificial populations. For each population of planetary systems, we added enough false positives (all single-planet systems) such that false positives represented 10% of all planets. The properties of the simulated false positives (e.g., radius and period) were based on the properties of known false positives. We then repeated all of our analyses for these populations. In both cases, we found that our results of intrinsic distributions were almost identical in terms of the typical number of planets per system as well as their inclinations. Accordingly, we do not expect that the effect of false positives will appreciably change our results.

Another effect that can impact our results is *Kepler* search incompleteness. The *Kepler* team is currently investigating the completeness of the pipeline by inserting artificial transits into the pipeline and determining their recovery rates. Batalha et al. (2012) suggested that the KOI catalog released in 2011 by Borucki et al. (2011b) suffers from incompleteness issues because the planet gains seen between the 2011 and 2012 catalogs cannot be completely explained by the longer observation window, and that it is possible the 2012 catalog still suffers from some incompleteness issues. This can affect our results in terms of the comparison between the observations and our model's computed observables, and we expect that its impact is a function of SNR and other parameters. The impact of incompleteness will be better known after the *Kepler* team's detailed study of pipeline completeness is finished, and pipeline completeness is expected to improve in the future with pipeline upgrades that are already underway (Batalha et al. 2012).

To investigate the reliability of our results given incompleteness issues, we have repeated all simulations and analyses described in this paper for higher SNR thresholds of 15, 20, and 25. In all cases, we find that our conclusions regarding low intrinsic inclinations are the same and that the *Kepler* data favors low-inclination distributions. However, we find that the best-fit multiplicity distribution rises towards larger numbers of planets as we increase to higher SNR thresholds. This can be explained as follows. For a given population of planetary systems, by imposing higher and higher SNR thresholds on the detectability of its transiting planets, planets in two-planet systems are more likely to be missed than planets in one-planet systems. This is because the outer planet in two-planet systems tends to have a larger orbital period than the planet in one-planet systems, and therefore the outer planet in two-planet systems will exhibit fewer transits and have lower SNR. Consequently, the ratio of observed one-planet to two-planet systems should rise with higher SNR thresholds for detectability. This effect is seen in our synthetic populations, but is not seen in the observed *Kepler* data, where the ratio of observed one-planet to two-planet systems remains near 6:1 for SNR$\sim$10 to SNR$\sim$25 for the radius and period regime considered here. As a result, the best-fit multiplicity distribution rises with increasing SNR thresholds in order to match the data. This curious trend in the data suggests that perhaps there are many single-planet systems missing in the KOI table. If this is the case, then our multiplicity determinations serve as an upper limit regarding the typical number of planets per system. The best way to test this is to repeat this analysis in the future when the KOI tables are less biased and more complete.

5. Comparison With the Solar System and With Previous Work

We compare the results of our study with the properties of planets in the Solar System as well as with some relevant previous studies.

5.1. Results Are Consistent With the Solar System

Based on the underlying multiplicity distribution of our best-fit models, 75-80% of planetary systems have 1 or 2 planets with orbital periods less than 200 days (see Section 4.1). In comparison, the Solar System has 1 planet, Mercury, with an orbital period less than 200 days. Accordingly, our best-fit multiplicity distributions are consistent with the Solar System, if we extrapolate the results of our study to planetary radii less than 1.5 Earth radii. Note that our analysis is agnostic about the number of planets with larger orbital periods or different radius/mass regimes than considered here; recall that these limits are due to the parameter space constraints imposed by our study and defined in Equations (1) and (2). More data and extension of this study to longer orbital periods and smaller planetary radii are warranted before any definitive multiplicity comparison can be made with the Solar System.

Based on the underlying inclination distributions of our best-fit models, over 85% of planets have orbital inclinations less than 3 degrees (see Section 4.1), suggesting a high degree of coplanarity. This is compatible with the inclinations seen among the planets in the Solar System, if we allow ourselves to extrapolate beyond the period and radii limits of our study. In the Solar System, 7 out of the eight planets (or 87.5%) have inclinations less than 3 degrees relative to the invariable plane, with Mercury as the exception.

5.2. Comparison with Previous Studies

Lissauer et al. (2011b) investigated the dynamical properties of multi-planet systems in the KOI catalog announced by Borucki et al. (2011b). They also presented a detailed analysis of the inclinations of *Kepler* planetary systems. To accomplish this, they created a host of planetary models following different planet multiplicity and inclination distributions, determined which of those planets were transiting and detectable, and compared the resulting transit numbers with the observed transit numbers to determine each model's goodness-of-fit. Differences between their methods and ours include different methods for obtaining debiased period and radius distributions, different radius and period parameter ranges, an observed ξ distribution that was used as a fitted observable in our study, and different data sets (we used the most recently released KOI data set; Batalha et al. 2012). From their results, Lissauer et al. (2011b) ruled out systems with small numbers of planets and large inclinations as well as systems with large numbers of planets and small inclinations, which we also found to be inconsistent with the data (see Figure 3). In addition, they found a degeneracy in their results between underlying distributions of inclination and multiplicity; the number of planets per system could be increased if the inclination was also increased and still provide good fits to the data, also seen in our Figure 3. Ultimately they discounted the case of thick systems with many planets by invoking results from radial velocity surveys that suggested low inclinations (see discussion in Fabrycky et al. 2012). In our study, we were able to reject that scenario because it provided poor fits to the observed ξ distribution (see Figure 4).

Tremaine & Dong (2012) applied a general statistical model to *Kepler* data as well as to radial velocity surveys to analyze the multiplicity and inclination distributions. They concluded that *Kepler* data alone could not place constraints on inclinations, and acceptable possibilities ranged from thin to even spherical systems. Systems with large rms inclinations could be fit by the data as long as some of them had a large number of planets. However, when jointly analyzing both *Kepler* and radial velocity data, they were able to place constraints on inclinations to show that mean planetary inclinations are in the range $0 - 5°$. These relatively low inclinations are consistent with our results showing how models with lower inclinations provided better fits to the data.

Figueira et al. (2012) determined underlying inclination distributions by applying information from both HARPS (High Accuracy Radial Velocity Planet Searcher) and *Kepler* surveys. They assumed that if the HARPS and *Kepler* surveys share the same underlying population, then the different detection sensitivities of these two surveys with their detected samples of planets should allow determination of the underlying inclinations. To do so, they created synthetic populations of planets with a given multiplicity distribution as previously determined using HARPS data, and planets were given various inclination distributions (aligned, Rayleigh, and isotropic). Each model's goodness-of-fit was determined by comparing the frequency of transiting systems with the *Kepler* sample. They found that the best fits were obtained using models with inclinations prescribed by a Rayleigh distribution with $\sigma \leq 1°$. In our study, we used a different data set based on the latest release by Batalha et al. (2012), we fit for an additional parameter (the intrinsic multiplicity distribution), and we fit to an extra observable (the resulting ξ distribution). Given that, our overall results are in agreement since we also found that low inclinations with a Rayleigh parameter $\sigma \sim 1°$ are consistent with the data.

Fabrycky et al. (2012) presented important properties of multi-planet candidates in the KOI catalog released by Batalha et al. (2012). They found that almost all of these systems are apparently stable (using nominal mass-radius and circular orbit assumptions), which reinforces the high-fidelity nature of these multi-planet detections. In addition, they derived the mutual inclinations of observed planets using the distribution of ξ from the *Kepler* sample, which we used in our study as a fitted observable. They found that mutual inclinations are constrained to the range of $1-2.3°$ for observed planets, and concluded that planetary systems are typically flat. Our analysis is different and has some advantages in that we considered underlying planet multiplicity and inclination models, ran them through synthetic observations, and fitted the models' results to observed transit numbers and ξ distribution. Our study agrees with the conclusions of Fabrycky et al. (2012) that planetary systems tend to be relatively coplanar to within a few degrees.

Weissbein et al. (2012) implemented an analytical model and investigated an intrinsic Poisson distribution for planet multiplicity as well as coplanar and non-coplanar assumptions for inclinations using a Rayleigh distribution. They found that none of their choices for multiplicity and inclination distributions produced numbers of transiting planet systems matching the *Kepler* data. This is generally consistent with our results, where we find that combinations of Poisson multiplicity distributions and Rayleigh inclination distributions produce some of the poorest fits. They suggested that the disagreement between their results and the data could be potentially explained if planet occurrence is not an independent process and is instead correlated between planets in the same system, where the existence of one planet may affect the existence of additional planets.

Johansen et al. (2012) used a different approach than some previous authors. They created synthetic triple planet systems by assuming they could be based off of observed *Kepler* triply transiting systems. They determined which of their synthetic planets could be transiting and observable, and then calculated the resulting number of singly, doubly, and triply transiting systems to compare with the actual number of transits in the *Kepler* data. They also repeated these steps for different inclinations. From fitting to observed doubly and triply transiting systems, they found low mutual inclinations of $\lesssim 5°$. Although our methods are different, such low mutual inclinations are compatible with our findings that these systems are intrinsically thin. In addition, Johansen et al. (2012) found that numbers of transiting two-planet and three-planet systems can be matched by underlying three-planet systems, but they underproduced the number of transiting single-planet systems. To investigate this further, we have repeated our entire analysis by considering systems with only one or three planets. We find that we are not only able to reproduce the numbers of transiting two-planet and three-planet systems, as did Johansen et al. (2012), but also the number of single planet systems. Of course, by considering only systems with one and three planets we are not able to match the number of systems with four transiting planets or greater.

6. Conclusions

We have investigated the underlying distributions of multiplicity and inclination of planetary systems by using the sample of planet candidates discovered by the *Kepler* mission during Quarters 1 through 6. Our study included solar-like stars and planets with orbital periods less than 200 days and with radii of $1.5-30$ $R_\oplus$. We created model populations represented by a total of two tunable parameters, and we fitted these models to observed numbers of transiting systems and to normalized transit duration ratios. We did not include any constraints from radial velocity surveys. Below we list the main conclusions of our study.

1. From our best-fit models, 75-80% of planetary systems have 1 or 2 planets with orbital periods less than 200 days. This represents the unbiased, underlying number of planets per system.

2. From our best-fit models, over 85% of planets have orbital inclinations less than 3 degrees (relative to a common reference plane), implying a high degree of coplanarity.

3. Compared to previous work, our results do not suffer from degeneracies between multiplicity and inclination. We break the degeneracy by jointly considering two types of observables that contain information on both number of planets and inclinations.

4. If we extrapolate down to planet radii less than 1.5 Earth radii, the underlying

multiplicity distribution is consistent with the number of planets in the Solar System with orbital periods less than 200 days. If we also extrapolate to beyond 200 days, we find that the underlying distribution of inclinations derived here is compatible with inclinations in the Solar System.

5. Our results are also consistent with the standard model of planet formation in a disk, followed by an evolution that did not have a significant and lasting impact on orbital inclinations.

Continued observations by the *Kepler* mission will improve the detectability of new candidate planets covering a larger swath of parameter space, especially to longer orbital periods and smaller planetary radii. We anticipate that future statistical work will further boost our understanding of the underlying architecture of planetary systems.

REFERENCES

Baluev, R. V. 2011, Celestial Mechanics and Dynamical Astronomy, 111, 235

Batalha, N. M., Borucki, W. J., Bryson, S. T., Buchhave, L. A., Caldwell, D. A., Christensen-Dalsgaard, J., Ciardi, D., Dunham, E. W., Fressin, F., Gautier, III, T. N., Gilliland, R. L., Haas, M. R., Howell, S. B., Jenkins, J. M., Kjeldsen, H., Koch, D. G., Latham, D. W., Lissauer, J. J., Marcy, G. W., Rowe, J. F., Sasselov, D. D., Seager, S., Steffen, J. H., Torres, G., Basri, G. S., Brown, T. M., Charbonneau, D., Christiansen, J., Clarke, B., Cochran, W. D., Dupree, A., Fabrycky, D. C., Fischer, D., Ford, E. B., Fortney, J., Girouard, F. R., Holman, M. J., Johnson, J., Isaacson, H., Klaus, T. C., Machalek, P., Moorehead, A. V., Morehead, R. C., Ragozzine, D., Tenenbaum, P., Twicken, J., Quinn, S., VanCleve, J., Walkowicz, L. M., Welsh, W. F., Devore, E., & Gould, A. 2011, ApJ, 729, 27

Batalha, N. M., Rowe, J. F., Bryson, S. T., Barclay, T., Burke, C. J., Caldwell, D. A., Christiansen, J. L., Mullally, F., Thompson, S. E., Brown, T. M., Dupree, A. K., Fabrycky, D. C., Ford, E. B., Fortney, J. J., Gilliland, R. L., Isaacson, H., Latham, D. W., Marcy, G. W., Quinn, S., Ragozzine, D., Shporer, A., Borucki, W. J., Ciardi, D. R., Gautier, III, T. N., Haas, M. R., Jenkins, J. M., Koch, D. G., Lissauer, J. J., Rapin, W., Basri, G. S., Boss, A. P., Buchhave, L. A., Charbonneau, D., Christensen-Dalsgaard, J., Clarke, B. D., Cochran, W. D., Demory, B.-O., Devore, E., Esquerdo, G. A., Everett, M., Fressin, F., Geary, J. C., Girouard, F. R., Gould, A., Hall, J. R., Holman, M. J., Howard, A. W., Howell, S. B., Ibrahim, K. A., Kinemuchi, K., Kjeldsen, H., Klaus, T. C., Li, J., Lucas, P. W., Morris, R. L., Prsa, A., Quintana, E., Sanderfer, D. T., Sasselov, D., Seader, S. E., Smith, J. C., Steffen, J. H., Still, M., Stumpe, M. C., Tarter, J. C., Tenenbaum, P., Torres, G., Twicken, J. D., Uddin, K., Van Cleve, J., Walkowicz, L., & Welsh, W. F. 2012, ArXiv e-prints

Bean, J. L. & Seifahrt, A. 2009, A&A, 496, 249

Borucki, W. J., Koch, D. G., Basri, G., Batalha, N., Boss, A., Brown, T. M., Caldwell, D., Christensen-Dalsgaard, J., Cochran, W. D., DeVore, E., Dunham, E. W., Dupree, A. K., Gautier, III, T. N., Geary, J. C., Gilliland, R., Gould, A., Howell, S. B., Jenkins, J. M., Kjeldsen, H., Latham, D. W., Lissauer, J. J., Marcy, G. W., Monet, D. G., Sasselov, D., Tarter, J., Charbonneau, D., Doyle, L., Ford, E. B., Fortney, J., Holman, M. J., Seager, S., Steffen, J. H., Welsh, W. F., Allen, C., Bryson, S. T., Buchhave, L., Chandrasekaran, H., Christiansen, J. L., Ciardi, D., Clarke, B. D., Dotson, J. L., Endl, M., Fischer, D., Fressin, F., Haas, M., Horch, E., Howard, A., Isaacson, H., Kolodziejczak, J., Li, J., MacQueen, P., Meibom, S., Prsa, A., Quintana, E. V., Rowe, J., Sherry, W., Tenenbaum, P., Torres, G., Twicken, J. D., Van Cleve, J., Walkowicz, L., & Wu, H. 2011a, ApJ, 728, 117

Borucki, W. J., Koch, D. G., Basri, G., Batalha, N., Brown, T. M., Bryson, S. T., Caldwell, D., Christensen-Dalsgaard, J., Cochran, W. D., DeVore, E., Dunham, E. W., Gautier, III, T. N., Geary, J. C., Gilliland, R., Gould, A., Howell, S. B., Jenkins,

J. M., Latham, D. W., Lissauer, J. J., Marcy, G. W., Rowe, J., Sasselov, D., Boss, A., Charbonneau, D., Ciardi, D., Doyle, L., Dupree, A. K., Ford, E. B., Fortney, J., Holman, M. J., Seager, S., Steffen, J. H., Tarter, J., Welsh, W. F., Allen, C., Buchhave, L. A., Christiansen, J. L., Clarke, B. D., Das, S., Désert, J.-M., Endl, M., Fabrycky, D., Fressin, F., Haas, M., Horch, E., Howard, A., Isaacson, H., Kjeldsen, H., Kolodziejczak, J., Kulesa, C., Li, J., Lucas, P. W., Machalek, P., McCarthy, D., MacQueen, P., Meibom, S., Miquel, T., Prsa, A., Quinn, S. N., Quintana, E. V., Ragozzine, D., Sherry, W., Shporer, A., Tenenbaum, P., Torres, G., Twicken, J. D., Van Cleve, J., Walkowicz, L., Witteborn, F. C., & Still, M. 2011b, ApJ, 736, 19

Brown, T. M., Latham, D. W., Everett, M. E., & Esquerdo, G. A. 2011, AJ, 142, 112

Chambers, J. E., Wetherill, G. W., & Boss, A. P. 1996, Icarus, 119, 261

Christiansen, J. L., Jenkins, J. M., Barclay, T. S., Burke, C. J., Caldwell, D. A., Clarke, B. D., Li, J., Seader, S., Smith, J. C., Stumpe, M. C., Tenenbaum, P., Thompson, S. E., Twicken, J. D., & Van Cleve, J. 2012, ArXiv e-prints

Colón, K. D., Ford, E. B., & Morehead, R. C. 2012, ArXiv e-prints

Correia, A. C. M., Couetdic, J., Laskar, J., Bonfils, X., Mayor, M., Bertaux, J.-L., Bouchy, F., Delfosse, X., Forveille, T., Lovis, C., Pepe, F., Perrier, C., Queloz, D., & Udry, S. 2010, A&A, 511, A21

Doyle, L. R. et al. 2011, Science, 333, 1602

Fabrycky, D. C., Lissauer, J. J., Ragozzine, D., Rowe, J. F., Agol, E., Barclay, T., Batalha, N., Borucki, W., Ciardi, D. R., Ford, E. B., Geary, J. C., Holman, M. J., Jenkins, J. M., Li, J., Morehead, R. C., Shporer, A., Smith, J. C., Steffen, J. H., & Still, M. 2012, ArXiv e-prints

Figueira, P., Marmier, M., Boué, G., Lovis, C., Santos, N. C., Montalto, M., Udry, S., Pepe, F., & Mayor, M. 2012, A&A, 541, A139

Fressin, F., Torres, G., Désert, J.-M., Charbonneau, D., Batalha, N. M., Fortney, J. J., Rowe, J. F., Allen, C., Borucki, W. J., Brown, T. M., Bryson, S. T., Ciardi, D. R., Cochran, W. D., Deming, D., Dunham, E. W., Fabrycky, D. C., Gautier, III, T. N., Gilliland, R. L., Henze, C. E., Holman, M. J., Howell, S. B., Jenkins, J. M., Kinemuchi, K., Knutson, H., Koch, D. G., Latham, D. W., Lissauer, J. J., Marcy, G. W., Ragozzine, D., Sasselov, D. D., Still, M., Tenenbaum, P., & Uddin, K. 2011, ApJS, 197, 5

Gladman, B. 1993, Icarus, 106, 247

Good, P. I. 2006, Resampling Methods: A Practical Guide to Data Analysis, 3rd edn. (Boston: Birkhauser), 218

Hoel, P. 1984, Introduction to mathematical statistics, Wiley series in probability and mathematical statistics. Probability and mathematical statistics (Wiley)

Holman, M. J., Fabrycky, D. C., Ragozzine, D., Ford, E. B., Steffen, J. H., Welsh, W. F., Lissauer, J. J., Latham, D. W., Marcy, G. W., Walkowicz, L. M., Batalha, N. M., Jenkins, J. M., Rowe, J. F., Cochran, W. D., Fressin, F., Torres, G., Buchhave, L. A., Sasselov, D. D., Borucki, W. J., Koch, D. G., Basri, G., Brown, T. M., Caldwell, D. A., Charbonneau, D., Dunham, E. W., Gautier, T. N., Geary, J. C., Gilliland, R. L., Haas, M. R., Howell, S. B., Ciardi, D. R., Endl, M., Fischer, D., Fürész, G., Hartman, J. D., Isaacson, H., Johnson, J. A., MacQueen, P. J., Moorhead, A. V., Morehead, R. C., & Orosz, J. A. 2010, Science, 330, 51

Howard, A. W., Marcy, G. W., Bryson, S. T., Jenkins, J. M., Rowe, J. F., Batalha, N. M., Borucki, W. J., Koch, D. G., Dunham, E. W., Gautier, T. N., Cleve, J. V., Cochran, W. D., Latham, D. W., Lissauer, J. J., Torres, G., Brown, T. M., Gilliland, R. L., Buchhave, L. A., Caldwell, D. A., Christensen-Dalsgaard, J., Ciardi, D., Fressin, F., Haas, M. R., Howell, S. B., Kjeldsen, H., Seager, S., Rogers, L., Sasselov, D. D., Steffen, J. H., Basri, G. S., Charbonneau, D., Christiansen, J., Clarke, B., Dupree, A., Fabrycky, D. C., Fischer, D. A., Ford, E. B., Fortney, J. J., Tarter, J., Girouard, F. R., Holman, M. J., Johnson, J. A., Klaus, T. C., Machalek, P., Moorhead, A. V., Morehead, R. C., Ragozzine, D., Tenenbaum, P., Twicken, J. D., Quinn, S. N., Isaacson, H., Shporer, A., Lucas, P. W., Walkowicz, L. M., Welsh, W. F., Boss, A., Devore, E., Gould, A., Smith, J. C., Morris, R. L., Prsa, A., Morton, T. D., Still, M., Thompson, S. E., Mullally, F., Endl, M., & MacQueen, P. J. 2012, The Astrophysical Journal Supplement Series, 201, 15

Johansen, A., Davies, M., Church, R. P., & Holmelin, V. 2012, ArXiv e-prints

Konacki, M. & Wolszczan, A. 2003, ApJ, 591, L147

Lissauer, J. J., Fabrycky, D. C., Ford, E. B., Borucki, W. J., Fressin, F., Marcy, G. W., Orosz, J. A., Rowe, J. F., Torres, G., Welsh, W. F., Batalha, N. M., Bryson, S. T., Buchhave, L. A., Caldwell, D. A., Carter, J. A., Charbonneau, D., Christiansen, J. L., Cochran, W. D., Desert, J.-M., Dunham, E. W., Fanelli, M. N., Fortney, J. J., Gautier, III, T. N., Geary, J. C., Gilliland, R. L., Haas, M. R., Hall, J. R., Holman, M. J., Koch, D. G., Latham, D. W., Lopez, E., McCauliff, S., Miller, N., Morehead, R. C., Quintana, E. V., Ragozzine, D., Sasselov, D., Short, D. R., & Steffen, J. H. 2011a, Nature, 470, 53

Lissauer, J. J., Marcy, G. W., Rowe, J. F., Bryson, S. T., Adams, E., Buchhave, L. A., Ciardi, D. R., Cochran, W. D., Fabrycky, D. C., Ford, E. B., Fressin, F., Geary, J., Gilliland, R. L., Holman, M. J., Howell, S. B., Jenkins, J. M., Kinemuchi, K., Koch, D. G., Morehead, R. C., Ragozzine, D., Seader, S. E., Tanenbaum, P. G., Torres, G., & Twicken, J. D. 2012, ApJ, 750, 112

Lissauer, J. J., Ragozzine, D., Fabrycky, D. C., Steffen, J. H., Ford, E. B., Jenkins, J. M., Shporer, A., Holman, M. J., Rowe, J. F., Quintana, E. V., Batalha, N. M., Borucki, W. J., Bryson, S. T., Caldwell, D. A., Carter, J. A., Ciardi, D., Dunham, E. W., Fortney, J. J., Gautier, III, T. N., Howell, S. B., Koch, D. G., Latham, D. W., Marcy, G. W., Morehead, R. C., & Sasselov, D. 2011b, ApJS, 197, 8

McArthur, B. E., Benedict, G. F., Barnes, R., Martioli, E., Korzennik, S., Nelan, E., & Butler, R. P. 2010, ApJ, 715, 1203

Moorhead, A. V., Ford, E. B., Morehead, R. C., Rowe, J., Borucki, W. J., Batalha, N. M., Bryson, S. T., Caldwell, D. A., Fabrycky, D. C., Gautier, III, T. N., Koch, D. G., Holman, M. J., Jenkins, J. M., Li, J., Lissauer, J. J., Lucas, P., Marcy, G. W., Quinn, S. N., Quintana, E., Ragozzine, D., Shporer, A., Still, M., & Torres, G. 2011, ApJS, 197, 1

Morton, T. D. & Johnson, J. A. 2011, ApJ, 738, 170

Ofir, A. & Dreizler, S. 2012, ArXiv e-prints

Press, W. H., Teukolsky, S. A., Vetterling, W. T., & Flannery, B. P. 1992, Numerical recipes in FORTRAN. The art of scientific computing

Sanchis-Ojeda, R. et al. 2012, Nature, 487, 449

Santerne, A., Díaz, R. F., Moutou, C., Bouchy, F., Hébrard, G., Almenara, J.-M., Bonomo, A. S., Deleuil, M., & Santos, N. C. 2012, A&A, 545, A76

Stuart, A. & Ord, J. 1991, Kendall's Advanced Theory of Statistics, Vol. 2, Classical Inference and Relationship, Kendall's Advanced Theory of Statistics, 5th edn. (Oxford University Press)

Tremaine, S. & Dong, S. 2012, AJ, 143, 94

Weissbein, A., Steinberg, E., & Sari, R. 2012, ArXiv e-prints

Winn, J. N. 2010, ArXiv e-prints

Youdin, A. N. 2011, ApJ, 742, 38

Chapter 4

Are Planetary Systems Filled to Capacity? A Study Based on *Kepler* Results

Reproduced by permission of the AAS (Fang, J., and Margot, J.L., 2013, The Astrophysical Journal, 767, 115).

1. Introduction

We examine the question of whether planetary systems generally consist of closely spaced planets in packed configurations or whether planets in the same system are generally more widely spaced apart. Here we adopt the traditional definition of *dynamical spacing* as the separation between adjacent planets in terms of their mutual Hill radius, and we define a planetary system to be *dynamically packed* if the system is "filled to capacity", i.e., it cannot accept an additional planet without leading to instability.

The degree of packing in planetary systems has important implications for their origin and evolution. It has been codified in the *packed planetary systems* (PPS) hypothesis (e.g., Barnes & Quinn 2004; Raymond & Barnes 2005; Raymond et al. 2006; Barnes & Greenberg 2007), the idea that all planetary systems are dynamically packed. Previous works have invoked the PPS hypothesis to predict the existence of additional planets in systems with observed planets located far apart with an intermediate stability zone (e.g. Menou & Tabachnik 2003; Barnes & Quinn 2004; Raymond & Barnes 2005; Ji et al. 2005; Rivera & Haghighipour 2007; Raymond et al. 2008; Fang & Margot 2012b), since the PPS hypothesis requires that an undetected planet is located in that stability zone. Systems that are observed to have dense configurations could support the PPS hypothesis if they were shown to be dynamically packed. Such systems may include Kepler-11, with six transiting planets within 0.5 AU (Lissauer et al. 2011b), Kepler-36, whose 2 known planets have semi-major axes differing by only $\sim$10% (Carter et al. 2012), and KOI-500, which has 5 planets all within an orbital period of 10 days (Ragozzine et al. 2012).

In this study we seek to investigate the underlying distribution of dynamical spacing in planetary systems by fitting to the observed properties of *Kepler* planet candidates. By *underlying* or *intrinsic*, we mean our best estimate of the true distribution of dynamical spacing between neighboring planets in multi-planet systems, i.e., free of observational biases. After we derive the underlying distribution of the dynamical spacing between planets, we create planetary systems whose planets have separations that obey this distribution. We then subject these planetary systems to N-body integrations to examine their stability properties, which allows us to determine if they are dynamically packed or not. By determining the fraction of systems that are packed, we can test the PPS hypothesis.

In a related study published by Fang & Margot (2012a), we investigated the underlying multiplicity and inclination distribution of planetary systems based on the *Kepler* catalog of planetary candidates from Batalha et al. (2012) in February 2012. We created population models of planetary systems following different multiplicity and inclination distributions, simulated observations of these systems by *Kepler*, and compared the properties of detected planets in our simulations with the properties of actual *Kepler* planet detections. We used two types of observables: numbers of transiting systems (i.e., numbers of singly transiting systems, doubly transiting systems, triply transiting systems, etc.) and normalized transit duration ratios. Within our orbital period and planet radius regime ($P \leq 200$ days, $1.5\ R_{\oplus} \leq R \leq 30\ R_{\oplus}$), we found that most planetary systems had $1-2$ planets with typical inclinations less than 3 degrees. In the present study, we build upon and extend this previous investigation to explore the underlying distribution of dynamical spacing in planetary systems using data from the *Kepler* mission.

This paper is organized as follows. In Section 2.1, we define our stellar and planetary parameter space. We also describe how we created model populations of planetary systems and how we compared them to the properties of *Kepler* planetary candidates. In Section

2.2, we present the best-fit model representing our best estimate of the intrinsic distribution of dynamical spacing in planetary systems. In Section 3, we compare this distribution of dynamical spacing with that of the Solar System. We also make comparisons with two other systems, Kepler-11 and Kepler-36, to quantify how rare such systems are. In Section 4, we test and quantify whether such a distribution of dynamical spacing implies that planetary systems are dynamically packed, by performing an ensemble of N-body integrations. We briefly describe implications for the PPS hypothesis. Section 5 summarizes the main conclusions of this study.

2. Dynamical Spacing of Planets

2.1. Methods

Our methods for deriving the intrinsic dynamical spacing of planetary systems are as follows. First, we created model populations of planetary systems obeying different underlying distributions of dynamical spacing. Second, we performed synthetic observations of the planetary systems in these populations by the *Kepler* spacecraft. At this stage we identified which simulated planets were detectable by the *Kepler* telescope, and which were not. Third, we compared the resulting distribution of dynamical spacing of detectable planets from synthetic populations with that of the actual *Kepler* detections. The actual distribution can be easily obtained from *Kepler* transit data with an assumed planet radius-mass relationship. Most of these steps are fully explained in Fang & Margot (2012a), and we refer the reader to that paper for details. In the following paragraphs, we summarize the most salient points of our procedure as well as any differences with Fang & Margot (2012a).

Each model population consists of about 10^6 planetary systems, and we created various model populations that followed different underlying distributions of multiplicity, inclinations, and dynamical spacing. To generate these populations, we needed to restrict the range of physical and orbital properties of the stars and planets that we considered in our simulations. We selected ranges that would adequately overlap those of a *Kepler* sample that can be considered nearly complete (Howard et al. 2012; Youdin 2011). Stellar properties such as radius R_*, stellar noise σ_*, effective temperature $T_{\rm eff}$, surface gravity parameter $\log(g)$, and *Kepler* magnitude K were randomly drawn from the Kepler Input Catalog (see Fang & Margot 2012a). We only considered bright solar-like stars that obeyed the following ranges:

$$\begin{gathered} 4100 \text{ K} \leq T_{\rm eff} \leq 6100 \text{ K}, \\ 4.0 \leq \log(g \text{ [cm s}^{-2}\text{]}) \leq 4.9, \\ K \leq 15 \text{ mag}. \end{gathered} \tag{1}$$

Planet radii and orbital periods were drawn from debiased distributions, and we obtained these debiased distributions by converting the observed sample of Kepler Objects of Interest (KOI; based on detections up to Quarter 6 released in February 2012, Batalha et al. 2012) into a debiased sample using calculations of detection efficiencies (see Fang & Margot 2012a). We filtered the KOI sample (and correspondingly limited the parameter space of the synthetic populations described in this paper) to the following orbital period P, planet radius R, and signal-to-noise ratio (SNR) boundaries:

$$\begin{gathered} P \leq 200 \text{ days}, \\ 1.5\ R_\oplus \leq R \leq 30\ R_\oplus, \\ \text{SNR}(\rightarrow \text{Q8}) \geq 11.5. \end{gathered} \tag{2}$$

These limits were imposed in order to choose a sample of planets with properties unlikely to be missed by the *Kepler* detection pipeline. For SNR, we required an SNR$\geq$10 for observations up to Quarter 6, which corresponds to about SNR$\geq$11.5 for observations up to Quarter 8 by assuming that SNR roughly scales as $\sqrt{N}$, where N is the number of observed transits. This scaling is performed because the SNRs of observed KOIs have been reported for observations up to Quarter 8 in Batalha et al. (2012), whereas the actual detections have been reported up to Quarter 6 only. Planet masses M were calculated by converting from planet radii R. We used a broken log-linear $M(R)$ prescription obtained by fitting to masses and radii of transiting planets (see Fang & Margot 2012a):

$$\log_{10}\left(\frac{M}{M_{\rm Jup}}\right) = 2.368\left(\frac{R}{R_{\rm Jup}}\right) - 2.261 \qquad \text{for} \left(\frac{R}{R_{\rm Jup}}\right) < 1.062, \tag{3}$$

$$\log_{10}\left(\frac{M}{M_{\rm Jup}}\right) = -0.492\left(\frac{R}{R_{\rm Jup}}\right) + 0.777 \qquad \text{for} \left(\frac{R}{R_{\rm Jup}}\right) \geq 1.062. \tag{4}$$

Additionally, we repeated all of the methods described in this section by using an alternate mass-radius relationship: $(M/M_\oplus) = (R/R_\oplus)^{2.06}$ (Lissauer et al. 2011b). By adopting this alternate mass-radius equation, our results showed the same best-fit dynamical spacing distribution as defined in Equation (7) with σ =14.5 (see results presented in Section 2.2). We note that both of these mass-radius equations were obtained by fitting to the sample of planets with known masses and radii. Errors in the mass-radius relationships can potentially affect our results because our determination of dynamical spacing is a direct function of planetary masses. In Figure 1, we investigate how uncertainties in the mass-radius relationship map into dynamical spacing uncertainties. Specifically, we plot histograms showing how the observed dynamical spacing changes if there is a $1-\sigma$ increase or decrease in mass for the mass-radius equation. For masses lower than nominal, adjacent planets appear to be less closely spaced and so the distribution shifts to the right. For masses higher than nominal, adjacent planets appear to be more closely spaced and so the distribution shifts to the left. The shifts are quantified at the end of Section 2.2.

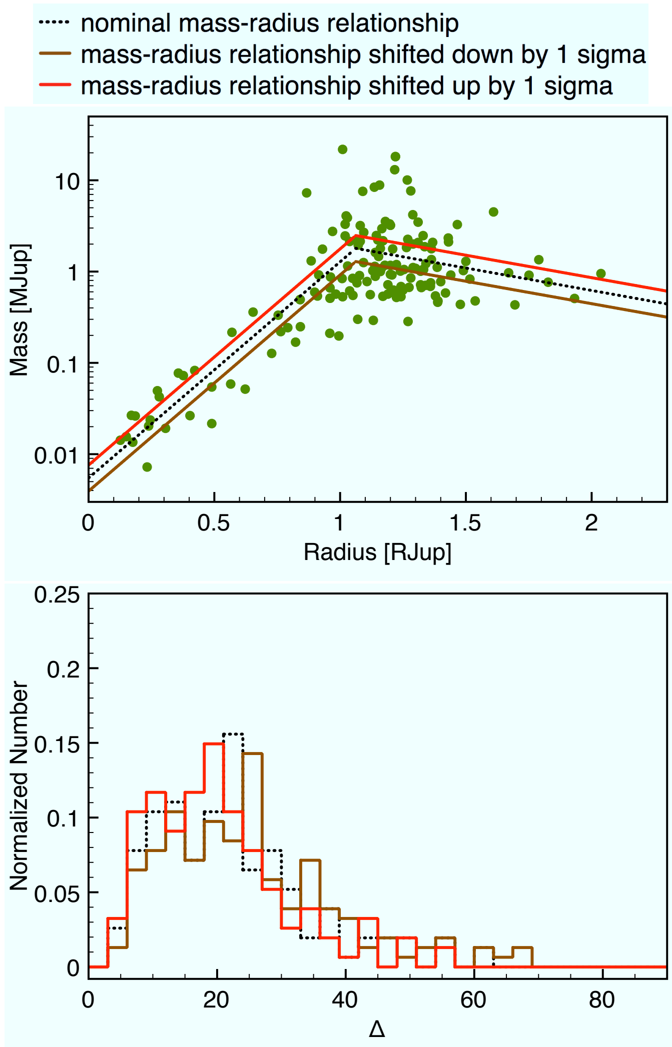

Fig. 1.— (Top) Observed transiting exoplanets with known masses and radii shown in green, and the corresponding mass-radius relationship. (Bottom) Dependence of the observed dynamical spacing distribution on the choice of mass-radius relationship. In both panels, the nominal mass-radius relationship as defined in Equations (3) and (4) is shown in black, and the mass-radius relationship shifted by one sigma to lower (higher) masses is shown in brown (red). Δ represents the number of mutual Hill radii between adjacent planets in multi-planet systems and is defined in Equation (5).

For orbital eccentricities, we adopted circular orbits, as we did in Fang & Margot (2012a).

Eccentricities do not directly affect our calculation of dynamical spacing, as we will define below in Equation (5).

Regarding the multiplicity distribution in our model populations, we used a bounded uniform distribution with $\lambda = 1.5 - 3.5$ with increments of 0.25 to assign the number of planets per system. A bounded uniform distribution has a single parameter λ and is defined as follows: first, draw a value $N_{\rm max}$ (maximum number of planets) from a Poisson distribution with parameter λ that ignores zero values, and second, draw the number of planets from a discrete uniform distribution with range $1 - N_{\rm max}$ (Fang & Margot 2012a). Thus, each planetary system will have at least one planet. For the inclination distribution of planetary orbits, we used a Rayleigh distribution with $\sigma = 1, 2°$ as well as a Rayleigh of Rayleigh distribution with $\sigma_\sigma = 1, 2°$. A Rayleigh of Rayleigh distribution has a single parameter σ_σ and is defined as follows: first, draw a value σ from a Rayleigh distribution with parameter σ_σ, and second, draw a value for inclination from a Rayleigh distribution with parameter σ (Lissauer et al. 2011b). These specific multiplicity and inclination distributions were chosen because they yielded fits consistent with transit numbers and transit duration ratios from *Kepler* detections (see Fang & Margot 2012a). Combinations of these specific multiplicity and inclination distributions add up to a total of 36 possibilities.

The difference between model populations generated in Fang & Margot (2012a) and the model populations generated in this study is the treatment of planetary separations, since here we wish to determine the underlying dynamical spacing of planetary systems. We used a separation criterion Δ to assess the dynamical spacing between all adjacent planets in multi-planet systems, where Δ is defined as (e.g., Gladman 1993; Chambers et al. 1996)

$$\Delta = \frac{a_2 - a_1}{R_{H1,2}}, \tag{5}$$

with

$$R_{H1,2} = \left(\frac{M_1 + M_2}{3M_*}\right)^{1/3} \frac{a_1 + a_2}{2}. \tag{6}$$

In these equations, a is the semi-major axis, $R_{H1,2}$ is the mutual Hill radius, and M is the mass. Subscripts $*$, 1, and 2 refer to the star, the inner planet, and the outer planet, respectively. For a two-planet system not in resonance, the planets are required to be spaced with $\Delta \gtrsim 3.46$ in order to be Hill stable.

In our model populations, adjacent planets in multi-planet systems were spaced according to a prescribed Δ distribution. We used a shifted Rayleigh distribution, which is the same as a regular Rayleigh distribution except shifted to the right by 3.5 (since we require this distribution to provide values of Δ that meet the minimum Hill stability limit). Such a distribution, as we will show, matches the observed sample well. The mathematical form of a shifted Rayleigh distribution f is

$$f(\Delta) = \frac{\Delta - 3.5}{\sigma^2} e^{-(\Delta-3.5)^2/(2\sigma^2)}, \tag{7}$$

and is described by a single parameter σ. In our model populations, we explored values of $\sigma = 10-20$ with increments of 0.5 for a total of 21 possibilities. We chose this range of σ values based on the location of the observed Δ distribution (blue histogram in Figure 2) with its approximate peak at about 20 mutual Hill radii. This chosen range of σ values allowed us to explore different distributions of dynamical spacing that spanned a reasonable range of possible model Δ distributions. Increments of 0.5 were chosen as a trade-off between resolution and computational limitations. As will be seen in Section 2.2, the statistically good match between the data and the best-fit model demonstrates that our increments are sufficiently small and have appropriately sampled the possible range of Δ distributions.

In order to enforce that adjacent planets are spaced according to the prescribed Δ distribution, we performed the following steps. For each synthetic planetary system, the first planet's orbital period is drawn from the debiased period distribution. If the system's multiplicity is greater than one, for the second planet we draw its separation Δ from the first planet using the prescribed Δ distribution and we also draw a value from the debiased period distribution. If that value is less/greater than the first planet's period, then the second planet will be the inner/outer planet and its exact period will be calculated by satisfying the drawn

Δ separation from the first planet. This process repeats if the system has additional planets. These steps are different from Fang & Margot (2012a), where in that study all planetary orbital periods were chosen by drawing them from a debiased distribution. We verified that the periods drawn to match the Δ distribution provide a very close match to the debiased period distribution as well.

After the creation of each model population, we performed synthetic observations of each population's planetary systems by the *Kepler* spacecraft in order to determine which planets were transiting and detectable (see Fang & Margot 2012a). The transiting requirement was evaluated by picking a random line-of-sight (i.e., picking a random point on the celestial sphere) and computing the planet−star distance projected on the plane of the sky. The minimum of that distance was compared to the radius of the host star to determine if the planet in our simulations transited or not. The detection requirement was assessed by calculating each transiting planet's SNR, defined as

$$\mathrm{SNR} = \left(\frac{R}{R_*}\right)^2 \frac{\sqrt{N}}{\sigma_*}, \tag{8}$$

where the first fraction gives the depth of the transit, N represents the number of transits up to Quarter 6, and σ_* represents stellar noise (Combined Differential Photometric Precision or CDPP; Christiansen et al. 2012). Since CDPP is quarter-to-quarter dependent, we used the median CDPP value over all available quarters. In the calculation of SNR, we took into account gaps between *Kepler* quarters, the fact that not all stars are observed each quarter, and a 95% duty cycle (Fang & Margot 2012a). If the calculated SNR for a transiting planet met or exceeded the SNR threshold for detection (SNR=10), then it was considered detectable.

Lastly, we determined the goodness-of-fit between each model population's detected planets and the actual *Kepler* detections. This was ascertained by comparing the Δ distributions of adjacent planets in their multi-planet systems. We performed a Kolmogorov-Smirnov (K-S) test to assess the fit between the Δ distributions, and this comparison yielded a p-value that we used to evaluate the null hypothesis that the distributions emanate from the same parent distribution. This K-S probability was used to determine how well a particular model matched the observations. We also calculated the goodness-of-fit for multiplicity (by comparing with observed *Kepler* numbers of transiting systems using a chi-square test) and for inclination (by comparing with observed, normalized transit duration ratios using a K-S test) to check that they were consistent with the data (see Fang & Margot 2012a). While we only generated model populations with underlying multiplicity and inclination distributions that are considered to be good fits to the data based on our previous work, this extra step allowed us to confirm that any models with acceptable Δ fits also produced acceptable multiplicity and inclination fits to the Kepler data. We determined which model populations were most consistent with the data by combining (multiplying) the probabilities associated with each one of the 3 statistical tests that probed multiplicity, inclination, and dynamical spacing. We assumed that these probabilities are independent.

Accounting for all combinations of multiplicity, inclination, and dynamical spacing distributions, in total we created 756 model populations with about 10^6 planets each. As described earlier, each of these model populations underwent synthetic observations by *Kepler* as well as statistical tests. The next section presents our results.

2.2. Results

We report our results on the dynamical spacing (represented by the criterion Δ) in multi-planet systems based on *Kepler* data. Using the methods described in the previous section, we determine that our best-fit model for the intrinsic Δ distribution is a shifted Rayleigh distribution (see Equation (7)) with $\sigma = 14.5$.

This best-fit distribution is plotted in Figure 2, where we show its probability density distribution (top panel) as well as its cumulative probability distribution (bottom panel). This best-fit distribution has a mean value of $\Delta = 21.7$ with a standard deviation of 9.5. About 50% of neighboring planet pairs have Δ separations larger than 20, and about 90%

of neighboring planet pairs have Δ separations larger than 10. This best-fit distribution was obtained by considering shifted Rayleigh distributions with increments in σ of 0.5. The mean values for distributions with $\sigma = 14.0$ and $\sigma = 15.0$ are $\Delta = 22.3$ and $\Delta = 21.0$, respectively. The combined probabilities for the match to the data using distributions with $\sigma = 14.0$ and $\sigma = 15.0$ are less than half the combined probability using $\sigma = 14.5$.

Our results are valid for the range of stellar and planetary parameters given in Equations (1) and (2), most notably a minimum planet radius of 1.5 $R_{\oplus}$ and a maximum orbital period of 200 days. It is possible that planets are actually even more closely spaced than this best-fit distribution if there are planets located in intermediate locations with radii less than 1.5 $R_{\oplus}$. Therefore, our findings about the Δ distribution can be used to represent the spacing of planetary systems confined to the scope of our study, or can serve as an upper limit for the spacing of planetary systems that include planets with smaller radii.

Figure 3 shows the comparison between the Δ distribution of simulated detections from this best-fit model's population and the observed Δ from actual *Kepler* detections. Note that this figure does not show the underlying Δ distribution that is plotted in Figure 2; instead, this figure shows the distribution of simulated planets that *would have been detected*, in order to make an appropriate comparison with the observed Δ distribution. The K-S test for comparing these two distributions yields a p-value of 56%, indicating that we cannot reject the null hypothesis that these distributions are drawn from the same parent distribution. In other words, this model is consistent with the observations.

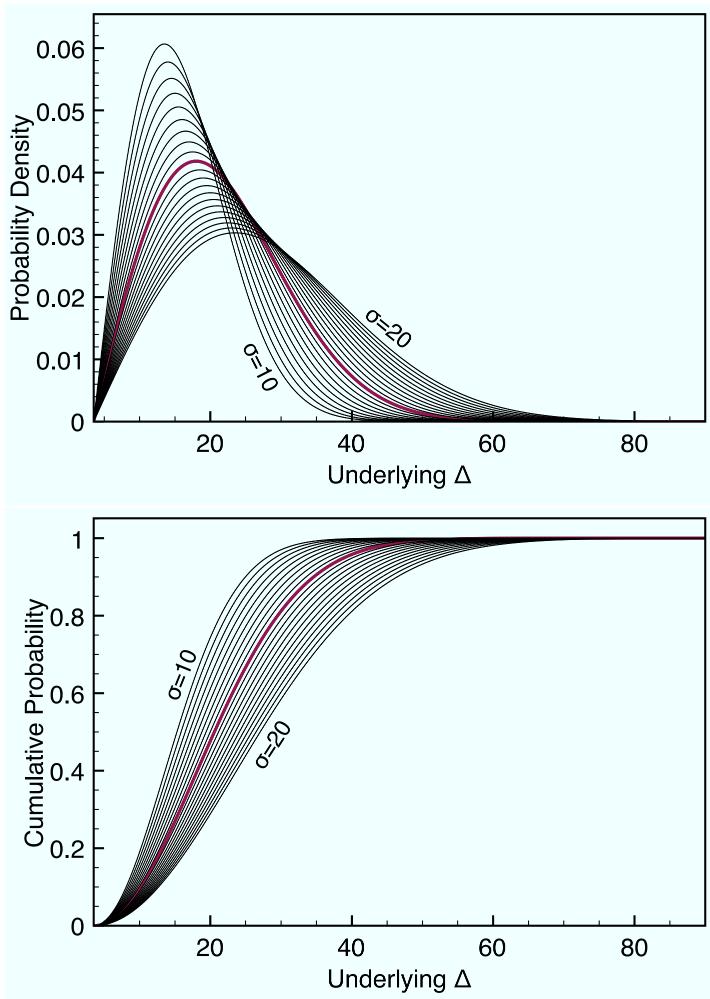

Fig. 2.— The best-fit model's underlying Δ distribution is shown as a magenta-colored curve. This distribution represents our best estimate of the true or intrinsic (i.e., free of observational bias) distribution of dynamical spacing between all neighboring planets meeting our orbital period and planet radius criteria. Recall that Δ represents the difference in semi-major axes between two adjacent orbits; it is expressed in units of the mutual Hill radius. The best-fit model is a shifted Rayleigh distribution as defined in Equation (7) with $\sigma = 14.5$; the top plot depicts the probability density and the bottom plot shows the cumulative probability. The black-colored curves show the range and sampling frequency of model distributions that follow different σ parameter values ranging from $\sigma = 10$ to $\sigma = 20$ with increments of 0.5, as examined in this study.

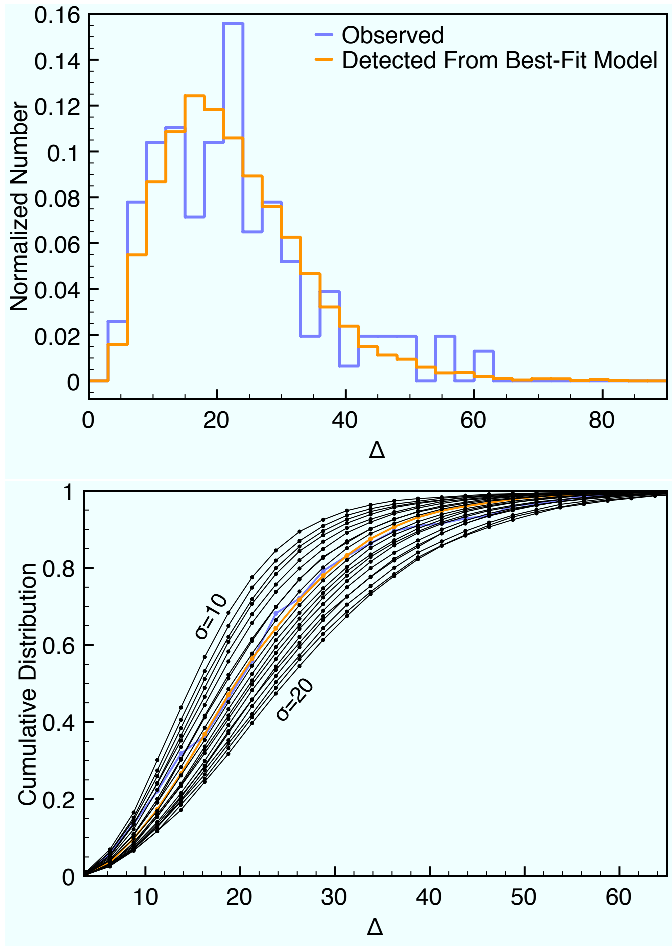

Fig. 3.— The top plot shows the comparison between the observed Δ distribution from actual *Kepler* detections (shown in blue) and the Δ distribution from simulated detections in our best-fit model population (shown in orange); the K-S probability for this match is 56%. The bottom plot shows this comparison in cumulative form and its histogram points are connected by lines for easy viewing, and also shows the comparison with the properties of detected planets from other model populations (σ =10 to σ =20 with increments of 0.5; shown in black). The 99.5% confidence region of acceptable fits includes model populations with σ ranging from 12.5 to 17.0.

Comparison between Figures 2 and 3 shows that the underlying Δ distribution is similar to the observed Δ distribution–both distributions have peaks near $\Delta \sim 20$. This suggests that the observed Δ distribution is not indicative of a significant population of non-transiting and/or low-SNR planets (within the planet radius and orbital period limits of our study) located in-between detected planets; otherwise, the underlying Δ distribution would have on average lower Δ values than those of the observed distribution. We caution again that our study cannot rule out the existence of a population of planets with $R < 1.5R_{\oplus}$, so the actual underlying Δ distribution could be different from what our results indicate. The similarity between the observed and underlying Δ distributions is due to the rarity of cases where a system has $\Delta_{\text{observed}} > \Delta_{\text{underlying}}$ (i.e., an undetected planet located in-between two detected planets). The stringent geometric probability of transit means that outer planets are more easily missed than inner planets. As a result, it will be rare to find cases where an intermediate planet is non-transiting and therefore missed, but both the innermost and outermost planets are transiting and detected. For such a case, which rarely occurs, the observed Δ would be greater than the underlying Δ.

We discuss how we expect these results to change if an alternate mass-radius relationship is used. In particular, Figure 1 shows how the observed dynamical spacing distribution changes depending on various choices for the mass-radius relationship. For computational expediency, we chose to evaluate the effects of the mass-radius relationship on the *observed* Δ distribution. We use this as an approximation for the effects on the *underlying* Δ distribution, with the justification that the observed and underlying Δ distributions appear similar (see previous paragraph). For the mass-radius relationship shifted down by 1 sigma, the best-fitting shifted Rayleigh distribution has $\sigma = 16.5$. For the mass-radius relationship shifted up by 1 sigma, the best-fitting shifted Rayleigh distribution has $\sigma = 12.5$. As a result, we estimate that our derived dynamical spacing distribution can span σ =12.5−16.5 due to uncertainties in the mass-radius scaling.

3. Comparison to the Solar System, Kepler-11, and Kepler-36

We can compare our results (i.e., the intrinsic dynamical spacing or Δ distribution) with the dynamical spacing distribution of the Solar System, if we extrapolate beyond the radius and period limits (Equation (2)) of our study. Figure 4 shows our intrinsic Δ distribution of planetary systems overplotted with a histogram of the Δ distribution of the Solar System planets. From this figure, it is interesting to note that the distributions appear to be relatively similar and that the Solar System planets may be similarly spaced as most exoplanets in general. A K-S test between our cumulative Δ distribution and the sample of Δ values between adjacent planets in the Solar System yields a p-value of 66.2%, indicating that the Solar System Δ distribution is consistent with that of Figure 2.

The orbital evolution of the planets in the Solar System is known to be chaotic and unstable (e.g., Sussman & Wisdom 1988; Laskar 1989, 1990; Sussman & Wisdom 1992; Laskar 1994; Michtchenko & Ferraz-Mello 2001; Lecar et al. 2001). The inner Solar System can be potentially unstable within the Sun's remaining lifetime due to a secular resonance (Batygin & Laughlin 2008). Laskar (1994) and Laskar & Gastineau (2009) have shown that inner planets could be ejected or collide. Numerical simulations of the planets in the outer Solar System suggest that they are packed (Barnes & Quinn 2004; Raymond & Barnes 2005; Barnes et al. 2008). All of these results suggest that the Solar System is dynamically packed. If we consider the Solar System to be dynamically packed then it is possible that other planetary systems with similar planet multiplicities and Δ distributions are also dynamically packed. This prompted us to verify whether planetary systems in general are dynamically packed (see Section 4).

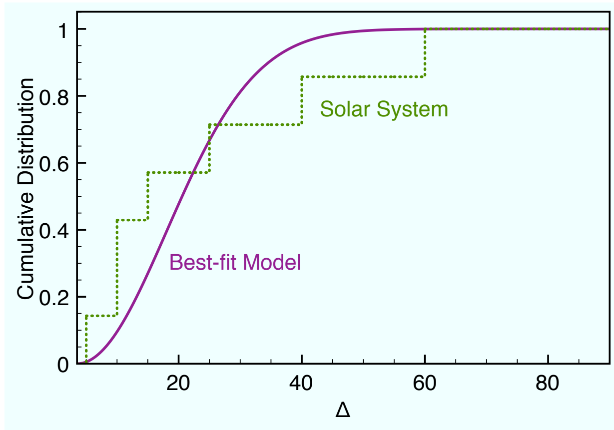

Fig. 4.— Comparison of the cumulative Δ distribution between the best-fit model's Δ distribution (i.e., shifted Rayleigh distribution with $\sigma = 14.5$; purple solid line) and the Solar System's Δ distribution (i.e., histogram based on its 8 planets; dotted green line).

Kepler-11 is a planetary system with six known transiting planets in a closely spaced configuration (Lissauer et al. 2011a). All six transiting planets have orbits smaller than the orbit of Venus, and five of the six transiting planets have orbits smaller than the orbit of Mercury. This appears to be a very compact system, and we calculate the Δ separations of the innermost five planets to be $\Delta_{\rm b-c}$ =5.7, $\Delta_{\rm c-d}$ =14.6, $\Delta_{\rm d-e}$ =8.0, and $\Delta_{\rm e-f}$ =11.2. We did not calculate the Δ separation of the f−g planet pair because the mass of planet g is not known and only has an upper limit. Accounting for the 1σ uncertainties on mass reported by Lissauer et al. (2011a), the dynamical spacing of these pairs have the following ranges: $\Delta_{\rm b-c}$ =5.1−7.0, $\Delta_{\rm c-d}$ =13.0−17.3, $\Delta_{\rm d-e}$ =7.2−8.8, and $\Delta_{\rm e-f}$ =10.0−12.6. All of the Kepler-11 planets are within the planet radius and orbital period scope of our study, and we apply our knowledge of the intrinsic dynamical spacing (i.e., Figure 2) to this system. We find that the separation $\Delta_{\rm b-c}$ =5.7 is more closely spaced than 98.9% of adjacent planet pairs in multi-planet systems, $\Delta_{\rm c-d}$ =14.6 is more closely spaced than 74.6%, $\Delta_{\rm d-e}$ =8.0 is more closely spaced than 95.3%, and $\Delta_{\rm e-f}$ =11.2 is more closely spaced than 86.8%. These high percentages indicate that the planetary separations in the Kepler-11 system are much smaller than average separations in planetary systems, and we conclude that Kepler-11 is unusual in terms of the density of its configuration.

Kepler-36 has two known transiting planets with a large density contrast (their densities differ by a factor of $\sim$8) yet they orbit closely to one another (semi-major axes differ by $\sim$10%) (Carter et al. 2012). Such close orbits with dissimilar densities are unusual compared to the planets in the Solar System, where the denser terrestrial planets are located in the inner region and the less-dense giant planets are located in the outer region. We calculate the dynamical spacing between the two planets in Kepler-36 to be Δ=4.7. In comparison to our intrinsic Δ distribution of dynamical spacing, a separation of Δ=4.7 is more closely spaced than 99.7% of neighboring planet pairs of planetary systems in general.

4. Dynamical Packedness of Planets

Section 2.2 described the best-fit Δ distribution of planetary systems based on *Kepler* data, with a mean value of $\Delta = 21.7$ (Figure 2). In this section, we investigate whether this distribution of Δ implies that planetary systems are dynamically packed or not. By *dynamically packed*, we refer to a planetary system that is filled to capacity and cannot include an additional planet without leading to instability.

To investigate whether planetary systems are dynamically packed, we performed long-term N-body integrations of planetary systems generated for our best-fit model population (see Sections 2.1-2.2). For each multiplicity (i.e., 2-planet systems, 3-planet systems, 4-planet systems), we randomly chose 1000 planetary systems for which we performed long-term integrations. In total, we performed 3000 integrations. We did not include single planet systems because they are irrelevant for studies of dynamical packedness and we did not include systems with multiplicities higher than 4 planets because they are relatively rare for our parameter space (Fang & Margot 2012a).

For each integration, we added an additional planet when testing for stability; this planet had a mass equal to the lowest mass of all original planets and its initial conditions included an orbital eccentricity of zero, an inclination drawn from a Rayleigh of Rayleigh distribution with $\sigma_\sigma = 1°$ (see Section 2.1), and random values for its argument of pericenter, longitude of the ascending node, and mean anomaly. This additional planet was placed in-between the orbits of existing planets, and if there were 3 or 4 original planets, we randomly determined which 2 adjacent planets would be receiving a new neighbor. The additional planet's semi-major axis was calculated so that it was located with equal mutual Hill radii distances between its neighboring planets. These initial conditions for the additional planet (e.g., low eccentricities, low inclinations, a mass equal to the lowest mass of original planets, a semi-major axis located at equal Δ distances from neighboring planets) are very conservative in the sense that we have chosen initial conditions that are very amenable to stability, as we determine whether a planetary system with this additional planet can remain stable or not.

Our simulations were performed using a hybrid symplectic/Bulirsch-Stoer integrator from the *Mercury* package (Chambers 1999), and we used a timestep that covered 1/25 of the innermost planet's orbital period. Simulations were performed for a length of 10^8 years; the instability timescales had median values less than 10^5 years. Possible outcomes included either a stable system with no instabilities or a system with at least one instability defined as a collision between the star and a planet, a collision between planets, and/or an ejected planet. All of these planetary systems were verified to be stable for 10^8 years before adding the additional planet.

The results of our simulations can be divided into two camps. The first group is composed of planetary systems that became unstable in our integrations. This suggests that these planetary systems are dynamically packed, since the addition of another planet in an intermediate orbit resulted in an unstable planetary system. We found that 31%, 35%, and 45% of 2-, 3-, and 4-planet systems were unstable, respectively (Table 1). The second group is composed of planetary systems that did not exhibit any signs of instability. For these systems, although they were stable within the scope of our integrations, they may still be dynamically packed. Possible reasons include: an instability may occur on a longer timescale than our integration time, there may be additional planets in the system beyond the scope of our orbital period range of 200 days, or there may be additional planets in the system smaller than 1.5 $R_{\oplus}$, which is the minimum radius of our study. All of these factors would affect the determination of the stability of the system, and so for this second group of systems we are agnostic about their dynamical packedness.

Accordingly, we can only confidently provide a lower limit on packed systems by concluding that at least 31−45% (depending on the system's multiplicity) of planetary systems with dynamical spacings consistent with our best-fit Δ distribution (Figure 2) are dynamically packed. These lower limits are also presented in Table 1. Note that systems with lower multiplicity are more common (Fang & Margot 2012a).

Table 1: Lower Limits on the Percentage of Dynamically Packed Systems

System Multiplicity	**Percentage of Packed Systems**
2-Planet Systems	$\geq 31\%$
3-Planet Systems	$\geq 35\%$
4-Planet Systems	$\geq 45\%$

Lower limits on the percentage of dynamically packed systems as obtained from the fraction of numerical integrations exhibiting instabilities. A planetary system is considered to be dynamically packed if the addition of another planet causes instability. The results of our simulations only provide lower limits because the absence of instability does not indicate that a system is not dynamically packed (see main text).

The packed planetary systems (PPS) hypothesis is the idea that all planetary systems are dynamically packed, and therefore cannot hold additional planets without becoming unstable. The results of our long-term numerical integrations are consistent with the PPS hypothesis, as we find a sizeable lower limit of 31−45% (depending on the system's multiplicity) of planetary systems to be dynamically packed.

5. Conclusions

We have generated model populations of planetary systems and simulated observations of them by the *Kepler* spacecraft. By comparing the properties of detected planets in our simulations with the actual *Kepler* planet detections, we have determined the best-fit distribution of dynamical spacing between neighboring planets. This best-fit distribution is our best estimate of the underlying (i.e., free of observational bias) distribution of dynamical spacing for our orbital period ($P \leq 200$ days) and planet radius ($1.5\ R_\oplus \leq R \leq 30\ R_\oplus$) parameter regime. Stemming from this distribution, the main results of this study are:

1. On average, neighboring planets are spaced 21.7 mutual Hill radii apart, with a standard deviation of 9.5. This distance represents the typical dynamical spacing of neighboring planets for all systems included in the parameter space described above.

2. Our best-fit distribution of dynamical spacing is consistent with the dynamical spacing of neighboring planets in the Solar System, with a K-S p-value of 66.2%. If we consider the Solar System to be dynamically packed, then it is not unreasonable to ask whether other planetary systems with similar dynamical spacing are also dynamically packed.

3. Based on our best-fit distribution of planetary spacing: ≥31% of 2-planet systems, ≥35% of 3-planet systems, and ≥45% of 4-planet systems are dynamically packed. This means that such systems are filled to capacity and cannot hold another planet in an intermediate orbit without becoming unstable.

4. Our results on the dynamical packedness of planetary systems are consistent with the packed planetary systems hypothesis that all planetary systems are filled to capacity, as we find sizeable lower limits on the fraction of systems that are dynamically packed.

5. Compact systems such as Kepler-11 and Kepler-36 represent extremes in the dynamical spacing distribution. For example, the two known planets in Kepler-36 are more closely spaced than 99.7% of all neighboring planets represented by our orbital period and planet radius regime.

REFERENCES

Barnes, R., Goździewski, K., & Raymond, S. N. 2008, ApJ, 680, L57

Barnes, R. & Greenberg, R. 2007, ApJ, 665, L67

Barnes, R. & Quinn, T. 2004, ApJ, 611, 494

Batalha, N. M., Rowe, J. F., Bryson, S. T., Barclay, T., Burke, C. J., Caldwell, D. A., Christiansen, J. L., Mullally, F., Thompson, S. E., Brown, T. M., Dupree, A. K., Fabrycky, D. C., Ford, E. B., Fortney, J. J., Gilliland, R. L., Isaacson, H., Latham, D. W., Marcy, G. W., Quinn, S., Ragozzine, D., Shporer, A., Borucki, W. J., Ciardi, D. R., Gautier, III, T. N., Haas, M. R., Jenkins, J. M., Koch, D. G., Lissauer, J. J., Rapin, W., Basri, G. S., Boss, A. P., Buchhave, L. A., Charbonneau, D., Christensen-Dalsgaard, J., Clarke, B. D., Cochran, W. D., Demory, B.-O., Devore, E., Esquerdo, G. A., Everett, M., Fressin, F., Geary, J. C., Girouard, F. R., Gould, A., Hall, J. R., Holman, M. J., Howard, A. W., Howell, S. B., Ibrahim, K. A., Kinemuchi, K., Kjeldsen, H., Klaus, T. C., Li, J., Lucas, P. W., Morris, R. L., Prsa, A., Quintana, E., Sanderfer, D. T., Sasselov, D., Seader, S. E., Smith, J. C., Steffen, J. H., Still, M., Stumpe, M. C., Tarter, J. C., Tenenbaum, P., Torres, G., Twicken, J. D., Uddin, K., Van Cleve, J., Walkowicz, L., & Welsh, W. F. 2012, ArXiv e-prints

Batygin, K. & Laughlin, G. 2008, ApJ, 683, 1207

Carter, J. A., Agol, E., Chaplin, W. J., Basu, S., Bedding, T. R., Buchhave, L. A., Christensen-Dalsgaard, J., Deck, K. M., Elsworth, Y., Fabrycky, D. C., Ford, E. B., Fortney, J. J., Hale, S. J., Handberg, R., Hekker, S., Holman, M. J., Huber, D., Karoff, C., Kawaler, S. D., Kjeldsen, H., Lissauer, J. J., Lopez, E. D., Lund, M. N., Lundkvist, M., Metcalfe, T. S., Miglio, A., Rogers, L. A., Stello, D., Borucki, W. J., Bryson, S., Christiansen, J. L., Cochran, W. D., Geary, J. C., Gilliland, R. L., Haas, M. R., Hall, J., Howard, A. W., Jenkins, J. M., Klaus, T., Koch, D. G., Latham, D. W., MacQueen, P. J., Sasselov, D., Steffen, J. H., Twicken, J. D., & Winn, J. N. 2012, Science, 337, 556

Chambers, J. E. 1999, MNRAS, 304, 793

Chambers, J. E., Wetherill, G. W., & Boss, A. P. 1996, Icarus, 119, 261

Christiansen, J. L., Jenkins, J. M., Caldwell, D. A., Burke, C. J., Tenenbaum, P., Seader, S., Thompson, S. E., Barclay, T. S., Clarke, B. D., Li, J., Smith, J. C., Stumpe, M. C., Twicken, J. D., & Van Cleve, J. 2012, PASP, 124, 1279

Fang, J. & Margot, J.-L. 2012a, ArXiv e-prints

—. 2012b, ApJ, 751, 23

Gladman, B. 1993, Icarus, 106, 247

Howard, A. W., Marcy, G. W., Bryson, S. T., Jenkins, J. M., Rowe, J. F., Batalha, N. M., Borucki, W. J., Koch, D. G., Dunham, E. W., Gautier, T. N., Cleve, J. V., Cochran, W. D., Latham, D. W., Lissauer, J. J., Torres, G., Brown, T. M., Gilliland, R. L., Buchhave, L. A., Caldwell, D. A., Christensen-Dalsgaard, J., Ciardi, D., Fressin, F., Haas, M. R., Howell, S. B., Kjeldsen, H., Seager, S., Rogers, L., Sasselov, D. D., Steffen, J. H., Basri, G. S., Charbonneau, D., Christiansen, J., Clarke, B., Dupree, A., Fabrycky, D. C., Fischer, D. A., Ford, E. B., Fortney, J. J., Tarter, J., Girouard, F. R., Holman, M. J., Johnson, J. A., Klaus, T. C., Machalek, P., Moorhead, A. V., Morehead, R. C., Ragozzine, D., Tenenbaum, P., Twicken, J. D., Quinn, S. N., Isaacson, H., Shporer, A., Lucas, P. W., Walkowicz, L. M., Welsh, W. F., Boss, A., Devore, E., Gould, A., Smith, J. C., Morris, R. L., Prsa, A., Morton, T. D., Still, M., Thompson, S. E., Mullally, F., Endl, M., & MacQueen, P. J. 2012, The Astrophysical Journal Supplement Series, 201, 15

Ji, J., Liu, L., Kinoshita, H., & Li, G. 2005, ApJ, 631, 1191

Laskar, J. 1989, Nature, 338, 237

—. 1990, Icarus, 88, 266

—. 1994, A&A, 287, L9

Laskar, J. & Gastineau, M. 2009, Nature, 459, 817

Lecar, M., Franklin, F. A., Holman, M. J., & Murray, N. J. 2001, ARA&A, 39, 581

Lissauer, J. J., Fabrycky, D. C., Ford, E. B., Borucki, W. J., Fressin, F., Marcy, G. W., Orosz, J. A., Rowe, J. F., Torres, G., Welsh, W. F., Batalha, N. M., Bryson, S. T., Buchhave, L. A., Caldwell, D. A., Carter, J. A., Charbonneau, D., Christiansen, J. L., Cochran, W. D., Desert, J.-M., Dunham, E. W., Fanelli, M. N., Fortney, J. J., Gautier, III, T. N., Geary, J. C., Gilliland, R. L., Haas, M. R., Hall, J. R., Holman, M. J., Koch, D. G., Latham, D. W., Lopez, E., McCauliff, S., Miller, N., Morehead, R. C., Quintana, E. V., Ragozzine, D., Sasselov, D., Short, D. R., & Steffen, J. H. 2011a, Nature, 470, 53

Lissauer, J. J., Ragozzine, D., Fabrycky, D. C., Steffen, J. H., Ford, E. B., Jenkins, J. M., Shporer, A., Holman, M. J., Rowe, J. F., Quintana, E. V., Batalha, N. M., Borucki, W. J., Bryson, S. T., Caldwell, D. A., Carter, J. A., Ciardi, D., Dunham, E. W., Fortney, J. J., Gautier, III, T. N., Howell, S. B., Koch, D. G., Latham, D. W., Marcy, G. W., Morehead, R. C., & Sasselov, D. 2011b, ApJS, 197, 8

Menou, K. & Tabachnik, S. 2003, ApJ, 583, 473

Michtchenko, T. A. & Ferraz-Mello, S. 2001, AJ, 122, 474

Ragozzine, D. et al. 2012, in AAS/Division for Planetary Sciences Meeting Abstracts, Vol. 44, AAS/Division for Planetary Sciences Meeting Abstracts

Raymond, S. N. & Barnes, R. 2005, ApJ, 619, 549

Raymond, S. N., Barnes, R., & Gorelick, N. 2008, ApJ, 689, 478

Raymond, S. N., Barnes, R., & Kaib, N. A. 2006, ApJ, 644, 1223

Rivera, E. & Haghighipour, N. 2007, MNRAS, 374, 599

Sussman, G. J. & Wisdom, J. 1988, Science, 241, 433

—. 1992, Science, 257, 56

Youdin, A. N. 2011, ApJ, 742, 38